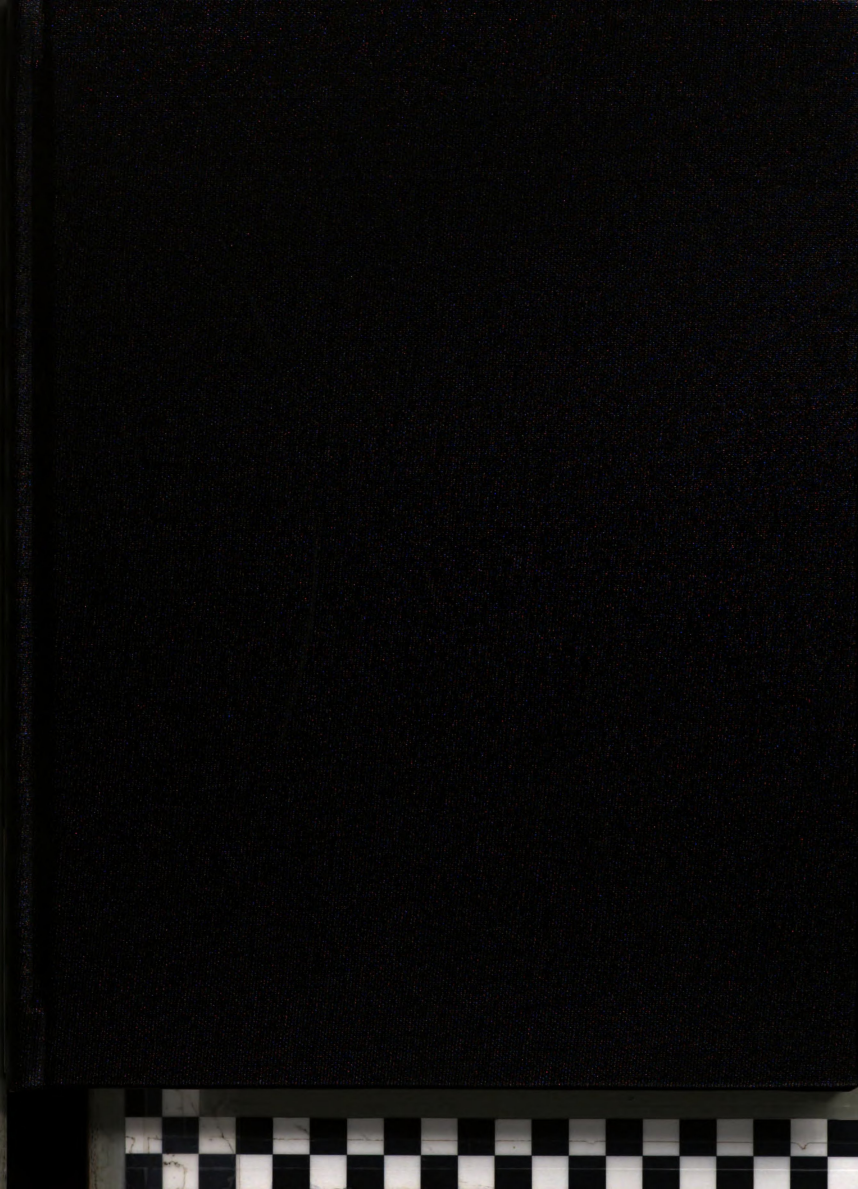

dissertation entitled

QUADRUPOLE COLLECTIVITY MEASUREMENTS
IN EVEN-EVEN, NEUTRON-RICH SILICON AND
SULFUR ISOTOPES APPROACHING N = 28

presented by

Christopher M. Campbell

has been accepted towards fulfillment
of the requirements for the

Ph.D. degree in Physics and Astronomy

Major Professor's Signature

5-10-07

Date

MSU is an affirmative-action, equal-opportunity employer

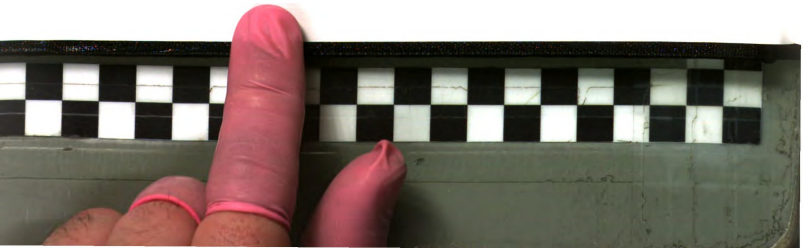

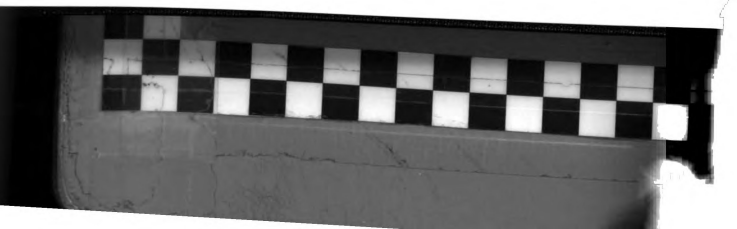

QUADRUPOLE COLLECTIVITY MEASUREMENTS IN EVEN-EVEN, NEUTRON-RICH SILICON AND SULFUR ISOTOPES APPROACHING $N = 28$

By

Christopher M. Campbell

A DISSERTATION

Submitted to
Michigan State University
in partial fulfillment of the requirements
for the degree of

DOCTOR OF PHILOSOPHY

Department of Physics and Astronomy

2007

ABSTRACT

QUADRUPOLE COLLECTIVITY MEASUREMENTS IN EVEN-EVEN, NEUTRON-RICH SILICON AND SULFUR ISOTOPES APPROACHING $N = 28$

By

Christopher M. Campbell

An inelastic proton scattering experiment was performed at the National Superconducting Cyclotron Laboratory to study quadrupole collectivity in the even-even silicon and sulfur isotopes near $N = 28$. Experiments on neutron-rich sulfur isotopes have found significant collectivity and have been interpreted as pointing to the collapse of the $N = 28$ shell gap. Narrowing of a proton subshell gap in the sulfur isotopes may, however, be responsible for the increased collectivity. This experiment gives a quantitative measurement of the decrease in collectivity between ^{42}S and ^{44}S showing that the $N = 28$ shell gap does not vanish at $Z = 16$. In the silicon isotopes, the large, stable $Z = 14$ subshell gap directly ties collective trends to the strength of the $N = 28$ shell closure. Quadrupole collectivity and 2_1^+ excitation energies in the isotopes ^{36,38,40}Si give clear evidence for the narrowing of the $N = 28$ shell gap in the absence of strong proton collectivity.

to my wife Bethany

ACKNOWLEDGMENTS

This thesis has benefited from the hard work of dozens of people to whom I am most grateful. I will start by thanking my advisor Thomas Glasmacher for introducing me to the field of rare isotopes when I was in the Research Experience for Undergraduates program. I thank Thomas for being a supportive and challenging mentor. I am grateful to Michigan State University and the National Science Foundation for financial support during my graduate education.

I thank the members of the Gamma group for their insights, support, and friendship. I thank Katie Yurkewicz for her help during my REU. I thank Heather Zwahlen for helping a new student get up to speed and for all the fun we had with the filling system. I will always remember installing the SeGA detectors for your experiment. I thank Dan-Cristian Dinca for working with me on the SeGA pulse-shape acquisition and analysis. I thank Russ Terry and Alexandra Gade for our discussions of nuclear structure and Doppler correction of γ-rays.

I am very grateful to my Japanese collaborators who provided, constructed, and maintained the RIKEN-Kyushu-Rikkyo liquid hydrogen target used in my thesis experiment. I especially thank Nori Aoi and Shoko Kanno for their helpful discussions. I thank Ken Yoneda and Nori Aoi for their assistance in understanding γ-ray angular distribution calculations based on ECIS outputs.

I thank the many outside collaborators with whom I have had the pleasure of working. In particular, I thank Lew Riley for many helpful discussion on proton scattering, probe sensitivity, and ECIS. I also owe a debt of gratitude to my collaborators from Florida State University, especially Kirby Kemper and Paul Cottle for focusing attention on the question of changing proton collectivity in the neutron-rich sulfur isotopes. I thank Mihai Horoi for shell model calculations and Hiroyuki Sagawa for his help with effective charges.

This work was made possible by the NSCL staff, and I am grateful for all their

help. I thank Len Morris for all his help in designing detector stands, beam line components, and experimental setups for the liquid hydrogen target campaign. I thank the operations and A1900 groups for good beams. I thank Daniel Bazin and John Yurkon for helping me understand the S800 and the focal plane detectors — and for rebuilding the focal plane detectors after a minor disaster during the start of my experiment.

For their support and thoughtful questions, I thank my committee members: Simon Billinge, Wayne Repko, Krzysztof Starosta, Vladimir Zelevinsky, and Thomas Glasmacher. I also thank Alex Brown — who served on my committee until his sabbatical — for his insights, his shell model calculations, and our many discussions on nuclear structure.

Thank you all.

TABLE OF CONTENTS

LIST OF TABLES

LIST OF FIGURES

Images in this dissertation are presented in color.

Chapter 1

Introduction

1.1 The nucleus

The nucleus is a bound collection of protons and neutrons — typically found at the center of an atom. Protons (positively charged) and neutrons (neutral) are collectively called nucleons due to their shared properties. Both types of nucleons have an intrinsic spin of 1/2, have masses near 940 MeV/c^2, and are fermions. (Here, and throughout this thesis, all spins and angular momenta are given in units of $\hbar$.) The like-nucleon interaction strength ($n-n$ or $p-p$) is independent of the nucleon type — once the Coulomb interaction in $p-p$ has been removed. Interactions between nucleons arise from the strong interaction, which also holds together quarks inside a nucleon.

Nuclei have a characteristic size on the order of 10^{-15} m, or 1 fm (SI unit femtometer, historically known as a fermi). This is far smaller than the characteristic atomic scale of 10^{-10} m. Nuclear excitations are typically of order $0.1-10$ MeV ($1\ MeV = 10^6\ eV$), while atomic excitations are typically on the eV scale. This separation of scales effectively decouples the nuclear and atomic realms in most cases.

Similar to the arrangement of elements in the periodic table, Figure 1.1 shows the chart of the nuclides which plots number of neutrons (N) on the horizontal axis and number of protons (Z) on the vertical axis. Nuclei having the same number of

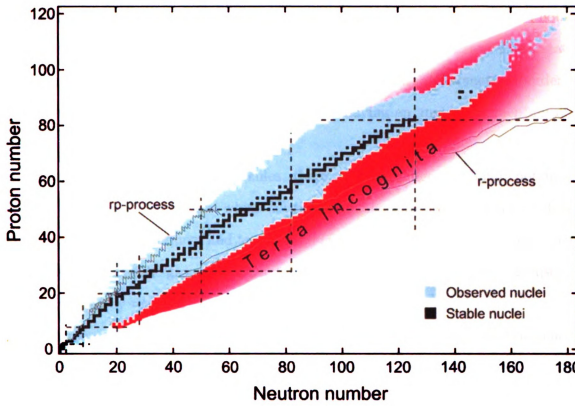

Figure 1.1: Chart of the nuclides

protons (neutrons) are referred to as isotopes (isotones). Stable nuclei — shown by black squares in figure 1.1 — lie along an arc known as the valley of stability. Here, stability refers to β-stability, i.e. these nuclei do not undergo β-decay which convert protons into neutrons, or vice-versa. The vast majority of our knowledge of the nucleus has come from this stable subset of possible nuclei.

Nuclei which are β-unstable may allow one to study the effects of changing proton and neutron number independently and may allow access to nuclei along the various nucleosynthesis pathways which produce the heavy elements.

1.2 Nuclear structure

Nuclear properties are determined by the number of protons and neutrons and their arrangement, i.e. the relative positions and motions of all nucleons. Nuclear structure is the study of nuclear properties and how they arise due to the motions of nucleons.

Like atoms and molecules, nuclei have ground states and may have a number of bound excited states which arise from the interactions among their constituents. These states are identified by their total angular momentum J, parity π, and sometimes order in a level scheme i written as J_i^π. So, the first level having an angular momentum of 2 and a positive parity would be denoted 2_1^+.

In the case of atoms and molecules, there are long-range, Coulomb potentials created by the nucleus or nuclei which determine the motions of most of the electrons involved. Only the outermost and least bound (valence) electrons actively participate in changes between the ground and excited state. Furthermore, the nuclei themselves are unchanged by rearrangements of these electrons.

Nuclei, on the other hand, have no such strong, unchanging, long-distance, central potential. Instead, the nucleon-nucleon strong interaction has a short range and the nucleons — as a group — create the potential which binds them together. The average potential experienced by a nucleon interacting with all other nucleons in the nucleus is called the nuclear mean-field potential and may be approximated by a central potential. Given a central potential, the constituents may be described as filling orbitals whose properties, ordering, and spacing are determined by the underlying potential.

Shell structure in nuclei was discovered by studying isotopic abundances and the number of stable isotones for a given element [1]. These observations pointed to particularly stable numbers of protons or neutrons called magic numbers. The nuclear magic numbers are 2, 8, 20, 28, 50, 82, and 126.

Atomic systems having so-called magic numbers of electrons were also known to display particular stability. In the atomic case, electrons — which are also spin 1/2 fermions — may only occupy the same orbital if they have different spin orientations. Electrons fill the orbitals pairwise from lowest to highest energy until all electrons have been placed. The electron magic numbers correspond to the atomic numbers of the noble gasses on the periodic table: 2, 10, 18, 36, 54,... These atomic magic numbers result from a degeneracy in the eigenvalues of the Coulomb potential for a

system of spin 1/2 fermions.

In nuclei, a first-principles calculation of the energy levels is complicated by the fact that the potential, which leads to orbitals is created by the particles filling the orbitals. Instead, the nuclear magic numbers were initially used to learn about the nuclear mean field. The three-dimensional harmonic oscillator potential yields the sequence 2, 8, 20, 40, 70, ... for nucleons filling harmonic oscillator shells. However, the harmonic oscillator potential — a parabola extending to infinity — is rather unphysical, and terms were added to better approximate the nuclear potential. The addition of an attractive $\ell \cdot \ell$ term is equivalent to deepening the potential at large radii. This changed the magic numbers but failed to reproduce the data. Finally, a strong spin-orbit term was introduced which depressed the $j = \ell + 1/2$ orbital with the maximum orbital angular momentum (ℓ) from each harmonic oscillator shell. This lead to the nuclear magic numbers: 2, 8, 20, 28, 50, 82, and 126 [2,3].

Orbitals are typically labeled as $n\ell_j$ where n is the number of nodes in the radial wavefunction, ℓ is the orbital angular momentum, and $j = \ell \pm 1/2$ is the total angular momentum. The prefixes ν and π specify neutron and proton, respectively. Node counting may start from zero or one depending on the author. In this work, n will start at zero. Orbital angular momentum is given by $s, p, d, f, \ldots$ for $\ell = 0, 1, 2, 3, \ldots$ As an example, the first neutron orbital having $\ell = 3$ has $j = 3 + 1/2 = 7/2$ due to the spin-orbit force and is denoted $\nu 0 f_{7/2}$.

1.2.1 The nuclear shell model

Given this shell structure, it is then natural to consider a separation of nucleons into two categories: core and valence. Core nucleons are those filling orbitals up to a magic number, and valence nucleons will fill orbitals above that magic number. Considering only valence nucleons restricted to a few orbitals, detailed calculations including nucleon-nucleon couplings become possible. This is commonly known as a shell model calculation — but a better term may be interacting shell-model calculation. In this

way, the nuclear level energies and properties may be calculated.

Why – or when – is such a separation reasonable? The energy spacing between valence orbitals, and the highest-energy filled orbitals of the core is $\sim 1\hbar\omega$ in terms of the harmonic oscillator potential used to describe the mean field. This energy is approximately given as $\hbar\omega \approx 45A^{-1/3} - 25A^{-2/3}$ [4]. For ^{16}O and ^{208}Pb, the estimates are 14 MeV and 7 MeV, respectively. For energy levels well below $1\hbar\omega$, the approximation appears valid. It is important to point out that even though core and valence nucleons appear to have many opportunities to interact, the Pauli principle prevents many such interactions [5]. That is, a valence nucleon may not scatter off a core nucleon with a small energy-momentum transfer because all orbitals to which the core nucleon would scatter are filled.

An introduction to the shell model is a book in itself, so only a brief discussion is presented here. An interacting shell model calculation is defined by the selection of:

- a core,
- a set of valence orbitals,
- a set of single-particle energies,
- a two-body interaction, and
- the number of valence protons and neutrons.

The core is typically chosen as the largest doubly-magic nucleus having fewer neutrons and protons than the nuclei being calculated. Valence orbitals may consist of all orbitals in the major proton and neutron shells above the core or some subset thereof. Single-particle energies (SPEs) are typically taken from nuclei having one nucleon more or fewer than a doubly-magic nucleus; a SPE represents the binding energy of a single particle due to the mean field produced by the core. A two-body interaction describes the interactions between pairs of valence nucleons; this interaction is not the free nucleon-nucleon interaction. Instead, the two-body interaction implicitly or

explicitly contains many-body physics. In practice, the two-body interaction — or two-body matrix elements (TBME) — may be fit to well known nuclear levels [6].

The nucleus is a quantum system. The Hamiltonian describing nuclear levels results from a sum over single-particle energies and two-body interactions of valence particles. An initial set of states may be defined as a sum over partitions of nucleons into orbitals, which is further summed over spin couplings for each partition which yield a given J^π. This initial set of states is then diagonalized to find eigenvalues (level energies) and eigenvectors (wave functions). Thus, shell-model states arise from a mixing of many configurations.

These states then give level schemes, spectroscopic factors, multipole moments, and transition probabilities (transition matrix elements). Spectroscopic factors are found by taking the wavefunction overlap of a state in a nucleus of mass A and the result of a particle creation operator acting on a state in a daughter nucleus of mass $A-1$. Experiments compare to the C^2S values which includes an isospin Clebsch-Gordan coefficient. Multipole moments are found by taking the expectation value of a multipole operator $\hat{O}$, i.e. $< \Psi|\hat{O}|\Psi >$. The electric quadrupole moment of the ground state would then be found using $\hat{O} = r^2 Y_0^2 e$ and the ground state wavefunction. Similarly, the proton transition matrix element for an $E2$ excitation of the 2_1^+ from a 0_1^+ ground state is given by

$$M_p = \sqrt{\frac{16\pi}{5}} \sum_{\mu=-2}^{+2} < 2_1^+; M = \mu | \sum_k r^2 Y_\mu^2(k) e | 0_1^+ >,$$

where the sum is over all protons, k [5]. The reduced transition probability — termed the B(E2; $0_1^+ \rightarrow 2_1^+$), or B(E2$\uparrow$) value — would then be given by $B(E2\uparrow) = |M_p|^2$.

Although the shell model has been quite successful in describing low-lying nuclear structure [7–9], it does not offer a complete description of nuclear states and transitions. To make calculations tractable, the model space available to nucleons is truncated to a few orbitals and the two-body interactions are modified to remove the

hard core of the $n-n$ potential. Direct comparisons with spectroscopic studies and measurements of transition rates reveal discrepancies. Theory and experiment show that the valence particles of the shell model behave as independent particles bound in the mean field of the nucleus $\sim 2/3$ of the time; the remaining time being spent in a correlated state [10].

Similarly, mixing with configurations outside the model space is required to explain observe transitions between bound states of the nucleus. Specifically, quadrupole transition strengths between low-lying states are larger than estimated by the shell model. This is explained as a small admixture of $2\hbar\omega$ components which arise from excitation of the core [11]. Essentially, the core is not, in fact, inert and may be polarized by the valence nucleons. The simplest analogy might be the tides experienced on Earth due to the gravitational pull and motion of the Moon. However, in the nuclear case, one must consider separately the effects of valence protons and neutrons on the protons and neutrons of the core. In equations 1.1 and 1.2, the generalized effective charge model [12] includes four core-valence couplings ($\delta_{CoreValence}$) and describes the effective matrix elements (M_p, M_n) in terms of the shell model — or valence — matrix elements (A_p, A_n).

$$M_p = A_p(1+\delta_{pp}) + A_n\delta_{pn} \tag{1.1}$$

$$M_n = A_n(1+\delta_{nn}) + A_p\delta_{np} \tag{1.2}$$

1.2.2 Collective models of the nucleus

In contrast to the shell model, collective models of the nucleus do not explicitly consider the individual motions and couplings of all valence nucleons. Instead, nuclei are treated much like a rubber ball or a drop of liquid; this is termed a macroscopic model. Such objects are constrained to have constant volume, but their surfaces may be dynamically or statically deformed [13]. Details of this deformation are then governed by some energy functional depending on surface, volume, and correlation energies. These

correlation energies may then be related back to specific nucleon orbital overlaps in a more microscopic model. Unpaired nucleons may then couple to the underlying collective modes of the even-even core.

The two fundamental paradigms for collective motion are vibration and rotation. Both may be viewed as a volume conserving modification of the nuclear surface:

$$R = R_0[1 + \Sigma_\mu \alpha_{\lambda\mu} Y_{\lambda\mu}(\theta, \phi)] \tag{1.3}$$

where λ denotes the multipole order [14]. The strongest collective excitations are typically $\lambda = 2$, i.e. quadrupole. Quadrupole parameters $\alpha_{2\mu}$, or simply α_μ, are simplified by choice of quantization axis and converted into the more useful parameters β and γ.

$$\alpha_0 = \beta \cos\gamma \tag{1.4}$$

$$\alpha_{\pm 2} = \beta \sin\gamma \tag{1.5}$$

$$\alpha_{\pm 1} = 0 \tag{1.6}$$

The magnitude of a quadrupole deformation is given by β while γ describes the degree of axial symmetry. Axial symmetric deformation is found when $\gamma = 0°$. This thesis will treat all deformations as axially symmetric unless otherwise noted.

Vibration occurs when a nucleus may be deformed but energetically favors an average spherical shape, and a harmonic oscillator potential in terms of β is often used. The shape of the nuclear surface may then oscillate. Excitation involves the additions of phonons to this system. In a rotational nucleus, a minimum in the potential $V(\beta)$ occurs away from $\beta = 0$, and the nucleus is statically deformed in its ground state. Positive deformation is termed prolate; negative deformation is oblate. Excitation energy goes into rotating this deformed nucleus about some axis other than the deformation axis.

Doubly-magic nuclei are spherical and have excitations built from particle-hole

states. Nuclei having a single closed shell, or only a few valence nucleons, may be vibrational and typically show only modest collectivity. Rotation is associated with a coupling of proton and neutron degrees of freedom [15]. Thus, both neutron and proton valence particles — perhaps several of each — are needed to form a statically deformed state.

1.3 Exploring new territory

Exploration of β-unstable nuclei provides additional tests of models developed near stability. In these exotic nuclei — also called rare isotopes — one may also study novel couplings of valence nucleons. Specifically, this thesis will probe the evolution of quadrupole collectivity in neutron-rich silicon and sulfur nuclei near $N = 28$. Figure 1.2 shows the isotopes studied in this thesis, ^{36,38,40}Si and ^{40,42,44}S.

The ordering of single-particle orbitals and the gaps in excitation between them form the foundation of the shell model. These single-particle energies (SPEs) are known to vary with mass, which changes the size and depth of the mean-field potential [16]. These SPEs are also known to vary with the filling of particular orbitals due to specific nucleon overlaps giving increased, or decreased, binding [14, 17, 18]. In exotic nuclei, these changes can be more extreme and even major shell gaps are affected [19]. Nuclei in the island of inversion [20–22] — canonically $N = 20-22, Z = 10-12$ — have intruder configuration ground states $(\nu(0f_{7/2})^x(sd)^{12-x})$. Neutrons are promoted across the $N = 20$ shell gap because this gap is smaller in these neutron-rich nuclei and the intruder states have increased correlation energy. Increased binding of the ground states [20] and strong collectivity in the low-lying 2_1^+ states of even-even nuclei [23–25] were the first observables used to discover and study this region. Much work is still left to do in this region. For example, the first quantitative measurement of intruder contributions to the ground state wavefunctions of ^{28}Ne was recently performed [26].

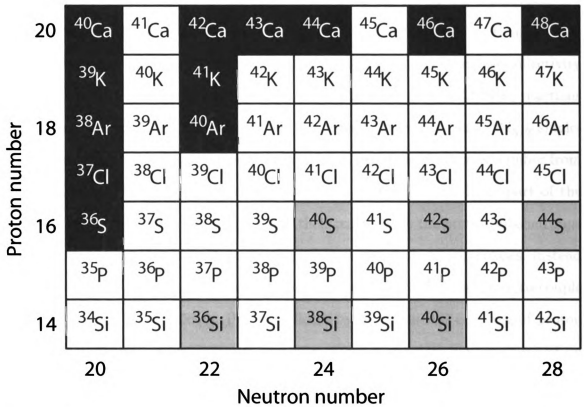

Figure 1.2: An expanded view of the chart of the nuclides is given for the region studied in this thesis. Isotopes shown as black squares are stable, and isotopes studied in this thesis are shown as grey squares.

In the $N = 28$ isotones, the first experimental indications of a reduction in the $\nu(0f_{7/2} - 1p_{3/2})$ shell gap came from the β-decay lifetime of ^{44}S, which was used to infer static deformation [27]. Coulomb excitation was then used to measure the B(E2$\uparrow$) value, confirming significant collectivity in this $N = 28$ nucleus [28]. The trend in B(E2$\uparrow$) values across the sulfur ($Z = 16$) isotopes showed quadrupole collectivity rose from a minimum at $N = 20$ to a maximum at $N = 26$; the small decrease between $N = 26$ and $N = 28$ was nearly the same as the error bar for such a comparison.

An alternate explanation was put forward by Dr. Cottle and Dr. Kemper [29]. They argued that shifts in the proton SPEs might be the cause of increase collectivity in the neutron-rich sulfur isotopes. Using data taken collected in $(d,^3\mathrm{He})$ reactions on calcium isotopes [30], Cottle and Kemper traced the $\pi 1s_{1/2}$ and $\pi 0d_{5/2}$ single-particle energies relative to the $\pi 0d_{3/2}$ orbital as a function of neutron number from $N = 20 - 28$. (Note: these were energy centroids summed over a large part of the single-particle strengths.) Figure 1.3 shows their results with the proton subshell gaps labeled. As N increases from 20 to 28, the subshell gap at $Z = 16$ decreases. Instead of filling the $1s_{1/2}$ subshell, the last two valence protons in ^{42,44}S are free to couple in a larger space of $1s_{1/2}0d_{3/2}$. Proton collectivity increases and coupling of proton and neutron degrees of freedom can lead to a region static deformation centered on ^{42}S [31, 32].

Thus, the rise in collectivity approaching $N = 28$ in the sulfur isotopes could be a sum of

- proton collectivity arising from the collapse of the $Z = 16$ subshell gap,
- neutron collectivity resulting from a diminished $N = 28$ shell gap, and
- increased $p - n$ correlation energy leading to static deformation.

Measurements of sulfur isotopes are then inconclusive with respect to changes in $N = 28$. Silicon isotopes, on the other hand, have a rather large $Z = 14$ subshell gap

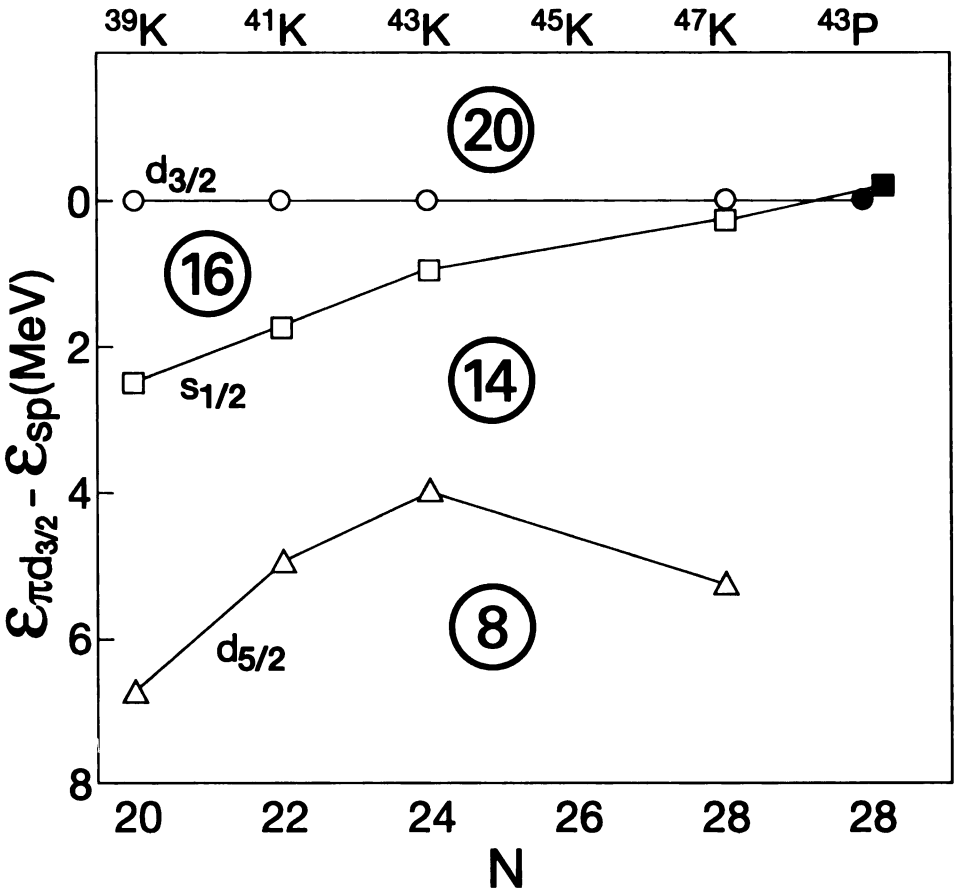

Figure 1.3: Proton single-particle energy shifts near $N = 28$ are shown for the $1s_{1/2}$ and $0d_{5/2}$ orbital relative $0d_{3/2}$ [29]. As the $Z = 16$ subshell gap narrows, proton collectivity is expected to increase. The $\pi(1s_{1/2} - 0d_{3/2})$ degeneracy is also observed in neutron-rich ^{43}P [33,34].

from $N = 20 - 28$ and are well suited to determine whether the $N = 28$ shell gap has truly weakened.

Shell model calculations in this region are typically performed using the SDPF-NR interaction [9] placing $N - 20$ neutrons in the pf shell and $Z - 8$ protons in the sd shell — or more succinctly, $\pi(sd)^{Z-8}\nu(pf)^{N-20}$. The SDPF-NR interaction resulted from combining the USD interaction between protons with the KB$'$ interaction between neutrons and a proton-neutron cross-shell interaction taken from G-matrix calculations then fit to data [31]. Initially, single particle energies were fixed by values measured at or near stability, but β-decay measurements found that the $\nu 1p_{3/2}$ state in ^{35}Si was significantly lower in excitation than predicted [35]. The interaction was modified to reproduce the smaller $\nu(0f_{7/2} - 1p_{3/2})$ splitting observed at $N = 21, Z = 14$. These changes had little effect on the calculated spectra of neutron-rich sulfur and argon isotopes, but the 2_1^+ excitation energy of ^{42}Si was reduced from 2.5 MeV to 1.5 MeV, indicating a strong sensitivity to the choice of interaction. This modified interaction is denoted SDPF-NR [9] and is compared to the levels observed in this thesis.

Chapter 2

Experimental Method

This experiment was designed to measure the collectivity of several β-unstable neutron-rich nuclei by extracting quadrupole deformation parameters from inelastic proton scattering cross sections.

A beam of these exotic nuclei — traveling at $\sim$ 40% of the speed of light — was produced and directed onto a liquid hydrogen target. The hydrogen nuclei — protons — were occasionally scattered off projectile nuclei, which were sometimes (roughly 1 in 10^4) left in an excited state. After some very short time — typically much less than 100 ps — the bound excited nuclei would de-excite by emitting γ rays. A fraction of these γ rays deposited their full energy in one of several γ-ray detectors arranged around the target. The beam of nuclei then passed through a series of magnets and were detected. Data were collected and cross sections for the population of specific excited states were extracted. These cross sections were then used to determine deformation parameters, $|\beta_{2,(p,p')}|$, in a collective model.

The first section of this chapter discusses proton scattering at intermediate beam energies. It focuses on the theory and inputs needed to extract deformation parameters from cross sections. Remaining sections describe the experimental setup, calibrations, and uncertainties in the cross section measurement.

2.1 Proton scattering

Inelastic proton scattering provides a method to directly measure nuclear collectivity. Specifically, the sensitivity of proton scattering to protons and neutrons in the nucleus has been employed along with the selective proton-sensitivity of Coulomb excitation to measure differences in the proton and neutron contributions to the excitation of specific states [36–38]. More recently, inverse-kinematics proton scattering has been used instead of Coulomb excitation to study collective states in the most exotic nuclei, as proton scattering experiments on liquid or solid hydrogen targets are feasible with beam rates of about a factor of ten less than is required for Coulomb excitation.

The present experiment was devised to measure quadrupole collectivity in ^{36,38,40}Si and ^{40,42,44}S. Deformation parameters ($\beta_{2,(p,p')}$) were deduced from inelastic excitation cross sections ($\sigma_{p,p'}$) using the DWBA code ECIS [39]. Collective form-factors for vibrational and rotational excited states were employed in deducing deformation parameters from the measured cross sections. A brief review of the underlying theory which allows the $\sigma_{p,p'} \rightarrow \beta_{2,(p,p')}$ deduction is presented in the next section.

2.1.1 Scattering theory

Scattering of a particle off a nucleus is a basic, but fundamental, problem in the field of nuclear reactions. The present experiment is concerned only with the scattering of $\sim$ 100 MeV protons on a nucleus. Furthermore, only the cross section for scattering which populates bound, excited states of that nucleus is relevant. Finally, only low-lying, collective states of even-even nuclei are analyzed herein.

The full derivation of scattering from a potential is covered in quantum mechanics and nuclear reaction texts [40–43]. Only a general overview is given here.

Elastic scattering is treated by solving for the wave functions which satisfy the Schrödinger equation:

$$\left(-\frac{\hbar^2}{2m}\nabla^2 + V\right)\Psi = E\Psi. \tag{2.1}$$

The Dirac equation may be used instead of the Schrödinger equation to handle relativistic kinematics; this is, in fact, done in the code ECIS [39]. Scattering comes in as a modification of an initial plane wave. The asymptotic (large R) wave functions are a superposition of the original plane wave and an outgoing spherical wave modulated by a scattering amplitude, f [42].

$$\Psi^{+}_{\vec{k}}(\vec{r}) \sim \left(e^{i\vec{k}\cdot\vec{r}} + f_{\vec{k}}(\hat{r}) \frac{e^{ikr}}{r} \right) \tag{2.2}$$

The probability for the scattered particle to pass through a specific point is an integral over $|\Psi|^2$, and the differential cross-section for elastic scattering is:

$$\frac{d\sigma}{d\Omega} = |f_{\vec{k}}(\hat{r})|^2 \tag{2.3}$$

When elastic scattering is the dominant reaction, other channels are treated through absorptive potentials which remove flux — or as perturbations. Inelastic scattering is treated as a perturbation. In calculating the scattering amplitudes, elastic scattering wavefunctions are used along with some additional potential responsible for the inelastic excitation.

The distorted wave born approximation (DWBA) is often employed in such calculations. Instead of plane waves, distorted waves ($\chi^{\pm}$) are used which satisfy the Schrödinger equation for the elastic potential. The Born approximation is applied by using the scattering wave functions calculated using the elastic potential. Essentially, the part of the potential responsible for the inelastic transition is weak compared to the elastic potential. Thus, the total potential and scattering wave functions are well approximated by the elastic potential and the distorted waves derived from that elastic potential [43].

For inelastic scattering, we consider not only the relative position wave function for the proton-nucleus system, but also the wave function describing the internal structure of the nucleus. Scattering amplitudes, f, for inelastic scattering are then

integrals over products of an incoming distorted wave, an outgoing distorted wave, and a term which couples the initial and final states via the transition potential [43].

To calculate the amplitudes, and thus a cross section, the following inputs are required:

- a potential describing elastic proton-nucleus scattering,
- the initial and final states of the nucleus, and
- a potential which couples these wavefunctions.

2.1.2 Deformation extraction

In practice, nucleon-nucleus elastic scattering at energies from a few keV to hundreds of MeV may be described using an optical model potential [44]. The optical model potential is typically a sum over complex Woods-Saxon potentials and derivatives thereof with parameters — depth, radius, and diffuseness — fit locally to elastic scattering on the nuclei of interest. Fitting the potential is not possible in the present experiment due to the use of the thick-target, γ-ray tagging method (see section 2.3.1 for further discussion). Thus, a global optical model parameterization was used [44]. Similar parameterizations compare well with measurements of proton scattering on nuclei in this region [45].

Inelastic proton scattering on even-even nuclei populates low-lying collective states strongly [46,47]. In particular, shape oscillations of the nuclear surface and rotational states in statically deformed nuclei are typically observed. Because the excitation probability is small, only single-step excitations are expected.

To calculate scattering amplitudes for these states, the collective models discussed in section 1.2.2 are used. Those models described deformations of the nucleus and are appropriate as models for nuclear density. The assumption that changes in the potential should follow changes in density distribution leads to the deformed optical

model [41]. This model was chosen for the analysis of the present experiment. Coupling between initial and final collective states is modeled by a term proportional to $\beta_L dU/dR$ [39], where β_L is the deformation parameter for the L multipole and dU/dR is the radial derivative of the optical potential. Here, the form-factor is a derivative of the original optical potential and is surface peaked. The scattering amplitude f from Eq. 2.3 is proportional to an integral over the product of incoming and outgoing distorted waves and the initial and final states of the nucleus coupled by this collective transition potential. Pulling β_L out of the integral implicit in Eq. 2.3, the integrated cross section is proportional to β_L^2.

Several codes have been developed to handle such DWBA calculations. In this work, the code `ECIS97` [39] was used to calculate DWBA cross sections for the (p, p') reactions considered in this thesis. Total inelastic cross-sections were calculated for multiple deformation parameters, $|\beta_L|$. The quadratic dependence of the calculated cross section on the deformation parameter was used to infer $|\beta_L|$ values for the measured cross sections and their $\pm 1\sigma$ uncertainties. Optical model parameters (OMP) — consisting of the radius, depth, and diffuseness for each Woods-Saxon or derivative of Woods-Saxon potential making up the proton-nucleus optical potential — were calculated for each isotope at its mid-target energy [44]. Because ions traveling through the target lose energy continuously, one must consider the energy dependence of the OMP used. Using the mid-target energy instead of integrating over the distribution of energies within the target leads to a negligible 1% reduction in inferred $|\beta_L|$.

2.1.3 Sensitivity of (p, p') to neutrons and protons

Because proton scattering is sensitive to both protons and neutrons within the nucleus, the deduced deformation parameters will depend on both proton and neutron contributions to the collective excitation. Coulomb excitation, on the other hand, is sensitive only to the protons. By combining measurements of both types, one may extract the relative strengths of the proton and neutron components of a given collective

excitation [36,37]. These ratios may then be compared to model predictions.

In the homogeneous collective model, neutrons and protons share a common deformation, $\delta_p = \delta_n$, where $\delta = \beta R$ [48]. Transition densities for neutrons and protons have a common shape but are scaled by the number of each type of nucleon. Proton and neutron matrix elements are then given by

$$\frac{M_p}{Z\delta_p} = \frac{M_n}{N\delta_n} = \int_0^\infty \rho'(r) r^{\lambda+2} \mathrm{d}r, \tag{2.4}$$

where $\rho(r)$ is the normalized ground state density. So, the ratio of neutron-to-proton matrix elements is $M_n/M_p = N/Z$.

Adding in nuclear shell structure modifies the observed trend for closed shell nuclei [48]. Specifically, a nucleus with a closed-shell structure for one type of nucleon and valence nucleons of the other type will have a large contribution to collective transitions from the valence nucleons. As an example, one would expect $N = 20$ nuclei with valence protons to show stronger proton than neutron collectivity. Thus, neutron closed shell nuclei are expected to have $M_n/M_p < N/Z$, while proton closed-shell nuclei show the opposite. The nucleon-nucleon interaction serves to couple valence nucleon motions to the nucleons of the core, leading to core polarization [49]. Even though a closed shell of nucleons may be considered inert in a shell-model calculation, the core plays a role in transition strengths.

To compare deformation parameters from various probes, Bernstein, Madsen, and Brown included the intrinsic sensitivity of the probe to protons and neutrons in the nucleus [36]. Equation 2.5 uses the sensitivity parameter, b_n/b_p, for the specific case of comparing proton scattering — which samples both protons and neutrons — to Coulomb excitation — which samples only protons.

$$\frac{M_n}{M_p} = \frac{b_p}{b_n}\left[\frac{\delta_{(p,p')}}{\delta_C}\left(1 + \frac{b_n}{b_p}\frac{N}{Z}\right) - 1\right] \tag{2.5}$$

Canonical proton scattering b_n/b_p values are 3 at low proton energy (10-30 MeV)

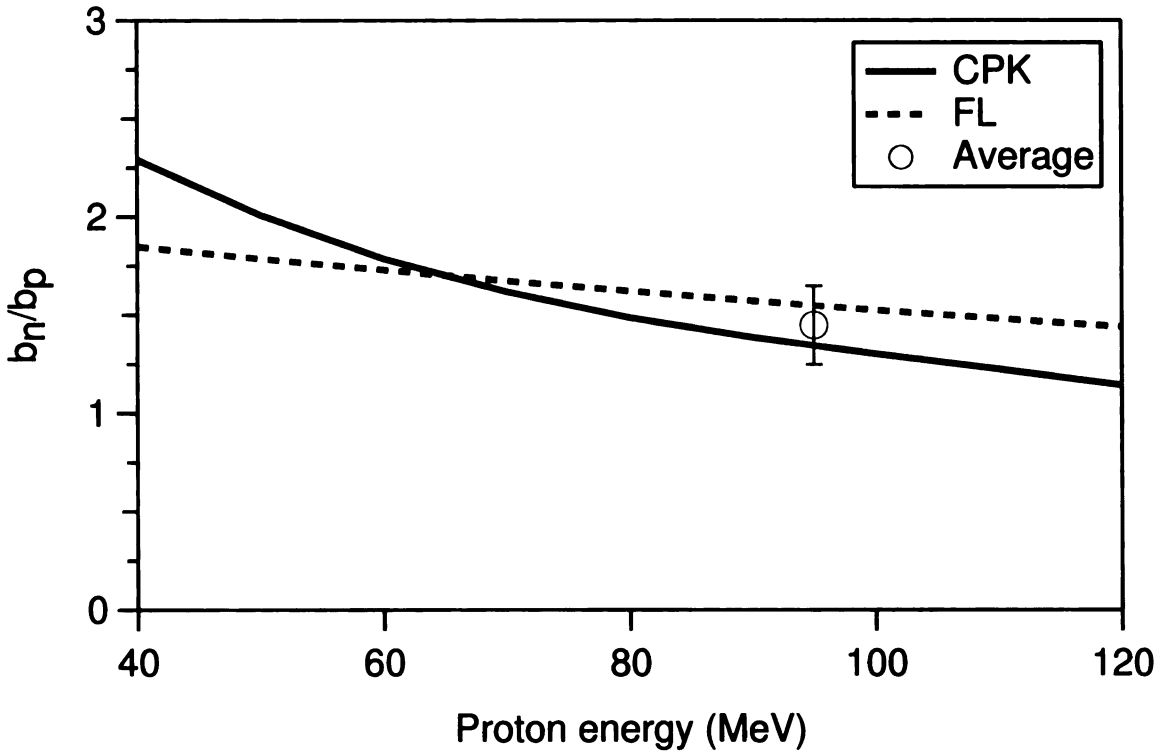

Figure 2.1: Ratio of neutron-to-proton sensitivity, b_n/b_p, in (p,p') calculated using two different parameterizations of the nucleon-nucleon interaction. One calculation was performed by Carr, Petrovich, and Kelly (CPK) [50], and the other uses the Franey and Love (FL) interaction [51].

and 1 at high energy (~1 GeV). This experiment was carried out at intermediate energies, ~100 MeV/nucleon. Following the procedure outlined by Carr, Petrovich, and Kelly [50], the ratio of free nucleon-nucleon amplitudes, $|t_{np}/t_{pp}|$ was used as an estimate of b_n/b_p. Inelastic proton scattering is surface dominated, and the free nucleon-nucleon cross sections are, therefore, a reasonable approximation.

Figure 2.1 shows the ratio $|t_{np}/t_{pp}|$ as a function of bombarding energy for two parameterizations of the nucleon-nucleon interaction. Carr, Petrovich, and Kelly (CPK) [50] used an interaction based on the M3Y [52] in the region 50 MeV $< E_p <$ 100 MeV. The parameterized interaction of Franey and Love (FL) was also used [51]. The mid-target energy for nuclei in this study varied from $\sim 90-100$ MeV. An average energy, $E_p = 95$ MeV was taken, and an average of the two sensitivities was taken. This yields $b_n/b_p = 1.45(20)$, where the difference in the two parameterizations was used as an estimate of uncertainty. At lower energies, the use of the free nucleon-nucleon interac-

tion is a poor approximation, and an effective interaction may be needed to determine b_n/b_p

An additional concern for neutron-rich nuclei is the difference in the radial form-factors for the neutron and proton transition densities. The issue is that the method described in section 2.1.2 is not sensitive to total collective strength but only to the strength which lies outside some absorptive potential. In a calculation with the absorptive potential, the nuclei studied had calculated cross-sections which were $\sim$ 44% of the cross sections calculated with the absorptive potential removed. Because the neutron transition density is centered at a larger radius than the proton transition density in these nuclei, a smaller part of the neutron collective strength is lost to absorption. Thus, the method favors neutrons relative to protons.

A sharp cutoff model was developed for this additional nucleon sensitivity in the method. Shell model transition densities were used for each nucleus. Transition densities were summed in proportion to the sensitivity, b_n/b_p, of proton scattering. This value was multiplied by r^4 (one r^2 term comes from the integral over the volume of a sphere and another r^2 term comes from the quadrupole operator) integrated from R to ∞ and squared to obtain a value proportional to the cross section lying outside a given absorptive radius. The radius outside which 44% of the integrated cross section lies was chosen as $R_{absorptive}$. Then, a ratio of the fractions of each nucleon transition strength lying outside $R_{absorptive}$ was taken as the additional nucleon sensitivity.

These additional nucleon sensitivity values ranged from $1.2 - 1.6$. Due to the *ad hoc* nature of this estimate, the uncertainty was estimated as 50% of the effect in each case. The final b_n/b_p value used for a given nucleus was simply a product of the intrinsic and model nucleon sensitivities.

2.1.4 Additional reaction channels

While the goal of this experiment was to measure inelastic excitation cross-sections in (p, p'), a number of other reactions were also observed. These included single and

multiple nucleon removal reactions. Proton pickup and (p,n) exchange reactions could not be observed because these reactions fell outside the momentum acceptance of the spectrograph. The single neutron removal channel $(-1n)$ was of particular interest as it had a large cross section, could populate a different set of states than (p,p'), and held the possibility for relating level population to spectroscopic strength calculated in the shell model.

Single-nucleon removal which occurs as a direct reaction, without transfer, is commonly called *single-nucleon knockout*, or simply *nucleon knockout* [53]. Two distinct groups of reactions are typically included. The first group consists of $(e,e'p)$, $(p,2p)$, and (p,pn), which were used to study the single particle composition of stable nuclei in normal kinematics [54,55]. High bombarding energies and kinematic selection were used to minimize any non-direct components. Extending the technique to short-lived, exotic nuclei required a more efficient technique. Thus, inverse-kinematics nucleon knockout on thick light-ion (^{9}Be) targets was developed. Light ions minimize Coulomb breakup, strong absorption confines single nucleon removal reactions to the surface, and the knockout residues are collected.

Nucleon pickup, i.e. (p,d), is another direct single-nucleon removal reaction in which a proton "picks up" a previously bound neutron from a heavy ion [41]. In either reaction, the removed neutron may come from one of a few valence orbitals, and the $A-1$ daughter nucleus will be left with some probability in one of several final states. Partial cross sections for populating those states are proportional to the spectroscopic factors (C^2S) for neutrons in the ground state of the original nucleus. One can find spectroscopic factors using measured cross sections to specific excited states, or one can use the predicted spectroscopic factors with the measured cross sections to infer the identity (J^π) of the populated excited states.

Unfortunately, the present experiment observed only the neutron removal residues after some interaction with protons. The setup was optimized for inelastic scattering, not knockout. A large fraction of neutron removal residues were collected for

many incoming isotopes, but the fraction which fell outside the focal plane acceptance varied. Furthermore, the neutron removal reaction observed in this experiment includes any reaction channel which populated bound final states in the $-1n$ residue. The observed cross section is a sum over (p,d), direct (p,pn), multi-step (p,pn), and ${}^{A}_{Z}X_{N}(p,p'){}^{A}_{Z}X^{*}_{N} \rightarrow {}^{A-1}_{Z}X^{*}_{N-1} + n$ reactions. This experiment was not designed to separate these contributions.

Experimental studies of inclusive neutron removal reactions due to $\sim$ 100 MeV protons typically do not track the final states populated in residues. Those papers which discuss the states populated in such reactions were mostly performed in the 1950's and 1960's, i.e. before the exclusive reaction techniques became common. Work from that era suggests that 50% of the (p,pn) cross section for masses and energies considered in this thesis comes from direct reactions [56]. Most of the remaining (p,pn) cross section was estimated to come from a two-step process of inelastic scattering followed by nucleon emission. The (p,d) component near 100 MeV proton beam energy was determined to be negligible [57]. Giant resonances carry much of the inelastic scattering strength, and in light nuclei $A \lessapprox 40$, semi-direct neutron emission can give cause the population of final states in the daughter nucleus to follow the spectroscopic factors [58, 59]. So, a significant portion of the inclusive neutron removal reaction considered here can be expected to populate states in the $-1n$ residue in proportion to the spectroscopic factors.

Spectra of γ rays in coincidence with neutron knockout on ^{9}Be were compared to γ-ray spectra measured in coincidence with neutron removal observed in this experiment for selected isotopes. From the γ-ray spectra, the two reactions were found to populate final excited states with similar relative intensities. Figure 2.2 compares the spectra resulting from single-neutron removal of ^{48}Ca on a ^{9}Be target [60] and on the proton target in this experiment. Similar agreement was also observed for $-1n$ reactions on ^{38}Si and ^{41}S [61]. The similarity in excited state populations between $1n$ knockout on ^{9}Be and $1n$ removal on a proton target indicates that the $(p,X)_{-1n}$ reaction populates

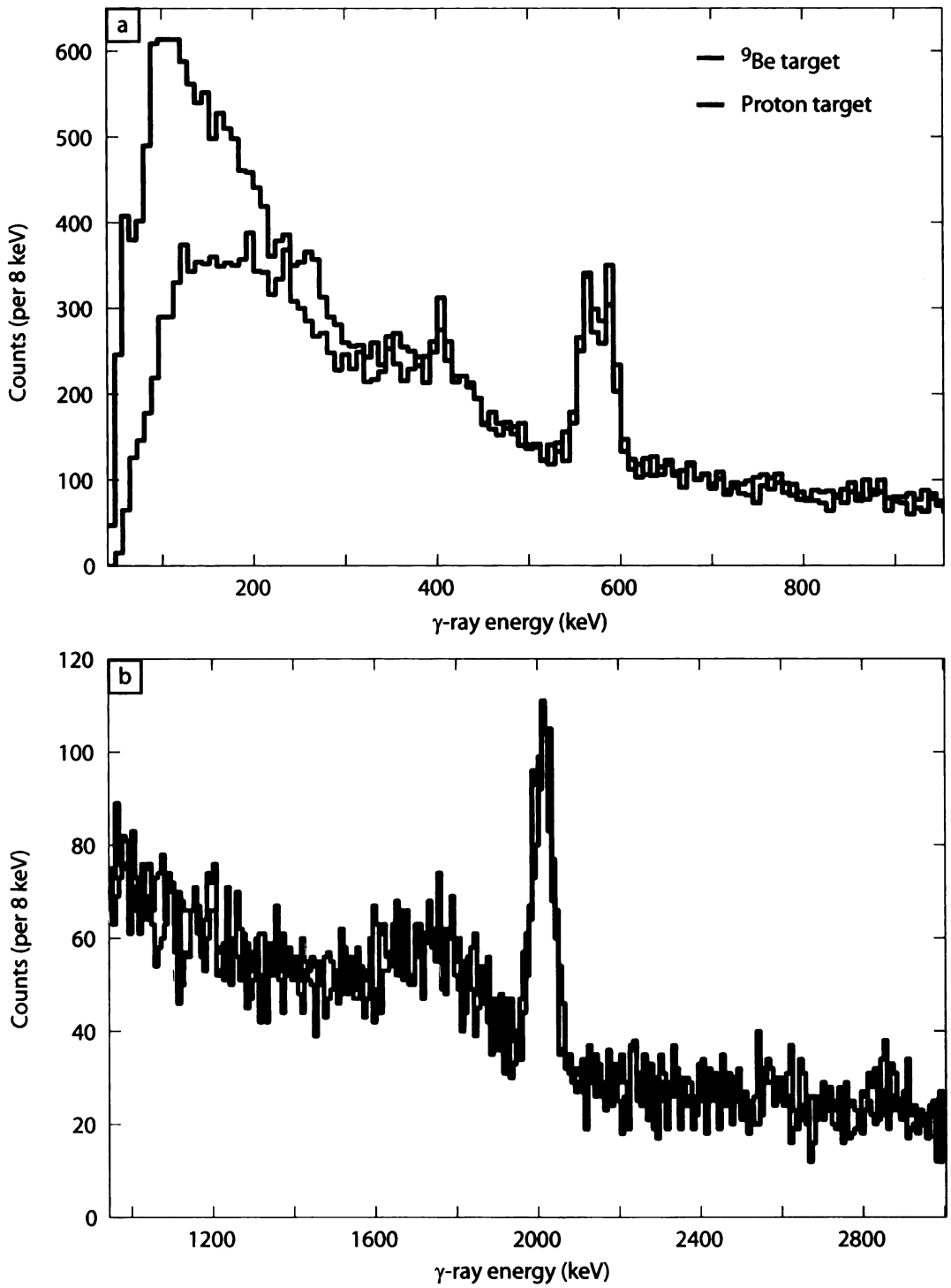

Figure 2.2: Spectra of γ rays in coincidence with single-neutron removal from ^{48}Ca impinging on a ^{9}Be target and on a proton target. The two panels show low and high energy portions of the spectrum. Deviations below 200 keV are likely due to differing levels of low-energy, beam-induced background and different threshold settings.

final states in rough proportion to their spectroscopic factors.

In this thesis, dependence of $-1n$ cross section on spectroscopic factors is used only to assign the second strongest γ-ray transition in even-even residues as the $4_1^+ \rightarrow 2_1^+$ transition. Spectroscopic factors for $-1n$ removal from odd-N, even-Z nuclei filling the $\nu(0f_{7/2})$ orbital favor population of 4^+ and 6^+ states in the even-even residue [62]. Decays predominantly flow through the 4_1^+ state.

2.2 Exotic beam production

Exotic, or rare, nuclei are unstable to β decay and typically have short lifetimes. Isotopes studied in this thesis are neutron-rich and undergo β^- decay with lifetimes ranging from tens to hundreds of milliseconds. So, the experiment must be performed in inverse kinematics with continuous production of the rare isotopes being studied.

Currently, two methods account for most of the production of isotopes far from stability: ISOL and in-flight production [63]. Both utilize nuclear reactions which break apart stable nuclei and use separation techniques to select the isotope(s) of interest. In-flight production may be further separated into projectile fragmentation and projectile fission. The latter will not be discussed in this thesis.

The name ISOL (isotope separation on-line) alludes to the methods historical development. Once research reactors and accelerators became available, nuclear physicists and chemists began creating long-lived, unstable isotopes by bombarding stable isotopes with neutrons and protons. The new isotopes were extracted off-line by removing the material to a lab and performing one or more physical and/or chemical separations. ISOL is essentially the same process but faster with continuous bombardment and extraction. The extracted ions are then separated, accelerated, and used in experiments. In this way, isotopes having shorter lifetimes may be studied.

Advantages of this technique include high production rate for some isotopes, good beam quality, and beam energies comparable to those used at stable beam facilities. Disadvantages include chemistry dependent extraction and beam development, decay losses due to extraction time, and thin secondary targets, which lead to lower reaction rates.

2.2.1 Projectile fragmentation

In projectile fragmentation, a stable heavy-ion beam is accelerated and directed onto a thick production target. A given projectile nucleus may strike a target nucleus while

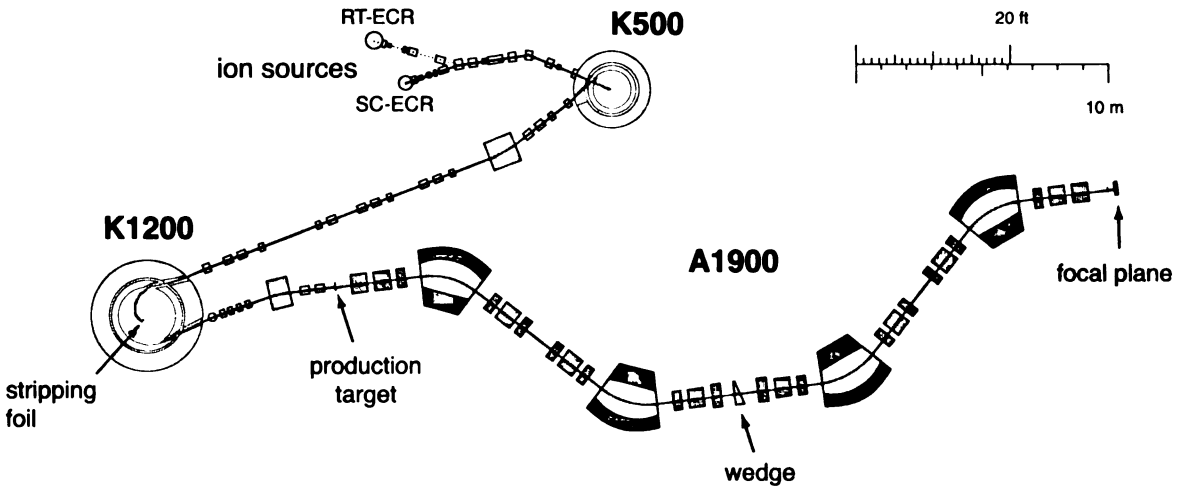

Figure 2.3: Diagram of coupled cyclotrons and A1900 fragment separator

passing through the target. Projectile nucleons in the target-projectile overlap region are removed, and the remaining projectile fragment travels forward with its velocity nearly unchanged [64]. This projectile fragment may then decay by nucleon emission until it has reached a particle stable configuration.

The present experiment was performed at the National Superconducting Cyclotron Laboratory (NSCL) on the campus of Michigan State University (MSU). Figure 2.3 provides a schematic of the Coupled Cyclotron Facility (CCF) [65] and the A1900 fragment separator [66], where the exotic nuclei used in this experiment were produced and selected. Stable ^{48}Ca was extracted from an ion source as beam with 8^+ charge state and injected into the K500 cyclotron. There, the beam was accelerated to an energy of 12 MeV/u, extracted, and injected into the K1200 cyclotron. Inside the K1200, the beam passed through a stripper foil and a beam with 19^+ charge state was accelerated to a final energy of 140 MeV/u. This beam was extracted and delivered to the production target.

2.2.2 Fragment separation and delivery

The 140 MeV/u beam of ^{48}Ca impinged on a 987 mg/cm^2 ^{9}Be target placed at mid-acceptance position of the A1900 [66]. Projectile fragmentation occurred within this

target. Following projectile fragmentation, the outgoing beam is a cocktail composed of unreacted ^{48}Ca and hundreds of stable and exotic nuclei, all having nearly the same velocity. Nuclei are separated in the A1900 fragment separator by the $B\rho - \Delta E - B\rho$ method which utilizes magnetic fields, differential energy-loss, and physical slits. Equation 2.6 defines $B\rho$ with m being the ion rest mass, v the velocity, γ the relativistic factor, and q the ion's charge. For isotope beams in this thesis, one may replace m/q with A/Z.

$$B\rho = \frac{m\gamma v}{q} \tag{2.6}$$

To make optimal use of the beam, a thin wedge was used at the intermediate image of the A1900. This allowed many nuclei to be delivered to the target in a single setting of the fragment separator — such beams are called cocktail beams. To collect data on the six even-A silicon and sulfur isotopes studied in this experiment, two cocktail beams were developed. These will be referred to as dataset 1 and 2 or cocktail beam 1 and 2 in this thesis. Table 2.1 gives the integrated number and mid-target beam energy of even-A silicon and sulfur isotopes incident on the target. Cocktail beam 1 had a momentum acceptance of 0.5%, and cocktail beam 2 had a momentum acceptance of 4% — imposed by the S800 analysis line. The second, more neutron-rich setting was developed with a large momentum acceptance to maximize rate for ^{40}Si.

2.3 Reaction target and detectors

2.3.1 Thick-target, γ-ray tagging method for (p, p')

Starting in the 1950's, proton scattering experiments have been used to study both the elastic and inelastic channels by detecting low-energy protons scattered off thin targets of stable isotopes. Excitation energies in these target were reconstructed from

Table 2.1: Even mass silicon and sulfur isotopes studied in this thesis are listed. The integrated number of nuclei delivered on the LH_2 target and beam energies at the mid-point of the target are listed. The cocktail beam in which each isotope was measured is listed.

Isotope	Cocktail beam (dataset)	Number of nuclei on target ($\times 10^6$)	Mid-target beam energy (MeV/u)
^{36}Si	1	14	90.3
^{38}Si	2	23	99.5
^{40}Si	2	1.6	90.3
^{40}S	1	97	96.0
^{42}S	2	11	103.6
^{44}S	2	36	94.9

measured proton energies and angles. By detecting protons at a number of fixed scattering angles, differential cross sections are measured for scattering to each final state. Starting in 1994 [67], such experiments have also been performed in inverse-kinematics with rare isotope beams [45,68,69]. Here, rare isotope beams impinged on targets containing protons, and low-energy protons were detected in the laboratory close to 90 degrees with respect to the incoming beam, which corresponds to very forward center-of-mass scattering angles. In all experiments where the scattered proton is detected, thin targets ($\sim$ 2 mg/cm^2) are employed to minimize energy straggling. Thin targets also require beam intensities of $\sim 10^4$ particles per second of rare isotope of interest to perform inelastic scattering experiments in a few days. The thick-target method employed here can achieve the same luminosity with beam rates of about 10^4 less.

To expand inelastic proton scattering studies to more neutron-rich nuclei, the thick-target, γ-ray tagging method was developed [70]. Instead of measuring the scattered proton and kinematically reconstructing the excitation energy, γ-rays are detected from decays of states populated in inelastic scattering events. An integrated cross section, defined by the detection of the recoil ion, is obtained. This allows the use of $\sim 100 - 200$ mg/cm^2 thick plastic [$(C_3H_6)_n$] or liquid hydrogen [LH_2] targets. In this case, target thickness is limited by the impact of energy loss of the ion travers-

ing the target on the desired energy resolution of Doppler-corrected γ-ray spectra. The present experiment used the thick-target, γ-ray tagging method to study nuclei with a lower rate limit of $\sim$ 10 particles per second.

This method improves energy resolution ($\sim$ 3% versus 100's of keV), gives additional information through γ-ray branching ratios, and allows for the measurement of long-lived states through changes in the γ-ray response. On the other hand, measuring excitation energy directly determines the state populated; γ-ray measurements are subject to feeding corrections and higher-lying level energies must be deduced from energy sums.

Elastic scattering angular distributions may also be collected but typically have poor angular resolution because the heavy-ion scattering angle is so small in the lab frame. Thus, the optical model cannot be determined locally. In this experiment, the energy and isotope dependent global optical model parameterization of Koning and Delaroche was used [44].

2.3.2 Liquid hydrogen target

The RIKEN-Kyushu-Rikkyo liquid hydrogen target [71] was used in this experiment to maximize the number of proton nuclei in the target while minimizing energy loss and the effect of contaminant atoms. In a plastic target, for example, carbon atoms also cause excitation of the nuclei under investigation, and a background run is required to measure and subtract this effect. The aluminum windows of the liquid hydrogen target cell used in this experiment account for 5.7(2)% of the atom fraction of the LH_2 target cell. Therefore, their contribution to measured excitation cross sections is negligible. Figure 2.4 is a schematic representation of the target system.

Because liquid hydrogen has a low density (0.071 g/cm^3), quite thick targets are required for exotic beam studies. A comparable experiment by Riley *et al.* used a 191 mg/cm^2 polypropylene [$(C_3H_6)_n$] target (i.e. 1.64×10^{22} protons/cm^2) to study ^{46}Ar. In the present work, Doppler-corrected γ-ray spectra were used to measure total cross

sections for exciting particular states by inelastic proton scattering. So, although an increase in target thickness would result in a proportional increase in reaction rate, the effect of target thickness on Doppler reconstruction must be taken into account.

Target thickness adds to the angular uncertainty in the Doppler correction. In a standard solid target experiment using SeGA, the angular resolution is dominated by the detector segmentation, which is 1 cm along the detectors central axis. The nominal target cell thickness chosen for this experiment was 9.0 mm, causing only a small impact on the resulting resolution of Doppler-corrected spectra.

A greater concern is the change in target thickness caused by differential pressure deforming the cell windows. The aluminum entrance and exit windows for this target cell were 0.190 and 0.212 mm thick respectively. During the data runs the target cell was placed into the vacuum of the beam pipe and contained liquid hydrogen at a pressure of 970(20) hPa, or just under 1 atmosphere. This pressure difference

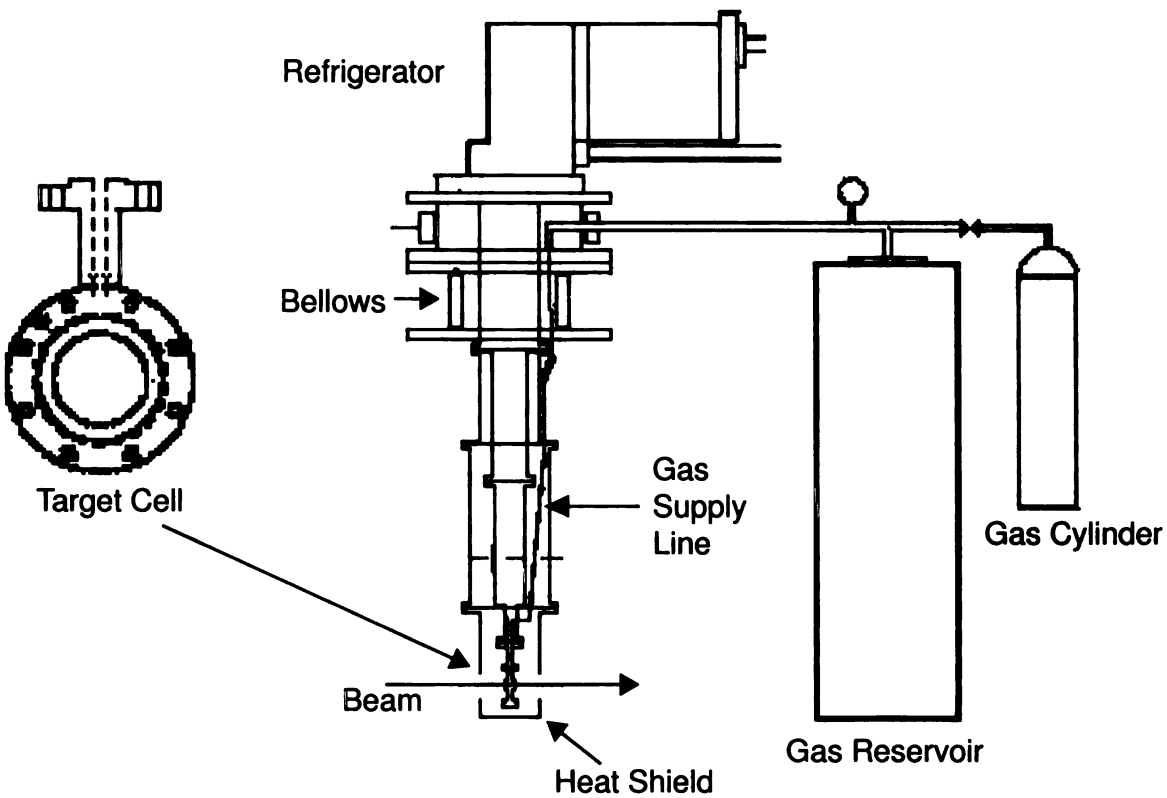

Figure 2.4: Schematic diagram of the RIKEN-Kyushu-Rikkyo liquid hydrogen (LH_2) target system [71].

Table 2.2: Measured maximum thickness of LH_2 cell when deformed by differential pressure. Measurements were performed at room temperature using an inert gas to fill the cell to the desired pressure [72]. The first entry is the nominal value before the aluminum windows were permanently deformed.

Differential pressure (hPa)	Thickness (mm)
flat	9.00
0	10.88
950	11.13
990	11.23

significantly bowed the target windows during the experiment increasing the effective target thickness. Following the experiment, the target thickness was measured with and without differential pressure [72]. Target thickness was measured with calipers at the center of the target windows, see table 2.2.

This measurement gives the maximum target thickness, but a cross-section measurement requires the effective target thickness and an associated uncertainty. Three factors were considered in the calculation of an effective thickness: (i) deformation profile, (ii) beam spot size, and (iii) beam position uncertainty. The deformation profile of a window due to pressure depends critically on the materials response to stresses involved [73]. In the limit of elastic response, the deformation is spherical. At the other extreme, a thick plate may become permanently deformed and both the deformation and its derivative must vanish at the boundary. Equation 2.7 defines the surface elevation of a deformed, clamped plate [73]. Figure 2.5 shows the half-thicknesses of the target in this experiment versus the Y position on the target for 4500 randomly chosen points on the target surface. The spherical model is shown in red and the deformed plate model in blue. Because the target remained deformed even after the differential pressure was removed, the deformed plate model has been used.

$$\Delta = \Delta_{MAX} \times \left[1 - \left(\frac{r}{R}\right)^2\right]^2 \tag{2.7}$$

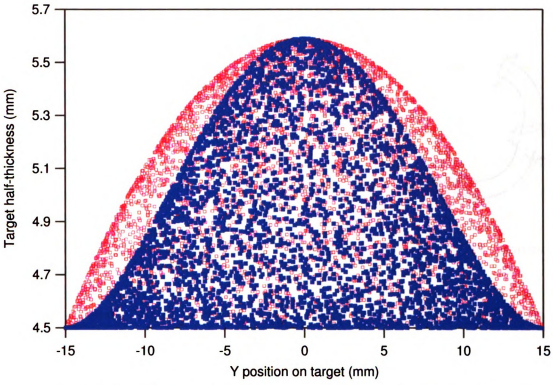

Figure 2.5: Effective LH_2 target thickness for two models of window deformation: the spherical model (red) and the deformed plate model (blue).

The effect of the beam spot was to average over some region of the target. This averaging was computed numerically by random selection of points on the surface of the target, see figure 2.5. An effective thickness was calculated at each point. These thicknesses were weighted according to a Gaussian distributed beam with a FWHM of 1 cm, summed, and normalized by the total probability due to all points. For a known beam position, this gives the effective target thickness.

However, beam position on the target may also vary with the specific fragment cocktail and the alignment of the target with the beam axis. A Gaussian distribution of 1 cm FWHM was taken for the beam position, and effective thickness was calculated as described above for beams centered at varying radii from the true target center. An expectation value for the effective target thickness was calculated to be 0.931 of the maximum target thickness. The range (0.912 – 0.946) contains 69% of the probability, thus these values set the 1-sigma uncertainty in target thickness.

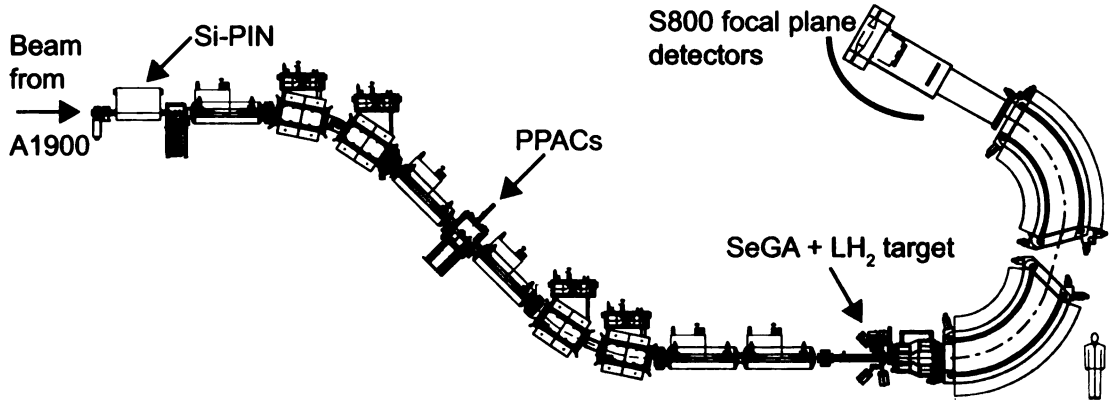

Figure 2.6: The S800 analysis line and spectrograph are shown. The locations of detectors used in this experiment are noted.

Target pressure varied between 950 and 970 hPa during the data runs giving a maximum target thicknesses of 11.18(5) mm. The product of effective target thickness, Avogadro's number, and mass density of liquid hydrogen divided by hydrogen's atomic mass (1.008 g/mol) gives the areal proton density of this target: $4.41^{+7}_{-9} \times 10^{22}$ protons/cm^2. Because the main target volume is quite large compared to the deformation of the windows, the uncertainty in effective thickness is only $\sim 2\%$, comparable to or smaller than typical solid foil uncertainties.

2.3.3 The S800 spectrograph

The S800 analysis line and spectrograph [74] are shown in figure 2.6. The analysis line serves to transport secondary beams prepared by the A1900 fragment separator to the S800 target position where secondary reactions may occur. The spectrograph then selects reaction residues in a particular range of magnetic rigidity and delivers them to the focal plane [75]. Detectors at the object and intermediate image of the analysis line and the spectrograph's focal plane uniquely characterize the nuclei impinging and exiting the reaction target. For the current study, the S800 was used in focused optics mode with a liquid hydrogen cell placed at the reaction target position.

Two optics modes are typically used in the S800 for inelastic scattering and nucleon

knockout experiments with fast beams. Dispersion-matched mode gives the highest energy resolution, but limits the incoming momentum acceptance to 0.5% and results in a momentum-dispersed beam on the reaction target. Focused mode allows for an incoming momentum acceptance of $\pm 2\%$ and results in a focused beam at the target position. Because the present study requires a large momentum acceptance to make efficient use of the projectile fragmentation beam and since the LH_2 target cell has a diameter of 3 cm, focused mode was used. In focused mode, the dispersive angle of a particles trajectory at the intermediate image of the analysis line is proportional to the incoming momentum. The momentum after the target is proportional to the dispersive position measured in the focal plane.

In this experiment, energy loss in a 300 μm Si-PIN detector placed at the object position was measured to determine the charge of each incoming projectile nucleus. Rare isotopes in this study are selected in the A1900 as fully stripped after emerging from the production target. They remain fully stripped when passing through thin transmission detectors and the secondary target at all times due to their high velocity and low atomic number. A pair of X-Y sensitive high-rate Tracking Parallel Plate Avalanche Counters (TPPACs) placed up- and down-stream of the intermediate image determined both the position and angle of each nucleus in the dispersive and non-dispersive planes. In the focal plane, a single Cathode Readout Drift Chamber (CRDC) determined the position of each nucleus in the dispersive and non-dispersive planes. [Note: usually two CRDCs are used to determine both positions and angles, but detector malfunctions left only one working CRDC for this experiment.] Energy loss in an ion-chamber determined the charge of each outgoing nucleus. Finally, time-of-flight was measured between a timing scintillator at the extended focal plane of the A1900 and a timing scintillator in the S800 focal plane for a total flight path of about 58 m.

Of these measured particle identification (PID) parameters, only the angle determined by the TPPACs and the dispersive position measured by the CRDC were used

as quantities needing calibration. Fortunately, the calibration in each case was fixed by the physical size of the readout elements and the detector placement.

Strong kinematic correlations among particle identification parameters offer an opportunity to improve resolution by combining separate measurements on an event-by-event basis. Energy loss parameters for the Si-PIN detector and the ion chamber were corrected for velocity differences of incoming projectiles to give a more uniform response proportional to projectile charge, Z. The largest improvement came from time-of-flight (TOF) correction by dispersive angle and position at the intermediate image of the S800. At that position — when the S800 is operated in focused mode — the dispersive angle is proportional to the relative momentum of a given particle. Thus, for each ion, its angle is proportional to velocity. Because the incoming cocktail beams had momentum widths of 0.5% and 4% $\Delta p/p$, a significant reduction in TOF width occurred. Figure 2.7 shows the dispersive angle versus the raw and corrected time of flight and the one dimensional time-of-flight spectra for ^{42,43,44}S from the second dataset.

From the TPPACs and the CRDC, a measure of the momentum difference due to target interactions was constructed. This longitudinal momentum change parameter was then corrected by the incoming momentum to remove the differential energy loss due to the incoming momentum spread. Transverse momentum is expected to be small in the lab frame due to the forward focusing of reaction products but could not be measured with a single functioning CRDC. Likewise, scattering angle could not be measured. The maximum lab scattering angle kinematically allowed for projectiles scattering off protons in this (p, p') study was $\sim 1.5°$. This falls well within the $3° \times 5°$ nominal angular acceptance of the S800 spectrograph, and no angular acceptance correction is required.

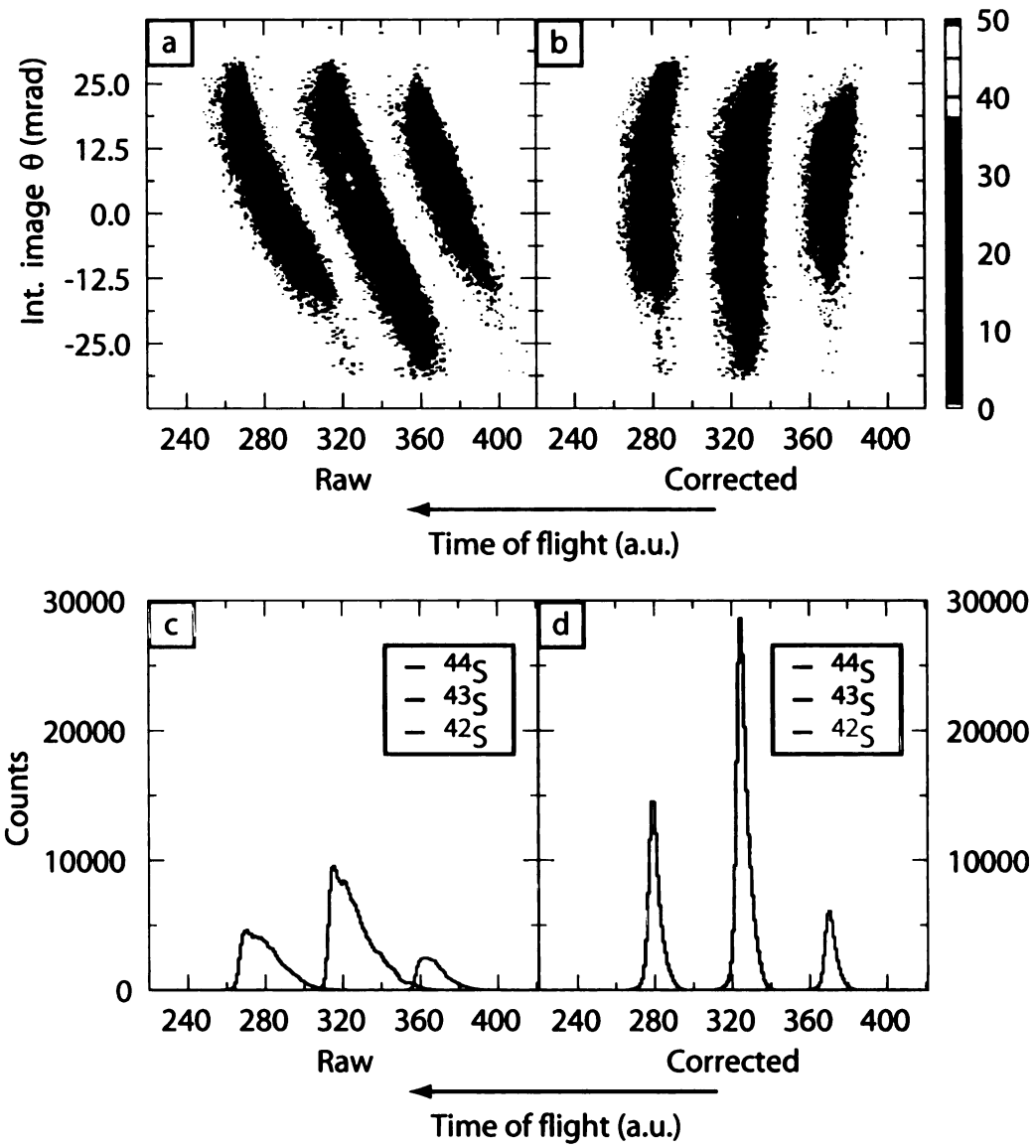

Figure 2.7: Time of flight correlation with incoming dispersive angle is shown. Because dispersive angle is proportional to momentum, it may be used to correct for the velocity spread of the incoming beam. Raw and corrected time of flight show the gain in resolution.

2.3.4 The Segmented Germanium Array (SeGA)

The Segmented Germanium Array (SeGA) is composed of 18 32-fold segmented high-purity germanium (HPGe) detectors [76]. SeGA was designed and built to study nuclei by detecting de-excitation γ rays emitted in-flight. Segmentation of electrical contacts introduce position resolution which aids in Doppler correction of γ rays emitted at roughly 40% of the speed of light.

The detection of γ rays is accomplished by collecting the charges resulting from ionization events within the germanium crystal. Gamma rays may introduce high-energy electrons into the germanium by undergoing the photo-electric effect, Compton scattering, or pair production (which results in a high-energy positron). These lose energy through interactions with electrons in the semiconductor material, and after a short time, the energy deposited has been converted into lattice vibrations and electron-hole pairs. Through proper surface doping, the germanium semiconductor is made into a diode, which is depleted of free charges by reverse biasing with a high voltage. When a γ ray deposits energy creating electron-hole pairs, the electrons and holes drift toward the biasing electrodes and are collected.

In SeGA, the germanium crystals are cut to form cylinders with a coaxial cylindrical well. The central contact (in the well) collects all electrons excited into the conduction band. The outer contact (on the surface of the cylinder) is divided into eight slices along the cylinders axis and four quadrants in the azimuthal direction. Thus, one or more of the 32 outer segmented contacts may collect the holes.

The energy measurement from SeGA detector central contacts was calibrated using a number of known γ-ray transitions from radioactive sources ranging from 81 to 3253 keV. While this calibration is expected to be linear for a semiconductor, non-linear effects arising from the amplification chain or the analog-to-digital conversion are possible. Here a quadratic calibration was used; the energy residuals after calibration for 15 of the 16 detectors used were remarkably similar. (The detector in SeGA electronics channel 3 required a three-part calibration with two linear sections

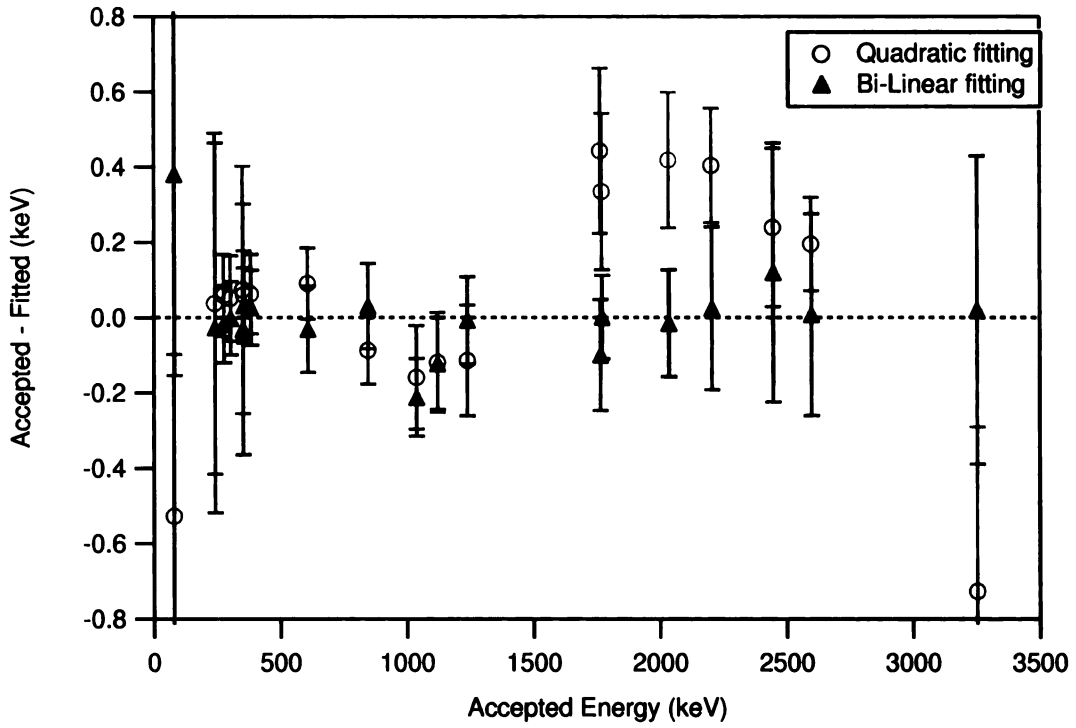

Figure 2.8: Energy residuals for 15 of 16 SeGA detectors following calibration. Results are shown for the quadratic function currently used and a two-part piecewise linear function.

and one quadratic section.) The averaged energy residuals for those 15 detectors are shown in figure 2.8. A two-part piecewise linear calibration was also attempted, but not used in the data analysis. To minimize free parameters, each detector was allowed one slope and intercept for variation; global linear relations between the slopes and offsets in the two linear pieces were varied; and a global cutoff between the two linear pieces was varied. The global fit residuals for this two-part piecewise linear calibration are substantially smaller, and more importantly, have little or no trend with energy. Future versions of the SeGA calibration routines should include such a bilinear calibration.

The efficiency for full-energy detection of γ rays was measured as a function of energy using calibrated sources between 81 and 1528 keV for absolute measurement. To extend the energy range of the measured efficiency to 3253 keV, uncalibrated ^{56}Co and ^{226}Ra sources with multiple γ rays of known branching ratios were used.

Table 2.3: A list of sources used for γ-ray efficiency calibration. Sources with documented absolute calibrations are listed with their relative uncertainties. The Mixed source contained nine radionuclides; most had short half-lives and were not used due to low peak intensity. Transitions arising from decays of ^{137}Cs and ^{60}Co in the Mixed source were used.

Source ID	Parent isotope	Measurement conditions	Calibration (rel. unc.)
H7141	Mixed	beam pipe only	absolute (2.1, 1.6%)
H7961	^{133}Ba	beam pipe & in-cell	absolute (3%)
Z2707	^{152}Eu	beam pipe only	absolute (1.4%)
Z7044	^{226}Ra	beam pipe & in-cell	relative to Z2707
FSU(1)	^{56}Co	beam pipe only	relative to Z2707

In these cases, the source efficiencies were scaled in an energy region overlapping the calibrated sources. The most precise source (^{152}Eu, serial number Z2707) had a relative uncertainty of 1.4%; uncalibrated sources were scaled relative to this source. Since this experiment uses a liquid hydrogen (LH_2) target enclosed in an aluminum target cell, efficiency data was collected both in and out of the cell to verify correct modeling of the target cell in the simulation. The size of the cell restricted the sources which could be measured inside the target cell. Efficiency results are displayed in figure 2.10.

The high-velocity of the nuclei at the moment of γ ray emission leads to a Doppler shift in the measured energies (see below) and a Lorentz boost which effects the angular distribution of γ rays. Both of these relativistic effects and a number of kinematic uncertainties are included in a **GEANT** [77] simulation of in-flight SeGA γ-ray detection. This simulation includes the photon scattering and attenuation due to beam pipe, target cell, and detectors. Figure 2.9 shows the geometry used in the **GEANT** simulation.

Response functions generated in this simulation are used in fitting the Doppler-corrected γ ray spectra, and the scaling found in the fit is used to calculate cross-sections. The ratio of the measured to the simulated efficiency must be applied as a correction to the cross-section. Figure 2.10 shows the **GEANT** simulated efficiencies for a source in the beam pipe and a source in the target cell superimposed on the

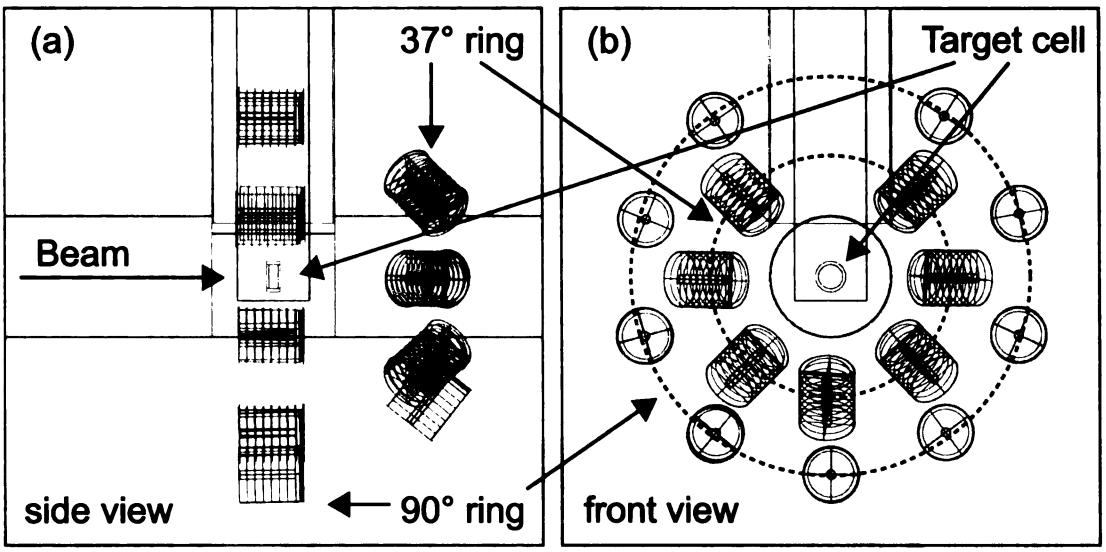

Figure 2.9: The geometry used in GEANT [77] simulations of this experiment is shown. from side and front viewpoints. The SeGA detectors surround the LH_2 target cell in two rings at 37° and 90°.

measurements. The ratio of measured to simulated efficiencies is shown in figure 2.11. Above 600 keV, the simulation systematically underestimates the efficiency. Below 600 keV, a sharp transition to overestimation occurs. Above 600 keV, a constant scale factor of 1.01(3) may be used. The scale factor uncertainty includes the scatter of scale factors and uncertainty in absolute source efficiency. Because the LH_2 was not present during the efficiency measurements, and the inclusion of LH_2 led to unphysical effects in the simulation, the small γ-ray attenuation due to passage through the LH_2 was included as a γ-ray energy dependent correction to the cross-section. This correction was typically less than 1% and an uncertainty of 20% of the correction was included.

Nuclei produced by projectile fragmentation have velocities that are a significant fraction of the speed of light ($v \sim 0.4c$ in this study). To minimize losses, these exotic nuclei are often studied in-flight (i.e. without being stopped and reaccelerated) in inverse kinematics (i.e. the beam is being studied and the target is probe). This allows for the use of thick secondary targets, which in turn, maximizes reaction yields; kinematic forward-focusing often leads to collection of a large fraction of reaction products.

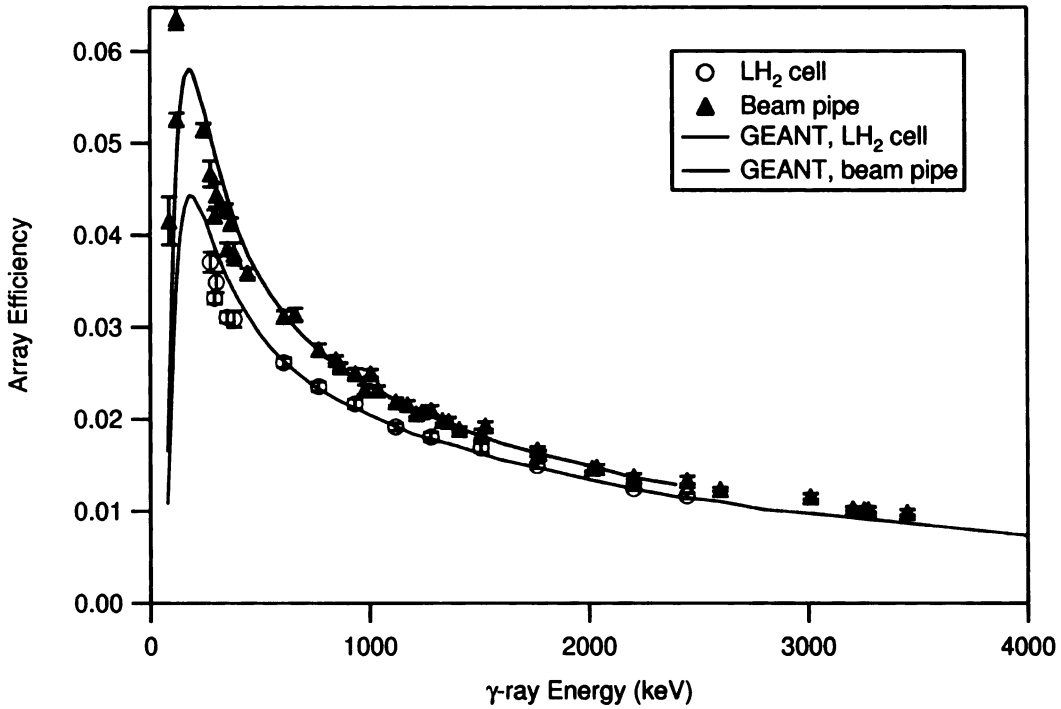

Figure 2.10: SeGA full-energy efficiency is plotted as a function of energy for calibrated source measurements and GEANT simulations. Data are shown for sources placed in the beam pipe (analogous to a standard SeGA measurement) and for sources placed in an empty LH_2 cell.

The method maximizes reaction rate, but introduces problems in determining what reaction took place. In normal kinematics, stable isotope experiments, the reaction rate is not a dominant concern, and thin targets may be used. Often, a complete kinematic description of each reaction event could be determined by detecting both the beam and target reaction products. In other cases, γ-ray detection was used to detect decay transitions from excited nuclei stopped in the target. When the stopping time is much shorter than the excited state lifetime, the γ rays are emitted from rest and are detected with an energy resolution determined solely by the detector.

In experiments using projectile fragmentation beams on thick targets, target thickness precludes a kinematic reconstruction of the scattering event because the scattered target either stops inside the target or its energy is poorly defined due to target straggling. Since γ rays may exit the target without energy loss, they are used to probe

which state was excited in a given scattering event. The γ-ray energy observed in the lab is related to the energy of the emitted γ ray in the projectile frame by the Doppler shift (see Eq. 2.8). However, uncertainties in the velocity of the nucleus emitting the γ ray and the angle of emission cause significant uncertainty in the deduced γ-ray energy.

$$E_{projectile} = E_{lab} \times \gamma \left[1 - \beta \cos\left(\theta\right)\right] \tag{2.8}$$

The external contact of the HPGe diodes are segmented into eight slices and four quadrants in the SeGA detectors. By detecting the net charge deposited in each of these 32 segments, one may estimate the location of the first interaction of a γ-ray scattering inside the detector. Currently, the favored algorithm is Hit-On-Max which uses the geometric center of the segment with the largest energy deposited as the location of the first interaction point. Knowing this first interaction point and the

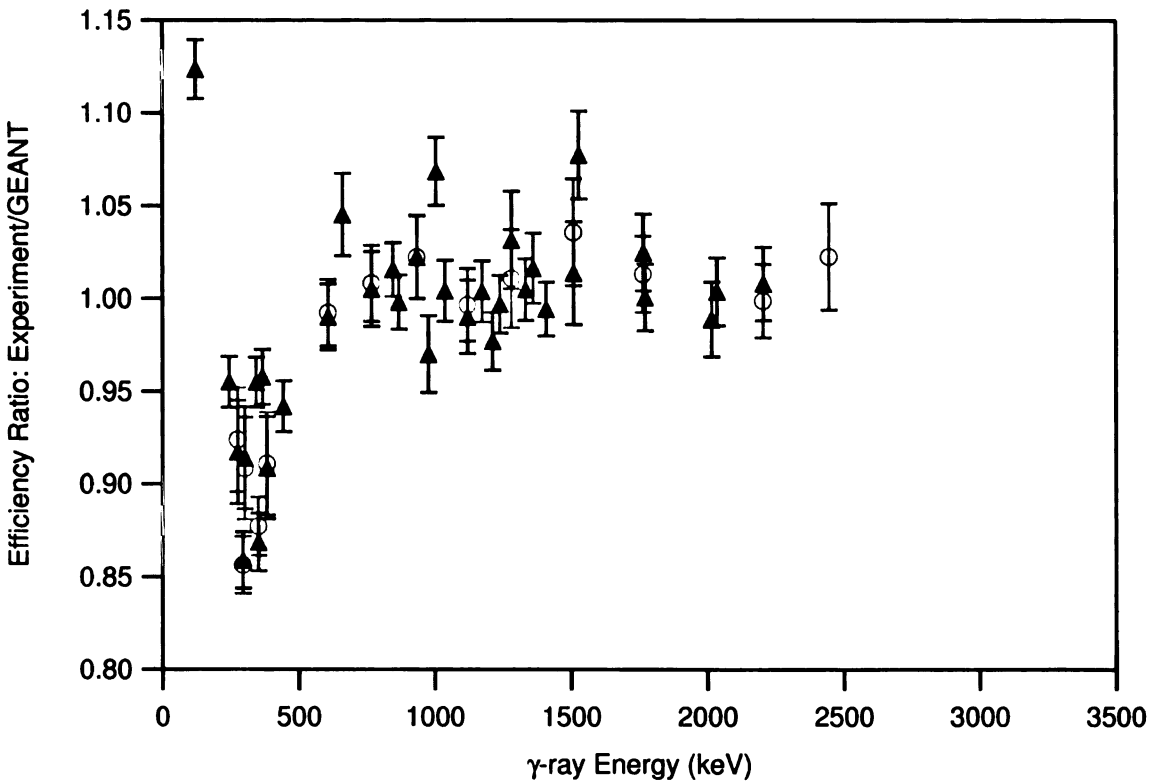

Figure 2.11: The ratio of measured SeGA full-energy efficiency to GEANT simulated full-energy efficiency is plotted as a function of energy.

location of γ ray emission (typically taken as the center of the reaction target), one can determine the angle between the γ-ray emission vector and the beam particles velocity vector. This gives the $cos(\theta)$ term in the Doppler correction formula, Eq. 2.8. The beam velocity may be determined for a given isotope from its position in the S800 focal plane and the $B\rho$ setting of the spectrograph.

The detectors are typically arranged at a fixed distance from a reaction target in rings at specific angles with respect to the beam axis. In the present work, a ring of seven detectors at 37° and another ring with nine detectors at 90° were placed with the centers of the crystals approximately 24 cm from the center of the LH_2 target. Only 16 of the 18 detectors could be used due to space constraints. To minimize the angular uncertainty, the segmentation axis is oriented to be perpendicular to a line connecting the target and detector centers and is coplanar with the beam axis. Figure 2.9 illustrates the relative SeGA detector and target positions.

2.4 Systematic corrections and uncertainties

This section describes corrections and systematic uncertainties applied to cross sections computed in the next chapter. Uncertainties listed here are added in quadrature to the statistical uncertainties obtained from fitting and feeding corrections. Table 2.4 presents the corrections and uncertainties which were applied to the 2_1^+ excitation cross section of ^{36}Si. Correction values were defined as the estimated change in γ-ray yield with respect to the baseline assumptions for a fixed cross section. The product of all corrections gives the total correction. Because the cross sections are calculated based on measured numbers γ-ray events, the cross section is multiplied by the reciprocal of this correction. The determination of these correction values and uncertainties are explained in the remainder of this section.

Target thickness was discussed in section 2.3.2. This correction is the ratio of the average target thickness — integrated over some beam spot — to the maximum

Table 2.4: Systematic correction and uncertainty table for ^{36}Si

Correction	Uncertainty	Description
0.931	0.022	target thickness
1.011	0.030	efficiency ratio: experiment / **GEANT**
0.993	0.001	γ-ray attenuation in LH_2
1.040	0.020	γ-ray angular distribution
0.990	0.005	momentum loss cut
0.962	0.042	total
1.039	0.046	total^{-1} = cross section correction

thickness. Measured and **GEANT** calculated γ-ray efficiencies were discussed in section 2.3.4 and plotted as a function of γ-ray energy in figure 2.10. All γ-ray transitions observed in this thesis have energies above 600 keV. Therefore, a constant scaling between experiment and simulation has been used. Attenuation of γ rays due to interactions with the liquid hydrogen in the target are computed using standard photon attenuation coefficients [78] instead of being included in the **GEANT** simulation; this correction depends on γ-ray energy.

Figure 2.12 shows the γ-ray angular distribution in the projectile frame, which was calculated from statistical tensors output by **ECIS** [39, 79]. The quantity $W(\theta) \cdot \sin\theta$ is shown due to the implementation of γ-ray angular distributions within the SeGA **GEANT** code [80]. Because γ rays were detected over a large range of reaction scattering angles, the integrated effect is small. SeGA detects γ rays at 37° and 90° in the lab frame — giving emission angles near 45° and 135° in the projectile frame — further minimizing the effect of any angular distribution.

Although proton scattering events are not cut by the angular acceptance of the S800 focal plane, the momentum loss gate which separates the inelastic and $-1n$ reaction channels introduces a cut on center-of-mass scattering angle, see section 3.1.1 for gating details. Figure 2.13, panel (a) shows the differential cross section as a function of center-of-mass scattering angle for inelastic excitation of the 2_1^+ state of ^{40}S by 100 MeV protons calculated by **ECIS** [39]. Panel (b) shows the same cross section as but differential with respect to scattering angle, not solid angle. In the

lab frame, the scattering event involves a momentum transfer from the beam particle to the target proton. The relationship between longitudinal momentum transfer — i.e. along the beam axis — and center-of-mass scattering angle was calculated using relativistic kinematics and is shown in figure 2.13, panel (c). A cut on longitudinal momentum transfer is then equivalent to a cut on center-of-mass scattering angle and requires an acceptance correction. Because each cocktail beam had a different intrinsic momentum width, the gating varied a small amount between cocktails to keep $1n$ contamination to a minimum. Figure 2.13, panel (d) shows the fraction of the total inelastic excitation cross-section lost due to the gates used in datasets 1 and 2. This calculation was used for all isotopes.

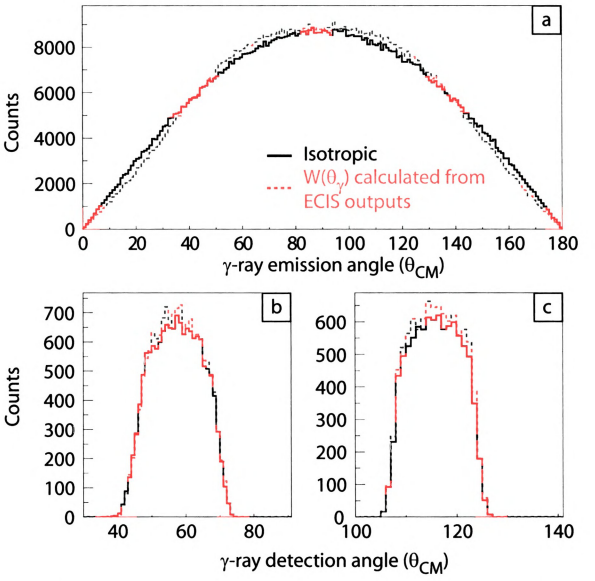

Figure 2.12: Gamma-ray angular distribution from (p, p') (dashed line) is compared with an isotropic angular distribution (solid line) in the projectile frame (a). The quantity $W(\theta) \cdot \sin\theta$ is shown due to the SeGA `GEANT` code implementation. Panels (b) and (c) show the projectile frame angular distribution of γ-rays detected in the 37° and 90° rings of SeGA.

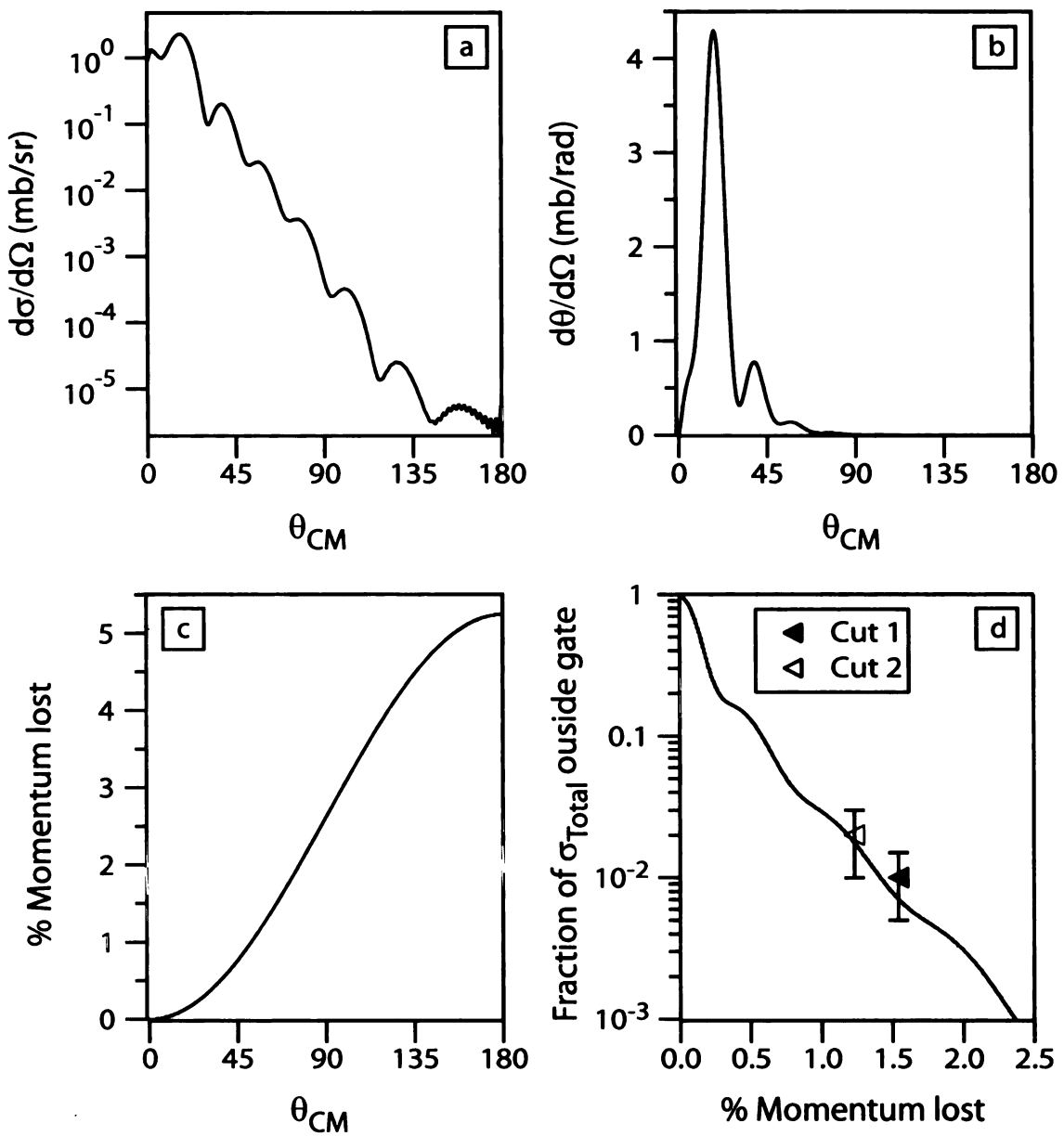

Figure 2.13: Calculated differential (p, p') cross sections for excitation of the 2_1^+ state in ^{40}S per unit solid angle (a) and per unit scattering angle (b). The relationship between momentum lost along the beam axis by the scattered ion in the lab frame and scattering angle in the center-of-mass frame is shown (c). The fraction of the total cross section not observed due to momentum gating losses is calculated as a function of momentum loss (d). For each dataset, the momentum loss gate position and effect on cross section are shown with error bars.

Chapter 3

Analysis

3.1 Particle and reaction channel identification

Particle and reaction channel identification were crucial to the extraction of inelastic excitation cross sections ($\sigma_{p,p'}$) in this experiment. While such gating is always important in intermediate-energy, thick-target experiments, a quick example makes clear the necessity of proper gating in this experiment. Table 3.1 lists the four incoming isotopes giving the highest absolute yields for the $2_1^+ \rightarrow 0_1^+$ transition in ^{38}Si. These isotopes were measured with a single incoming cocktail beam. The channel of interest — $p(^{38}\mathrm{Si},^{38}\mathrm{Si} + \gamma)\mathrm{p}'$ — gives the 3^{rd} largest γ-ray yield. Thus, clean identification of incoming particle and reaction channel are required.

Table 3.1: Incoming particles and $2_1^+ \rightarrow 0_1^+$ γ-ray yields for reactions populating ^{38}Si.

Incoming isotope	Number of beam particles ($\times 10^6$)	Area of 1077 keV ^{38}Si peak
^{41}P	77	500
^{39}Si	7	490
^{38}Si	23	400
^{40}P	58	140

3.1.1 Event selection

The final set of gates was the result of an iterative process; only the final gating solution is discussed here. To extract a cross section without physical bias, one must ensure that neither the gates applied nor the experimental setup itself introduces any physical bias. To that end, gating for the two datasets was developed in parallel. When applicable, gates were constucted with uniform geometries and positioned in a consistent way relative to peak centroids in the relevant parameter space. So, all incoming isotopes were treated consistently, and trends and parameter correlations were treated simultaneously for all gates. All particle and reaction channel gating were performed using the code `SpecTcl` [81].

Specifically, the inelastic channel gating requires that the unreacted beam and the inelastically scattered beam be treated equally. Equal treatment must be confirmed because a change in longitudinal momentum occurs in the scattering process, see section 2.4. Detection efficiencies cancel in the cross section calculation as long as their is no preference with respect to momentum.

The inelastic/$-1n$ gates for a given isotope is the **AND** of the following gates:

- Valid particle
  - TPPAC — Intermediate image center
  - PIN-IC — both detectors have reasonable energy loss
  - CRDC1 single hit — exactly one hit recorded in multi-hit TDC
- PIN-IC — select the change initial & final proton number
- PIN-TOF — select incoming isotope
- IC-TOF — select outgoing isotopes
- Momentum Loss-TOF — select the final mass

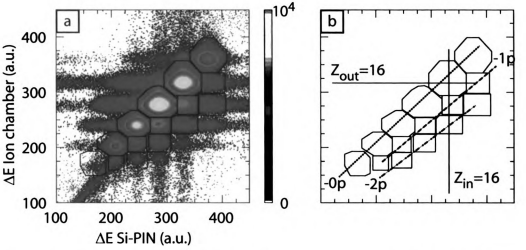

Figure 3.1: Energy loss after the target $\Delta E_{ionchamber}$ versus ΔE_{Si-PIN} is plotted for the second dataset. Gates select charge (Z) of ions before and after reactions on the LH_2 target.

Valid particle selects events in which all required particle detectors had reasonable values. Figure 3.1 shows energy loss in a detector after the target ($\Delta - E$ ion chamber) plotted versus energy loss in a detector before the target ($\Delta - E$ Si-PIN). Here the incoming and outgoing projectile charges are selected.

Choosing events with the same number of protons (Z) before and after the target selects the $-0pxn$ channels, i.e. the (p, p'), $-1n$, and $-2n$ channels. Incoming isotopic selection was made in the $\Delta - E$ Si-PIN versus time of flight (TOF) spectra for each dataset, shown in figure 3.2. Here each horizontal line is one isotopic chain with mass increasing from right to left. The outgoing $-0pxn$ channel was again selected in the $\Delta - E$ ion chamber versus time of flight (TOF) spectra. Figure 3.2 shows incoming isotopes are especially well-separated in the dataset containing ^{40}S. This is because $B\rho$ selection of a projectile fragmentation beam causes the TOF parameter to vary as M/Q. For the fully-stripped ions studied here, this is simply A/Z. The first dataset selects isotopes near ^{40}S, thus $A/Z \sim 2.5$. This give optimal PID separation by placing the TOF centroids of the $Z \pm 1$ nuclei exactly between the TOF centroids of a given isotopic chain.

The separation is less than optimal in the second dataset, figure 3.2 panel (d). The

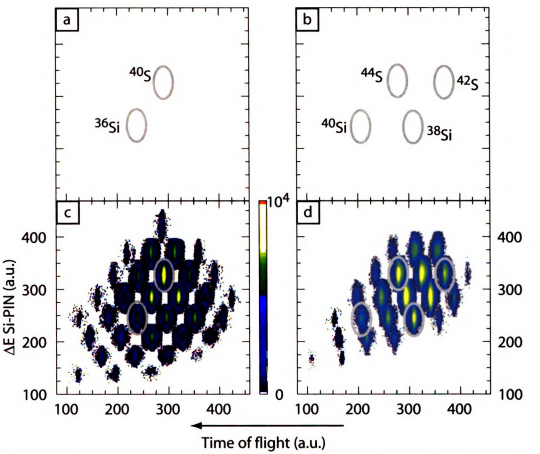

Figure 3.2: Incoming particle identification (PID) plots for both incoming cocktail beams. Panels (a) and (b) show the locations of isotopes studied in this thesis for the first and second cocktail beams, respectively. Panels (c) and (d) show the data for the respective settings with the isotope locations as marked in panels (a) and (b). A logarithmic color scale is used.

worst observed separation occurs for diagonal neighbors in the $\Delta - E$ ion chamber versus time of flight (TOF) spectrum for this second dataset. Figure 3.3 presents a magnified view of this spectrum. Possible contamination was investigated by selecting a diagonal grouping of isotopes, including ^{44}S and ^{38}Si. Panels (b) and (c) of figure 3.3 show the selected region and a projection onto a diagonal line running parallel to the group. The gaussian estimate for particle misidentification is $\sim 9 \times 10^{-4}$ of the given peak area. Contamination of particle identification gates, therefore, gives a negligble contribution to the cross-section uncertainty.

Finally, the (p,p'), $-1n$, and $-2n$ channels were separated on the basis of momentum lost while passing through the target. The momentum loss parameter is described in section 2.3.3 and is sensitive to differences in the logitudinal momentum change. Figure 3.4 shows the momentum loss versus time-of-flight spectrum gated for $-0pxn$ reactions arising from incoming ^{42}S. A residual correlation in the parameters is present because all TOF corrections were based on detectors before the target. Proton scattering, $-1n$, and $-2n$ channels were initially separated by diagonal cuts in such 2-D spectra. These cuts were made individually as the momentum loss parameter was not calibrated for incoming mass and charge. To remove the $-1n$ contamination from the (p,p') γ-ray spectra and to standardize the momentum loss cut, a time-of-flight, incoming-isotope corrected momentum loss parameter was created. Panel (b) of figure 3.4 shows a corrected momentum loss spectrum for the final inelastic gating compared with the $-1n$ events which had contaminated the inelastic spectrum and the $-1n$-gated events. Figure 3.5 (a) shows the corrected momentum loss versus the Doppler-corrected γ-ray energy of the original inelastic gating. Above momentum loss channel 320, the spectrum changes. Figure 3.5 (b) presents the original, final, and contaminant-gated Doppler-corrected γ-ray spectra.

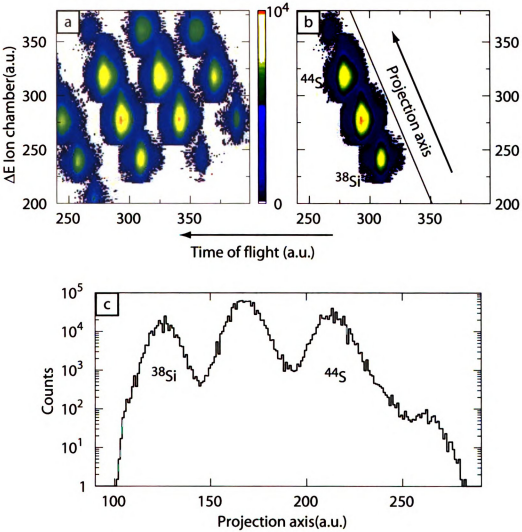

Figure 3.3: PID overlap was checked in the $\Delta E_{Ionchamber}$ vs. time of flight spectrum for the second beam setting. A diagonal selection of isotopes was made and projected on to the axis shown in panel (b). Overlap of neighboring isotopes in panel (c) is below 10^{-3} of total number of counts for a given isotope, which is negligible in this analysis.

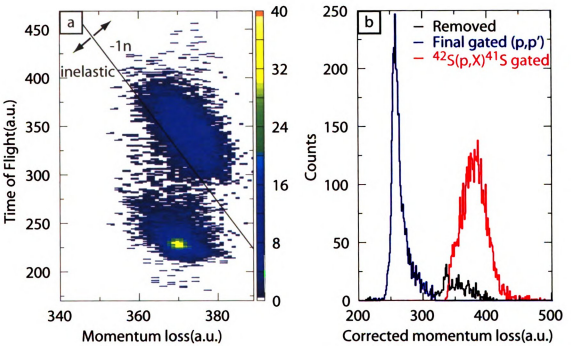

Figure 3.4: Initial momentum loss gating is shown in panel (a) for the ^{42}S $-0pxn$ channel. After correcting for time of flight, incoming mass, and incoming charge, panel (b) shows the corrected momentum loss spectrum.

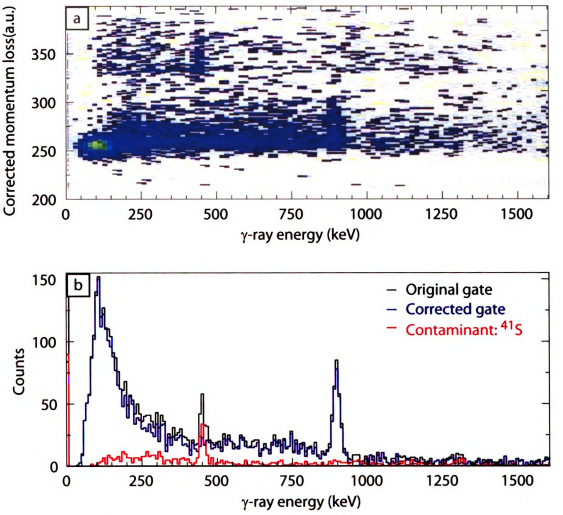

Figure 3.5: Corrected momentum loss is plotted versus Doppler corrected γ-ray energy for the original inelastic gating shown in figure 3.4 (a). Above momentum loss channel 320, the spectrum clearly changes. The original and final gated γ-ray spectra are superimposed in panel (b). Also shown is the spectrum corresponding to $-1n$ channel γ rays.

3.2 Analysis of γ-ray spectra

After events were selected according to incoming beam particle and reaction channel, gated γ-ray spectra were produced for the nuclei of interest. The following sections will focus on the analysis of the γ-ray spectra of ^{36,38,40}Si and ^{40,42,44}S measured in coincidence with (in)elastic scattering in the LH_2 target. The gating and analysis for each isotope was handled in a consistent fashion and is outlined here.

The incoming nuclei and (in)elastic scattering were selected by taking an AND of the gates described in section 3.1. Spectra are Doppler corrected on an event-by-event basis according to Eq. 2.8. The beam velocity, β, is determined for a nucleus from the focal plane dispersive position and the magnetic rigidity of the S800 spectrograph. The γ-ray emission angle is calculated from measured segment positions and a fixed target center.

To reduce random coincidences for the inelastic-scattering γ-ray spectra, a timing cut was added to select only γ-rays in a prompt time window of 60 ns. The timing parameter has been corrected for the time of flight between the target and the S800 focal plane. Due to an energy dependence in the triggering time of the SeGA detectors, γ-rays depositing $\lesssim$ 600keV may be prompt, but fall outside this timing cut. While a linearization of the time response could be performed, a strong, low-energy γ background in the inelastic channel would still affect this energy region. Spectra were investigated with and without this cut, and no low-energy peaks were observed for the inelastic-gated spectra of the nuclei currently under study. A study of efficiency loss due to the timing cut will be necessary to extract inelastic excitation cross sections from the neighboring odd-mass and odd-odd nuclei.

The remaining background in each inelastic-gated spectrum was due primarily to beam interactions with the aluminum windows of the LH_2 target cell. This background was measured by raising the target cell temperature above the boiling point of hydrogen. The magnetic rigidity of the S800 spectrograph was then increased to

compensate for the reduced energy loss of ions traversing the cell. This data was then analyzed to extract the γ-ray spectrum in coincidence with events which would satisfy an (in)elastic scattering gate. The total number beam particles contributing to this spectrum was computed from the number of down-scaled events satisfying the gate multiplied by the downscale factor. In the following sections, this collection of γ-ray events has been Doppler corrected using the $\beta_{projectile}$ appropriate for each nucleus and scaled in proportion to the number of incoming beam particles to form the beam-related background for each inelastic spectrum.

The sum of all individual SeGA detector spectra is used for fitting. Detectors were also summed by rings to check full-energy peaks for energy shifts relating to the lifetime of a particular state. Other than the previously measured lifetimes of the $2_1^+ \rightarrow 0_1^+$ transitions, no lifetime shift large enough to affect the analysis was observed. Spectra have been fit using response functions generated by a **GEANT** [77] simulation of SeGA added on top of this scaled background spectrum. The scale and position of each response were fit to find the number of γ-rays emitted and the energy centroid of the peak. Fits were performed in **PAW** [82] using the negative log-likelihood option of **Minuit** [83].

The SeGA **GEANT** simulation was written by Dr. W. F. Mueller to address the variation of Doppler-corrected peak shape with experimental conditions [80]. Experimental uncertainties including the finite segment size of SeGA, projectile scattering angle, energy loss through the target, physical thickness of the target, and lifetime of a decaying state may change the width — and sometimes position — of the reconstructed γ-ray peak. The simulation accepts information on the target, beam, and emitted γ-ray, then applies the appropriate Lorentz transformation on the γ-ray emitted in the projectile frame to find its lab-frame properties, and simulates the γ-ray interactions with SeGA. Then, the γ-ray is reconstructed as in the experiment, using an average velocity and the angle of the center of the segment receiving the most energy.

Cross sections for γ-ray production were calculated according to the definition of cross section.

$$\sigma = \frac{N_{reactions}}{N_{beam} \cdot (N/A)_{target}} \tag{3.1}$$

The terms $N_{reactions}$ and N_{beam} denote the total numbers of γ rays emitted due to reactions and incoming beam particles, respectively. $(N/A)_{target}$ is the number of target nuclei per unit area, also called the areal number density of the target. Note that this is not a level population cross section. The level population cross section is given by adding the cross sections for γ-rays which decay from a given level and subtracting the cross sections of those γ-rays which decay to that same level.

3.2.1 ^{36}Si

Prior to this experiment, the only published γ-ray information on ^{36}Si was the intermediate-energy Coulomb excitation work of Ibbotson *et al.* [84]. They observed a single peak at 1399(25) keV and labeled it as the $2_1^+ \rightarrow 0_1^+$ transition. Figures 3.6 - 3.8 show three views of the γ-ray spectrum observed in coincidence with $p(^{36}\mathrm{Si},^{36}\mathrm{Si}{+}\gamma)\mathrm{p}'$. The dominant peak in the full spectum is clearly near 1400 keV, but the spectrum is significantly above background at high energies.

Because γ-ray responses feature a peak with some low-energy continuum, fitting often proceeds from high energies to low energies. Often the full-energy peak (also known as the photopeak) will be fit; then its intensity will be fixed and used to fix its contribution to lower-energy background due to any escape peaks and the Compton continuum. However, these Doppler-corrected peaks are broadened compared to traditional forward-kinematics, or lab-frame, peaks. Thus for Doppler-corrected spectra, the relative importance of the full-energy peak is diminished, and the Compton edge and escape peaks may significantly decrease the uncertainty in a fit.

Fitting of the ^{36}Si spectrum was split into two energy regions, 1700-5000 keV

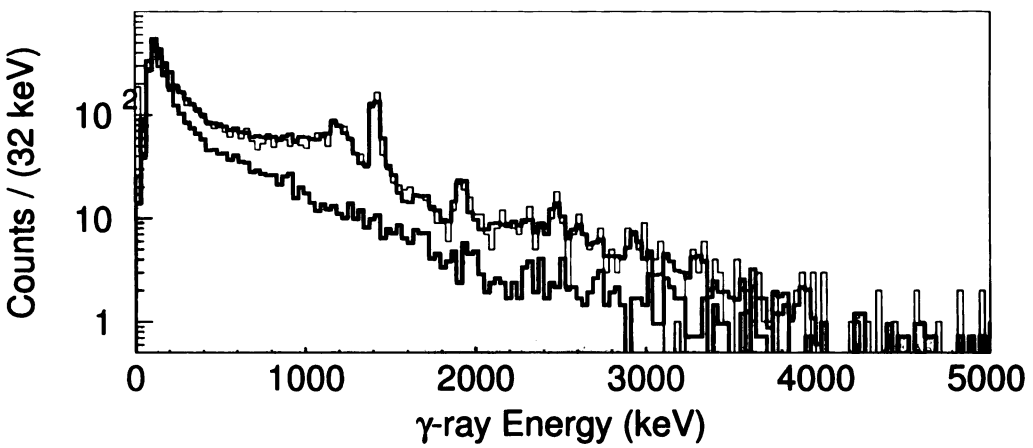

Figure 3.6: Full γ-ray spectrum of ^{36}Si. The background (grey-filled) and fit (blue) are superimposed on the full spectrum (black).

and 1000-2100 keV, shown in Figs. 3.7 and 3.8, respectively. First, the high-energy fit was performed stepwise from high to low energy. Each peak was added, fit in a narrow region about the full-energy peak, and fixed. Once all peaks were fit, the fit was performed once again with all peak parameters allowed to vary. Figure 3.7 shows the resulting peak fit. The solid line histograms are the measured and fitted spectra; grey fills the top of the fit spectrum histogram. Filled histograms of various colors show the fitted response functions. These are stacked, to show their sum, with the window background as grey as the top member of the stack. The window background is jagged compared to the response functions and was placed at the top to preserve the visual clarity of this figure. Smoothing was not performed on the background because several distinct feature arise from lab-frame γ rays being Doppler corrected to the projectile frame.

The step-wise fitting procedure was then repeated in the low-energy region with the high-energy peaks fixed. The high-energy responses contributed a nearly flat continuum component in this region. The peak near 1900 keV was allowed to vary to take advantage of its Compton continuum. Figure 3.8 shows the resulting peak fit.

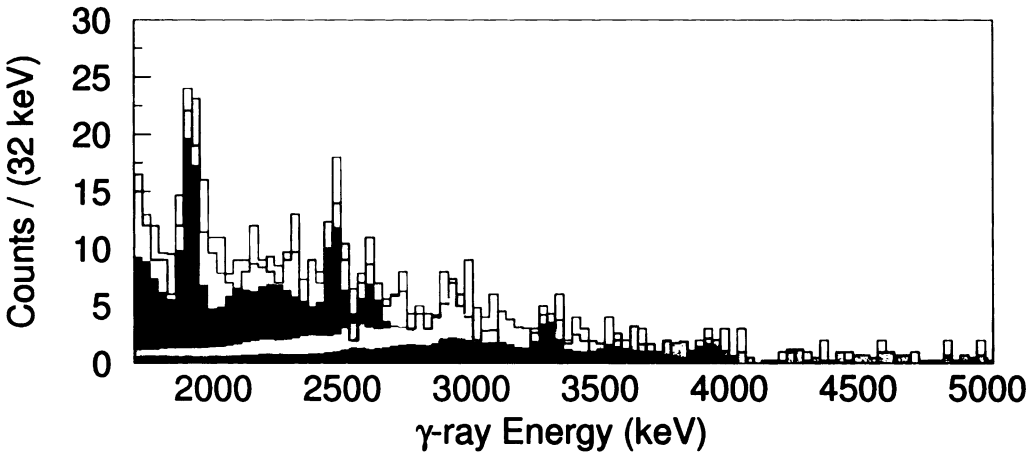

Figure 3.7: Spectrum of γ-rays in coincidence with ^{36}Si(p,p') shown from 1700-5000 keV. Response functions for fitted γ-ray transitions (colors) are stacked with the scaled background (grey) at the top. Data is shown as an unfilled histogram (black line).

Again, the unfilled solid histogram is the measured spectrum, while a filled solid line histogram is the fitted spectrum. Fitted responses are stacked, filled histograms of various colors. At the base of the stack, in black, is the contribution of all responses coming from γ rays with energies above 2000 keV. The window background is at the top of the stack in grey.

In this second fit, a doublet is shown between 1400 and 1450 keV. Hints of this doublet stucture were observed in this experiment — larger than expected peak width, a shoulder visible in one ring spectrum — but no firm conclusions could be drawn. Even if a doublet was found, fitting the positions and intensities would be impossible with the resolution of this Doppler-corrected spectrum. Fortunately, this doublet was observed in a deep inelastic collision experiment [85] published during this analysis. That experiment observed transitions at 1408(1), 1442(3), and 842(1) keV, which they identify as the $2_1^+ \rightarrow 0_1^+$, $4_1^+ \rightarrow 2_1^+$, and $6_1^+ \rightarrow 4_1^+$ transitions respectively. An energy spacing of 34 keV was used to fix the relative positions of the doublet members, and the positions and intensities of the doublet were sucessfully fit.

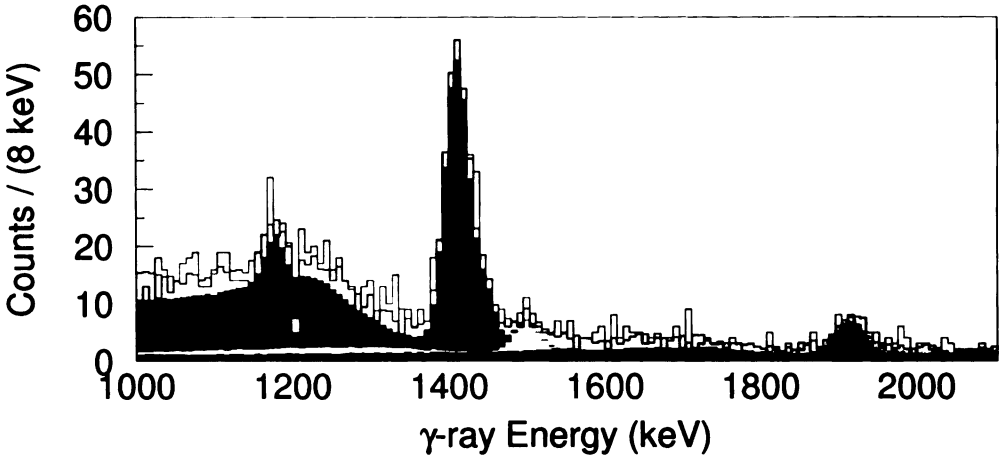

Figure 3.8: Spectrum of γ-rays in coincidence with ^{36}Si(p,p') shown from 1000-2100 keV. Response functions for fitted γ-ray transitions (colors) are stacked with the scaled background (grey) at the top. The sum of all responses due to higher energy γ rays is shown as a black filled histogram at the base of the stack. Data is shown as an unfilled histogram (black line).

Table 3.2: Energies and cross sections for γ rays produced in $p(^{36}\mathrm{Si},^{36}\mathrm{Si}+\gamma)\mathrm{p}'$.

γ-ray energy (keV)	unc.	Cross section (mb)	unc.
1179	3	2.1	0.6
1412.0	1.6	18.0	1.0
1446.0	1.6	3.8	0.8
1501	5	2.1	0.4
1916	4	3.4	0.4
2472	5	2.3	0.4
2613	15	1.1	0.4
2928	16	1.5	0.5
3299	18	1.2	0.3
3925	17	1.0	0.2

Cross sections to produce each γ ray were calculated using Eq. 3.1, and energy uncertainties were calculated by adding the position uncertainty from the fit to the calibration uncertainty in quadrature. Results are shown in table 3.2. For the 1412 and 1446 keV peaks, two additional uncertainties were also added in quadrature: uncertainty due to lifetime of the 2_1^+ state (0.5 keV) and uncertainty in the doublet energy spacing (0.7 keV).

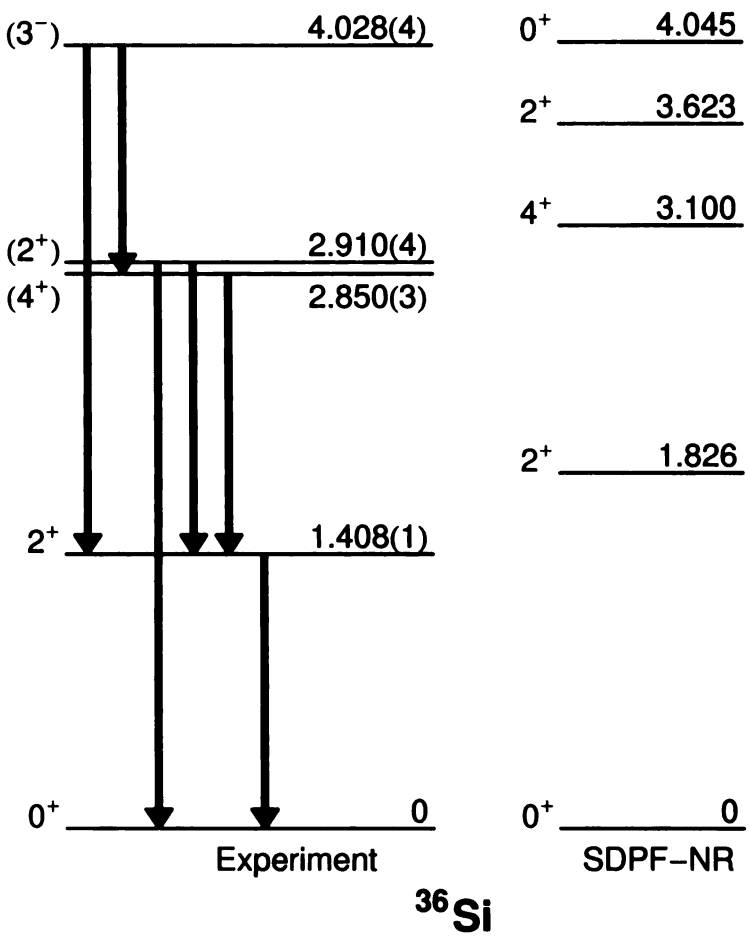

Figure 3.9: Level scheme of ^{36}Si deduced in this experiment is compared with low-lying levels calculated in the shell model. Energies are given in MeV.

These γ rays were then used to build a level scheme based on the energy sums and the known $4_1^+ \rightarrow 2_1^+ \rightarrow 0_1^+$ cascade. Because the doublet was well separated in the deep inelastic experiment, those energies will be used for the 2_1^+ and 4_1^+ levels. The following energy sums were found.

$$1408(1) + 1502(5) = 2909(5) \cong 2928(16)$$

$$1442(3) + 1179(3) = 2621(4) \cong 2613(15)$$

The resulting level scheme is shown in figure 3.9. All level schemes in this thesis were drawn using the `LevelScheme` package [86].

Table 3.3: Energies and cross sections for states populated in $p(^{36}\mathrm{Si},^{36}\mathrm{Si}+\gamma)\mathrm{p}'$.

Level energy (keV)	unc.	Cross section (mb)	unc.
1408	1	7.4	2.4
2850	3	1.8	1.0
2910	4	4.0	0.7
4028	4	3.6	0.7

Feeding corrections were made according to this level scheme. Unplaced γ rays could decay to these levels causing further reductions to the population cross sections. Decays to the ground state and first excited state are the most likely, and decays to higher-lying states will not affect the population cross section of the 2_1^+ state. Thus, the effect of the unplaced γ rays will be considered only for the 2_1^+ state. Feeding from unplaced γ rays is estimated as 50(25)% of the summed cross section of all unplaced transitions. Corrections as discussed in section 2.4 were applied. Table 3.3 gives the level energies, population cross-sections, and associated uncertainties.

Tentative J^π assignments are given in figure 3.9. The first two spin-parity assignments are taken from the previously mentioned Coulomb excitation and deep inelastic experiments [84,85]. The tentative 3^- assignment is based on the decay to both 4^+ and 2^+ states and the observation that (p,p') typically populates 2^+ and 3^- states in even-even nuclei. The tentative 2^+ assignment of the 2910 keV level is based on the decay to both 2^+ and 0^+ states and the typical population of 2^+ and 3^- states in even-even nuclei by inelastic proton scattering.

3.2.2 ^{38}Si

Published spectroscopy of ^{38}Si prior to this experiment was confined to the Coulomb excitation measurement of Ibbotson *et al.* [84]. The reported 2_1^+ energy was 1084(20) keV. Figures 3.10 and 3.11 show the full γ-ray spectrum for the reaction $p(^{38}\mathrm{Si},^{38}\mathrm{Si}+\gamma)\mathrm{p}'$ and the region from 800 to 1400 keV in detail. The $2_1^+ \rightarrow 0_1^+$ transition is dominant with two smaller peaks near 1160 and 1300 keV. Around 2000 keV, the spectrum is

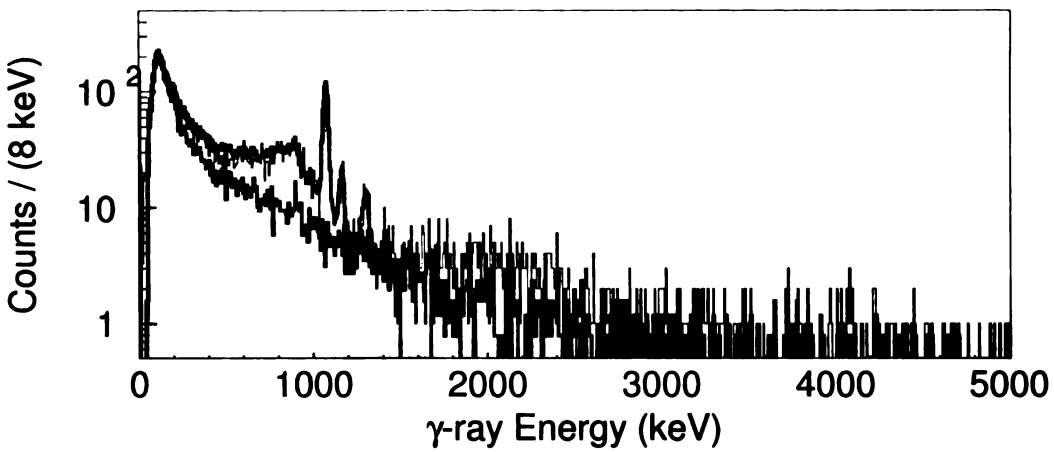

Figure 3.10: Full γ-ray spectrum of ^{38}Si. The background (grey-filled) and fit (blue) are superimposed on the full spectrum (black).

clearly above background, but no peak is visible.

As before, the fitting proceeded from high to low energy. In this case, the statistics were too poor for a definative peak fit. Indeed, it is unclear how many peaks may be contributing. The spectrum returns to the level of background near 2500 keV. The intensity of a hypothetical 2400 keV peak was fit to provide some measure of the intensity which may feed other peaks. This single peak fit gave a good match to the data, but shifts in the starting position or two-peak fits would give similar results. The Compton continuum from such a low-intensity, high-energy peak is negligible in the region of the other peaks.

The region from 800 to 1400 keV was fit using three response functions and the window background. Figure 3.11 shows the resulting fit. Again, the unfilled, solid line histogram is the measured data; the grey-filled, solid line histogram is the sum of all responses and background. The γ-ray response functions are stacked, in various colors, with the window background at the top of the stack in grey. Table 3.4 gives the cross sections for production of each γ ray.

Unlike the above ^{36}Si inelastic analysis, there were neither energy sums nor re-

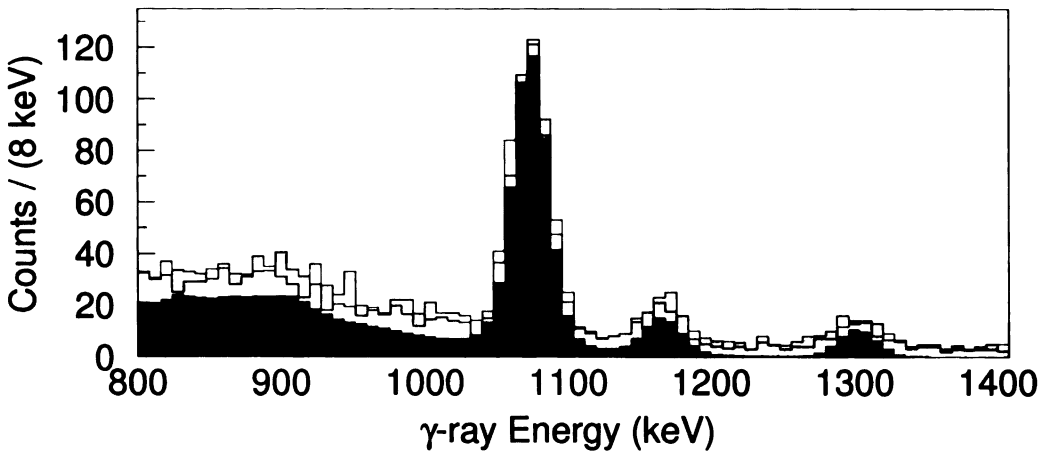

Figure 3.11: Spectrum of γ-rays in coincidence with ^{38}Si(p,p') shown from 800-1400 keV. Response functions for fitted γ-ray transitions (colors) are stacked with the scaled background (grey) at the top. Data is shown as an unfilled histogram (black line).

cently published level schemes to enable feeding correction. Systematics of even-even nuclei would reject either the 1167 or 1303 keV γ rays as decays to the ground state. Whether these transitions should be parallel or form a cascade was unclear. However, data from other reaction channels leading to excited states in ^{38}Si is present in this data set. As explained in section 2.3.3, the large momentum acceptance of the S800 spectrograph allowed data on reaction residues from neutron removal reactions to be collected simultaneously with the inelastic reaction. So, the γ-ray spectrum recorded in coincidence with $p(^{39}\text{Si},^{38}\text{Si}+\gamma)\text{X}$ was examined.

Figure 3.13 shows the γ-ray spectrum from 800 to 1400 keV for neutron removal reactions populating bound states of ^{38}Si. There are no definitive peak structures

Table 3.4: Energies and cross sections for γ rays produced in $p(^{38}\text{Si},^{38}\text{Si}+\gamma)\text{p}'$.

γ-ray energy (keV)	unc.	Cross section (mb)	unc.
1077	2	18.5	0.5
1167	3	2.5	0.3
1303	3	2.1	0.3
(2400)	-	2.7	0.6

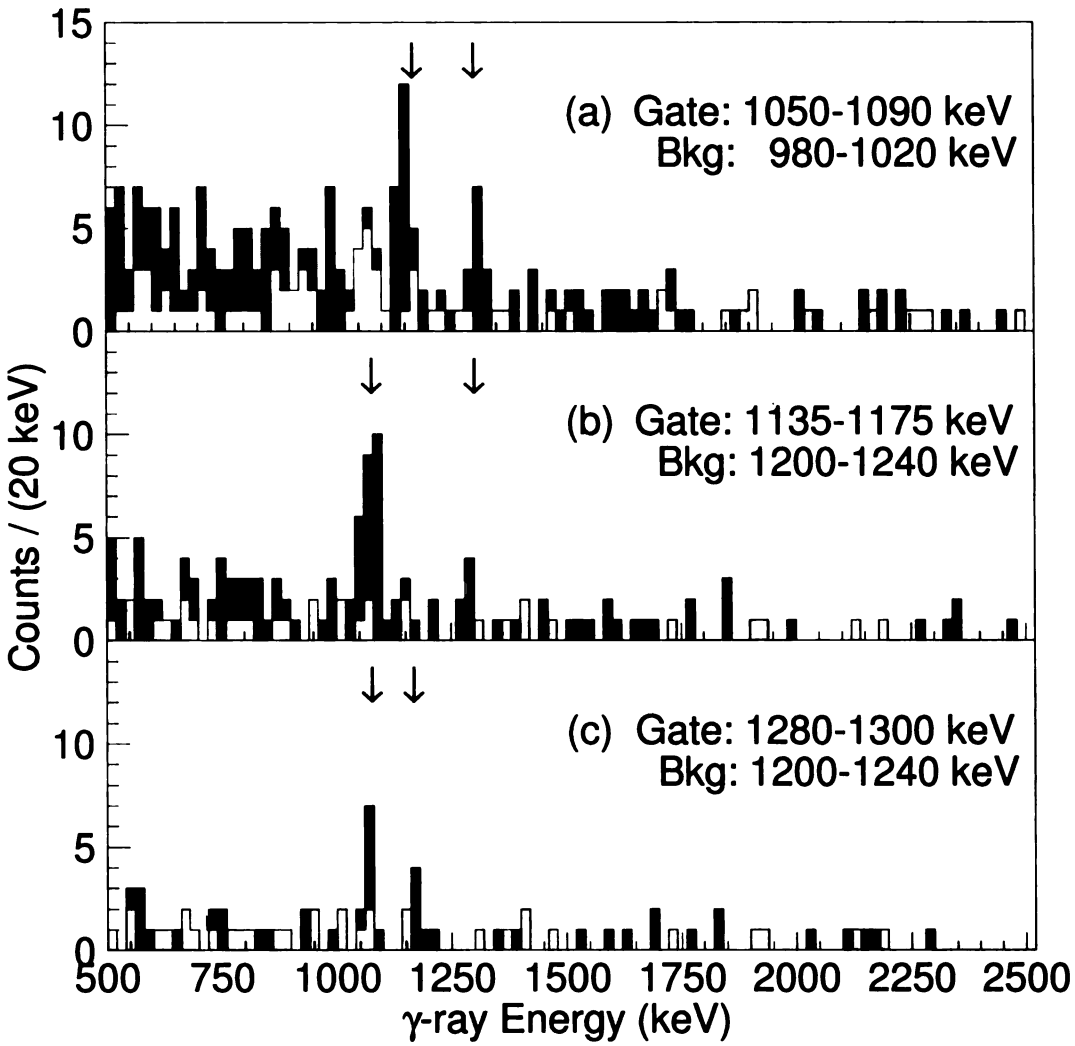

Figure 3.12: ^{38}Si $\gamma - \gamma$ spectra taken from a sum of several reaction channels. In each panel, the energy gates listed were used to create the coincident (black) and background (grey) spectra. Transitions in coincidence with the each gate are labeled by arrows.

other than the three visible in this figure. However, the relative intensities of the 1167 and 1303 keV transitions precluded the cascade 1167 $\rightarrow$ 1303 $\rightarrow$ 1070. Also, the strong population of the 1167 $\rightarrow$ 1070 cascade allowed the first observation of $\gamma - \gamma$ coincidences in this nucleus. The statistics were meagre. To check for other coincidence relations, all reaction channels populating bound excited states in ^{38}Si were added to form a single $\gamma - \gamma$ matrix. Figure 3.12 shows γ-ray spectra resulting from gates on

the three full-energy peaks. A backgound spectrum gated on a nearby energy region is superimposed as a grey histogram in each case. From this, the following $\gamma - \gamma$ coincidences were obtained:

$$1077 - 1167$$

$$1077 - 1303$$

$$1167 - 1303$$

Thus, the cascade $1303 \rightarrow 1167 \rightarrow 1070$ is affirmed, and two new levels have been observed in ^{38}Si.

Before quoting final level energies, the neutron removal spectrum was fit with three γ-ray responses and a linear background. The goal was to verify the peak eneries, and possibly improve the energy determination for the two new transitions. Detailed fitting of the $p(^{39}\mathrm{Si},^{38}\mathrm{Si} + \gamma)\mathrm{X}$ spectrum showed that although the peaks closely resemble those of the inelastic spectrum, significant shifts in peak position have occurred. Although the total uncertainty in peak energy is at the 2 keV level, the uncertainties due to level lifetime, Doppler correction parameters, and energy calibration are common for peaks in these two spectra. Thus, only the fitting uncertainty is used when comparing them. The 1077 keV peak is shifted by -3.0(6) keV in the neutron removal spectrum, and the 1167 keV peak is shifted by -10.5(22) keV. These are 5σ shifts, which must be explained. Large error bars on the 1303 keV peak preclude a definitive statement on the peak shift.

Though the addition of a peak would solve one of these shifts, it is unlikely that both peaks would have doublets and that they would both be at lower energies than the peaks observed in the inelastic spectrum. An error in the Doppler correction is also unlikely. Such an error would cause a common fractional displacement in the energies, i.e. the observed shifts would be directly proportional to the observed peak energy. After normalizing the peak shifts listed above by their respective peak positions, the fractional shifts are different by $> 3\sigma$. The remaining cause of peak shifts is the effect of lifetime.

For a lifetime to cause a γ-ray peak to shift between two Doppler corrected spectra of nearly the same projectile velocity, the state emitting the shifted γ-ray must be fed by one or more higher-lying states having non-negligible lifetime(s). Taking relative intensities and peak shifts into account, feeding of the level at 2244 keV gives the simplest explaination of the shifts of both peaks.

The $p(^{39}\mathrm{Si},^{38}\mathrm{Si}+\gamma)\mathrm{X}$ spectrum was fit under the assumption that the level at 2244 keV was fed by state(s) with lifetime(s) such that the resulting 1077 and 1167 keV peaks were shifted in the Doppler-corrected spectrum. Direct population of the 2244 keV level and population through fast decays was also included. The 1077 and 1167 keV response shifts were fixed at the values given by the inelastic fit; the 1303 keV response was free to shift. A new response formed by summing the 1077 and 1167 keV responses was free to shift; this represents the cascade decay of the 2244 keV level when fed by a delayed γ-ray transition. All response scaling was free to vary in the fit. Figure 3.13 shows the spectrum, fit, and responses as before. The color-coding of peaks is common between Figs. 3.11 and 3.13. The additional delayed cascade decay of the 2244 keV level is shown in cyan as a two-peak response. Uncertainties in the γ-ray energies from the inelastic fit were accounted for by repeating the fit with using the $\pm 1\sigma$ limits for each fixed peak.

The resulting energy shift of -14(2) keV for the 1167 keV shifted component translates to a feeder lifetime of 63(10) ps. Though this shifted component has a large fraction of the excited state population, no feeding γ ray was observed in the $\gamma-\gamma$ coincidences, nor was any transition other than the three previously mentioned observed in the singles spectrum. There is, in fact, no reason to conclude that the feeding of the 2244 keV level proceeds through a single transition. Because the energy shifting of peaks is nearly linear with lifetime, this feeder lifetime may be thought of as the average of a collection of feeding γ-ray transitions. Furthermore, $\gamma-\gamma$ coincidences resulting from Compton scattering off one SeGA detector into another is highly probable. Thus, the region $\lesssim$ 1000 keV has a physical background that makes it difficult

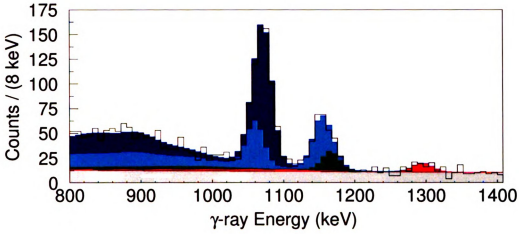

Figure 3.13: Spectrum of γ-rays in coincidence with ^{39}Si$(p, X)^{38}$Si shown from 800-1400 keV. Energy axis and colors correspond to figure 3.11. An added response (cyan) corresponds to a delayed γ cascade from the 2244 keV level.

Table 3.5: Energies and cross sections for states populated in $p(^{38}\text{Si},^{38}\text{Si}+\gamma)\text{p}'$.

Level energy (keV)	unc.	Cross section (mb)	unc.
1077	2	15.4	2.6
2244	4	0.4	0.4
3545	6	2.3	0.4
Unplaced estimate	-	2.7	0.6

to locate new coincidences.

Though the source of the delayed feeding is unknown, it is clear that these are the same peaks observed in the inelastic spectrum. The prompt 1167 keV transition comes with more intensity than the 1296(4) keV transition, which is associated with the 1303(2) keV transition found in the inelastic spectrum. (A weighted average yields a transition energy of 1301(5) keV.) So, the cascade ordering made above remains intact.

The deduced level scheme and feeding-corrected $p(^{38}\text{Si},^{38}\text{Si}+\gamma)\text{p}'$ excitation cross sections are given in figure 3.14 and table 3.5, respectively. Coulomb excitation established the 2_1^+ assignment for the 1077 keV level. Strong population of the level at 3545 keV suggests a 3^- assignment. The excitation cross section of the 2244 keV level

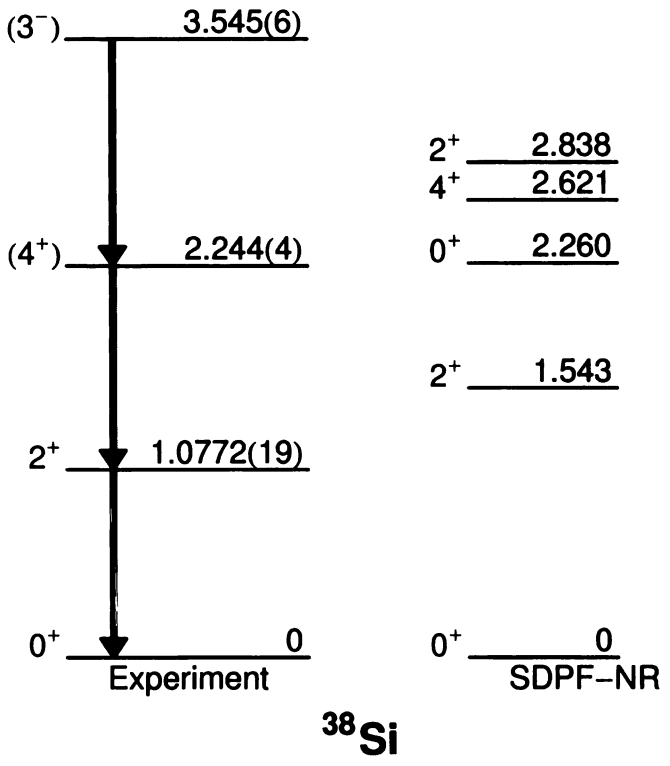

Figure 3.14: Level scheme of ^{38}Si deduced in this experiment is compared with low-lying levels calculated in the shell model. Energies are given in MeV.

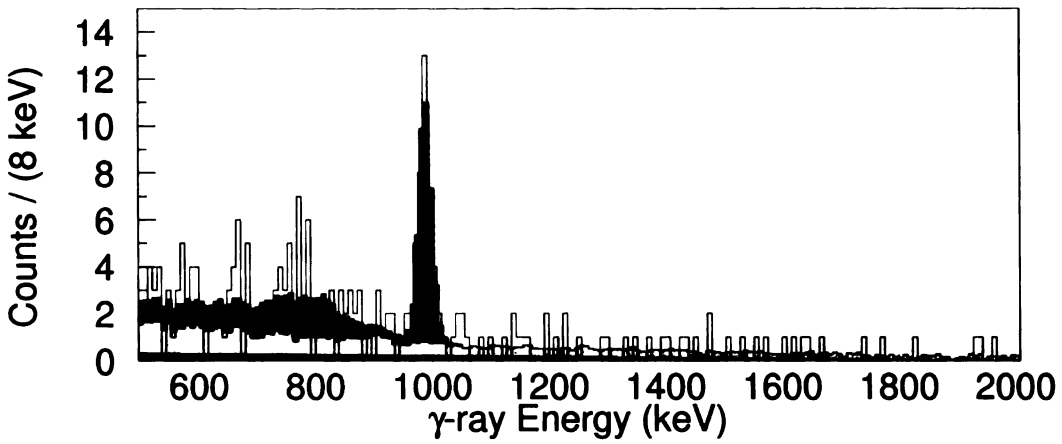

Figure 3.15: Spectrum of γ-rays in coincidence with ^{40}Si(p,p') shown from 500-2000 keV. The $2_1^+ \rightarrow 0_1^+$ transition's response function (blue) is stacked on the scaled background (grey) and a small linear background term (green). Data is shown as an unfilled histogram (black line).

is consistent with no direct population. Feeding from a tentative 3− and decays to the established 2_1^+ suggest either 2^+ or 4^+ for the 2244 keV level. Strong population in the neutron removal channel favors a 4^+ assignment, see section 2.1.4.

3.2.3 ^{40}Si

This experiment was the first to observe γ-ray transitions in ^{40}Si. Figure 3.15 shows the γ-ray spectrum for the reaction $p(^{40}\mathrm{Si},^{40}\mathrm{Si}+\gamma)\mathrm{p}'$ from 500 to 2000 keV. A single peak at 986 keV dominates the spectrum. Superimposed on this spectrum are the fitted peak response, the window background, and a small linear background function added to improve the fit. These components are stacked in order linear background, window background, and peak response, from bottom-to-top in figure 3.15.

Since the γ ray at 990(5) keV is the only transition observed in $p(^{40}\mathrm{Si},^{40}\mathrm{Si}+\gamma)\mathrm{p}'$, it was placed as the $2_1^+ \rightarrow 0_1^+$ transition. As this is the only peak observed in the spectrum, no feeding correction was applied, but an asymmetric uncertainty of -20% was added in quadrature to the population cross-section uncertainty of the first

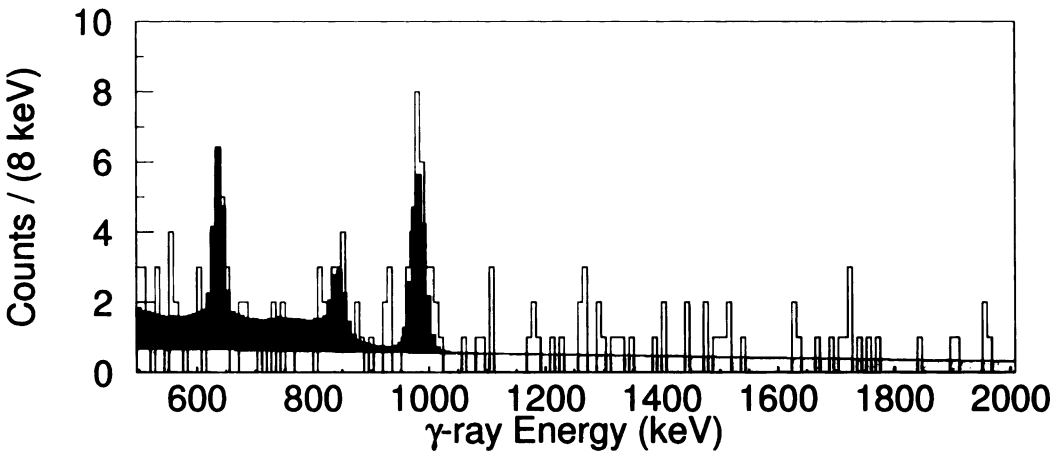

Figure 3.16: Spectrum of γ-rays in coincidence with $p(^{42}\mathrm{P},^{40}\mathrm{Si}+\gamma)\mathrm{X}$ shown from 500-2000 keV. Response functions for fitted γ-ray transitions (colors) are stacked on a linear background (grey). Data is shown as an unfilled histogram (black line).

Table 3.6: Energies and observed cross sections for γ rays produced in $p(^{42}\mathrm{P},^{40}\mathrm{Si}+\gamma)\mathrm{X}$. Total observed reaction cross section is also shown.

γ-ray energy (keV)	unc.	Cross section (mb)	unc.
638	5	1.1	0.2
845	6	0.7	0.2
982	5	2.0	0.3
Total cross-section		3.7	1.0

excited state. Twenty percent is the final feeding estimate used in ^{38}Si and is roughly the size of a single transition which might be missed in this low-statistics spectrum. This gives an inelastic excitation cross section, $\sigma_{0_1^+\rightarrow 2_1^+}$, of 20^{+2}_{-4} mb.

In addition to inelastic scattering, excited states in ^{40}Si were observed in the reaction $p(^{42}\mathrm{P},^{40}\mathrm{Si}+\gamma)\mathrm{X}$. Figure 3.16 shows the γ-ray spectrum recorded in coincidence with this reaction. Table 3.6 gives the observed cross sections for producing each γ-ray transition. The total observed cross section was calculated using the total number of downscaled particles observed in this PID-reaction channel gate; this value is also presented in table 3.6. Combining the both reaction channels gives the $2_1^+ \rightarrow 0_1^+$ transition an energy of 986(5) keV, where an uncertainty of 3 keV has been

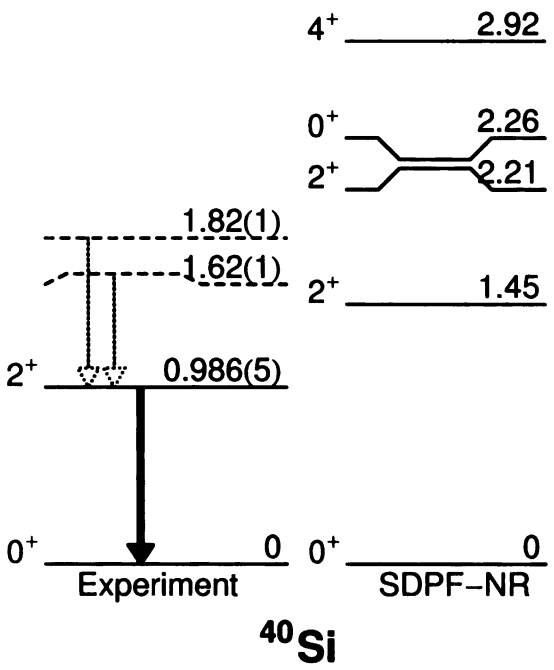

Figure 3.17: Level scheme of ^{40}Si deduced in this experiment is compared with low-lying levels calculated in the shell model. Energies are given in MeV.

added to account for the unknown lifetime of the 2_1^+ state. Transitions at 991(10) and 624(10) keV have also been observed in the secondary fragmentation work of Grevy *et al.* [87].

Though $\gamma - \gamma$ coincidences and energy sums are impossible in this case, the placement of at least one of the two new transitions as directly feeding the 2_1^+ level is quite probable. In the cases of ^{36,38}Si and ^{40}S, the strongest observed γ-ray is from the $2_1^+ \rightarrow 0_1^+$ transition, and the second strongest transition directly feeds the 2_1^+ level in each case. This suggests at least one of the two new transitions directly feeds the 2_1^+ level, and a second excited state of ^{40}Si lies at either 1624(7) or 1838(8) keV. Figure 3.17 shows the deduced level scheme and the shell model prediction.

3.2.4 ^{40}S

Prior to this experiment, the spectroscopy of ^{40}S had been studied by Coulomb excitation, β-delayed γ emission, and projectile fragmentation [88–90]. Figures 3.18,

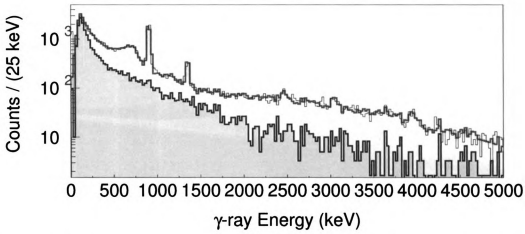

Figure 3.18: Full γ-ray spectrum of ^{40}S. The background (grey-filled) and fit (blue) are superimposed on the full spectrum (black).

3.19, and 3.20 show full, high-energy, and low-energy portions of the γ-ray spectrum collected in prompt coincidence with $p(^{40}\mathrm{S},^{40}\mathrm{S}+\gamma)\mathrm{p}'$. The $2_1^+ \rightarrow 0_1^+$ transition at 906 keV clearly dominates the spectrum, but a strong peak near 1350 keV and smaller peaks above 2 MeV indicate significant feeding. As before, solid-line, white-filled histograms represent the data and fit components are stacked, color-filled histograms superimposed on the data.

Fitting was performed first on the energy range 1400 to 5000 keV, as shown in figure 3.19. A significant background in addition to the window background was observed. A linear background was added and nicely accounted for these excess counts. The linear background is shown as a black histogram on which the peak responses are stacked in figure 3.19. After fitting the high-energy region, a fit to the region 500 to 1500 keV was performed. Additional fitting indicates $\sim$ 1.4 mb may lie in other peaks in this region. Figure 3.20 shows the fit with the linear background and the fixed contributions from all higher-energy peaks shown as a narrow black-filled histogram. Table 3.7 gives the γ-ray production cross sections for each of the fitted peaks.

The 905.9(11) keV transition is associated with the $2_1^+ \rightarrow 0_1^+$ transition in ^{40}S

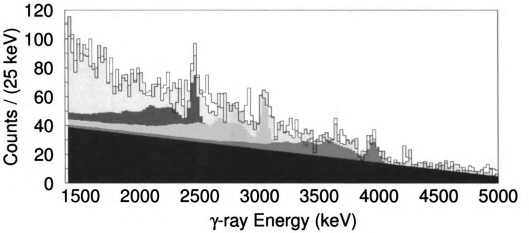

Figure 3.19: Spectrum of γ-rays in coincidence with $^{40}\mathrm{S}(p,p')$ shown from 1400-5000 keV. Response functions for fitted γ-ray transitions (colors) are stacked with the scaled background (grey) at the top. Data is shown as an unfilled histogram (black line).

Table 3.7: Energies and cross sections for γ rays produced in $p(^{40}\mathrm{S},^{40}\mathrm{S}+\gamma)\mathrm{p}'$.

γ-ray energy (keV)	unc.	Cross section (mb)	unc.
905.9	1.1	27.7	0.3
1351.4	1.4	5.5	0.2
2457	5	1.7	0.2
3044	6	2.0	0.2
3957	9	1.6	0.1

which has been previously observed in β-decay at an energy of 903.69(7) keV [89]. Similarly, the transition at 1351.4(14) keV is associated with the previously observed 1351.10(12) keV transition from β-decay. This transition is known to decay to the 2_1^+ level.

A single energy sum was found:

$$3044(1) + 905.9(11) = 3952(5) \cong 3957(9)$$

Taking a weighted average, the resulting level energy is 3952(5) keV. A level at 3947.0(3) keV was observed in β-decay, but that level decayed by the emission of

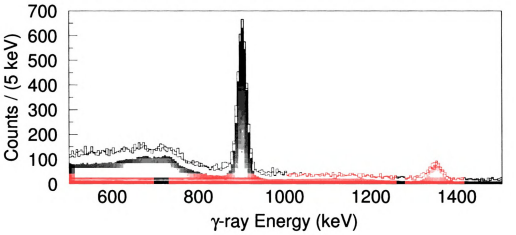

Figure 3.20: Spectrum of γ-rays in coincidence with $^{40}S(p,p')$ shown from 500-1500 keV. Response functions for fitted γ-ray transitions (colors) are stacked with the scaled background (grey) at the top. The sum of all responses due to higher energy γ rays is shown as a black filled histogram at the base of the stack. Data is shown as an unfilled histogram (black line).

1692.6(9) and 3043.2(4) keV γ-rays with relative intensities of 1.1(4) and 4.4(5), respectively. No 1693 keV transition was observed, so fitting was tried with a 1693 response function whose intensity relative to the 3044 response function was allowed to vary in $\pm 1\sigma$ and $\pm 2\sigma$ ranges. Both fits converged with the relative intensity parameter at the lower limit and significantly increased the χ^2 of the fit. Furthermore, the β-decay experiment did not observed a transition near 3947 keV. Therefore, the level seen here and the 3947 keV level observed in β-decay are not the same.

The 2457(5) keV transition observed here was similarly checked for correspondence with the 2469.8(2) keV transition observed in β-decay [89]. If these transitions were the same, a 2808-1013 keV cascade would be expected with an intensity relative to the 2469.8 keV of 86(26)%. Fits at the $\pm 1\sigma$ and $\pm 2\sigma$ range for this relative intensity failed to converge. Allowed to fit freely, the relative intensity of the 2808-1013 keV cascade was 12(21)and consistent with zero intensity. Therefore, the transition seen here and the 2469.8 keV transition observed in β-decay are different.

Although the ^{40}S has the highest statistics of any spectrum in this thesis, $\gamma - \gamma$

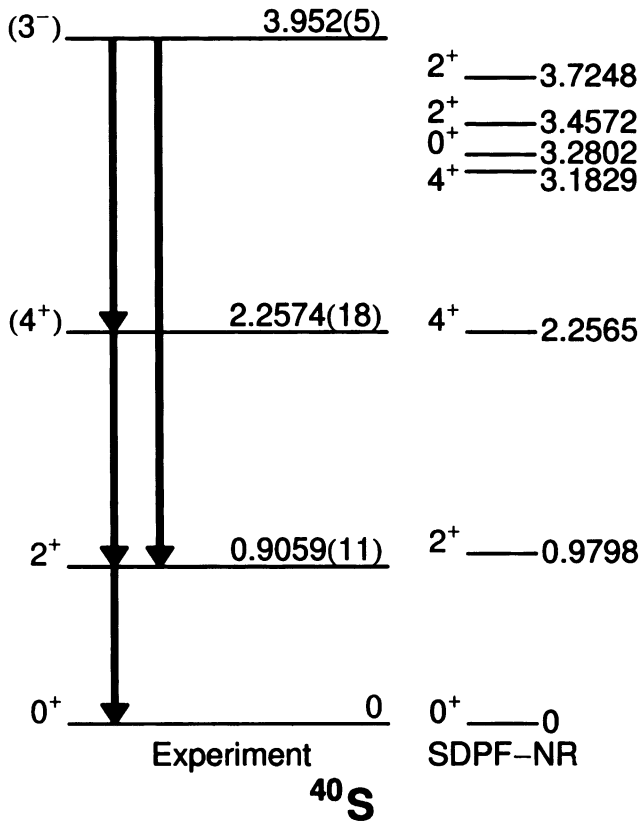

Figure 3.21: Level scheme of ^{40}S deduced in this experiment is compared with low-lying levels calculated in the shell model. Energies are given in MeV.

coincidences were not helpful in placing transitions into a level scheme. Only the 906-1351 keV coincidence was clear and unambiguous. In the remaining cases, the high γ-ray energy causes the intensity to be spread over the full-energy peak, Compton edge, and escape peaks. Only in the lab frame are the Compton edge and escape peaks at fixed energies relative to the full-energy peak. Doppler reconstruction over many angles blurs the distinctions, and in the end, the response function for a γ ray above 2000 keV becomes a full energy peak with a mound of superimposed peaks at lower energy. With three high-energy peaks, each having a similar low-intensity, the γ-ray spectrum in coincidence with the 906 keV peak shows coincidences above 2000 keV, but no clear assignment is possible.

Figure 3.21 shows the level scheme as observed in $p(^{40}\mathrm{S},^{40}\mathrm{S}+\gamma)\mathrm{p}'$ along with the shell model predictions for low-lying even parity states. Feeding of the 2_1^+ level

Table 3.8: Energies and cross sections for states populated in $p(^{40}S,^{40}S+\gamma)p'$.

Level energy (keV)	unc.	Cross section (mb)	unc.
905.9	1.1	19.8	1.2
2257.4	1.8	6.0	0.4
3952	5	3.9	0.3

is taken as the summed intensity of the 1351 and 3044 keV transitions plus 50(25)% of the unplaced, fitted γ-ray intensity. No feeding correction has been made for the 2257 and 3952 keV levels. Table 3.8 gives the observed level energies and excitation cross sections; corrections discussed in section 2.4 have been applied to excitation cross sections.

3.2.5 ^{42}S

Prior to this experiment, the spectroscopy of ^{42}S had been studied by Coulomb excitation, and projectile fragmentation [88,90]. Figure 3.22 shows the γ-ray spectrum collected in prompt coincidence with $p(^{42}S,^{42}S+\gamma)p'$ from 500 to 3000 keV. In addition to the strong $2_1^+ \rightarrow 0_1^+$ transition at 903.1(14) keV, a much weaker peak has been fit at 1838(9) keV. Fit components are colored, stacked with grey-filled window background at the top, and superimposed on the white-filled, solid-line histogram of the data.

The 1838(9) keV transition observed here corresponds to the 1821(8) keV transition observed in projectile fragmentation [90]. As in the previous work, this transition is placed as directly feeding the 2_1^+ level. Table 3.9 gives the feeding corrected exitation cross sections for the two levels observed in $p(^{42}S,^{42}S+\gamma)p'$.

Table 3.9: Energies and cross sections for states populated in $p(^{42}S,^{42}S+\gamma)p'$.

Level energy (keV)	unc.	Cross section (mb)	unc.
903.1	1.4	16.3	1.0
2741	9	1.6	0.4

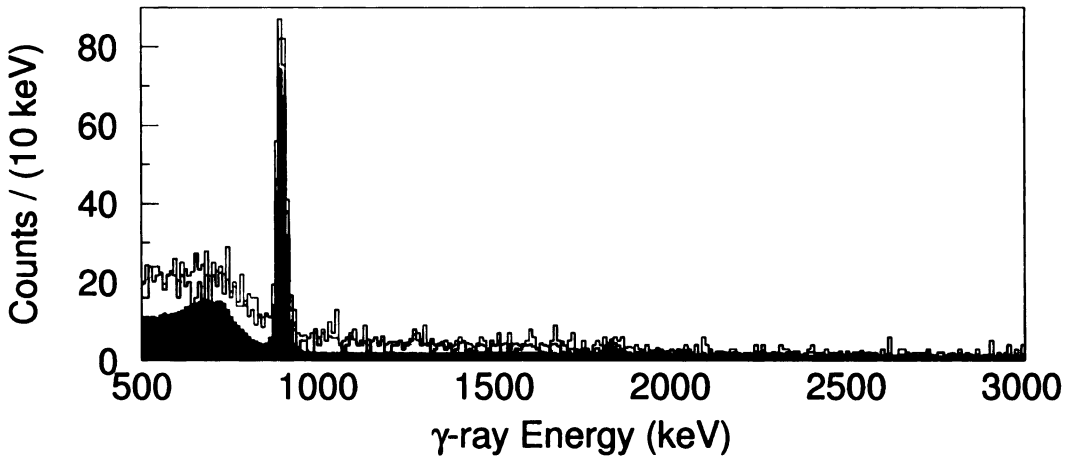

Figure 3.22: Spectrum of γ-rays in coincidence with $^{42}S(p,p')$ shown from 500-3000 keV. Response functions for fitted γ-ray transitions (colors) are stacked with the scaled background (grey) at the top. Data is shown as an unfilled histogram (black line).

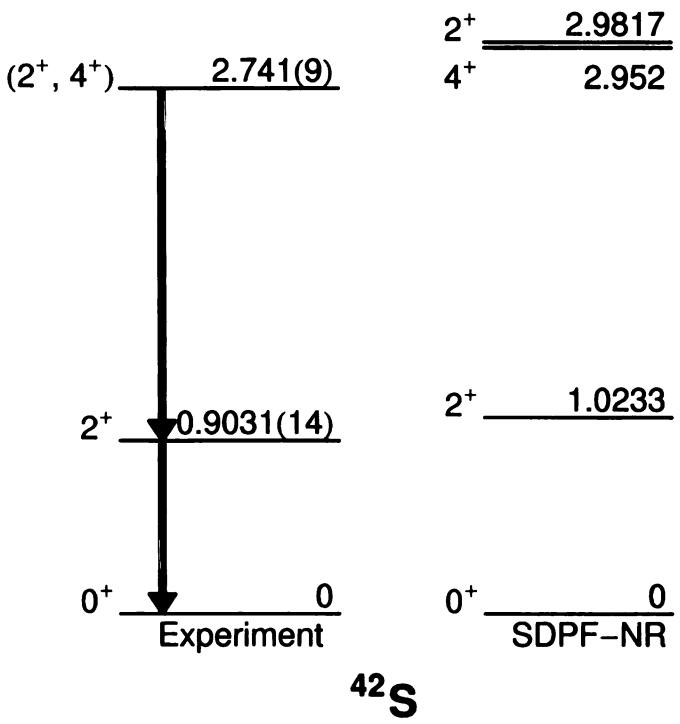

Figure 3.23: Level scheme of ^{42}S deduced in this experiment is compared with low-lying levels calculated in the shell model. Energies are given in MeV.

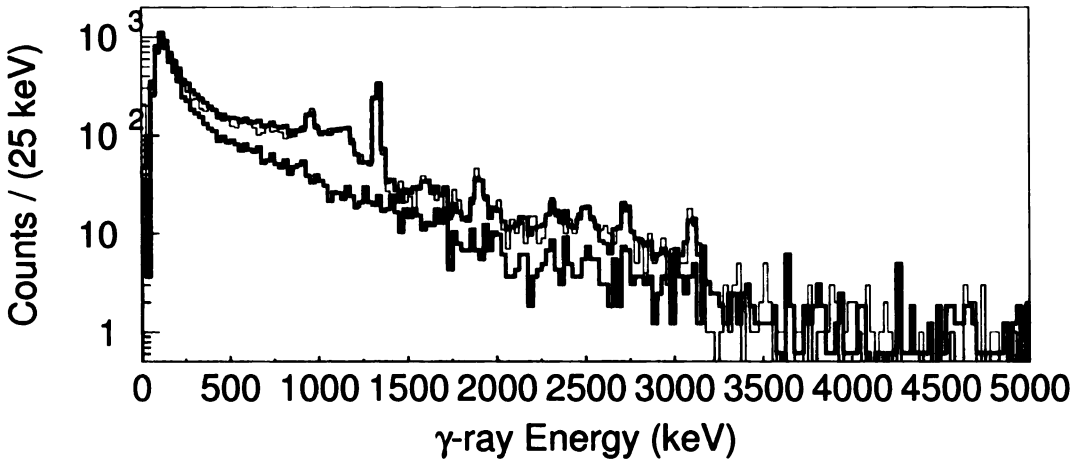

Figure 3.24: Full γ-ray spectrum of ^{44}S. The background (grey-filled) and fit (blue) are superimposed on the full spectrum (black).

3.2.6 ^{44}S

Prior to this experiment, the spectroscopy of ^{44}S had been studied by Coulomb excitation, projectile fragmentation, proton knockout, and isomer decay [34,88,90,91]. Figures 3.24, 3.25, and 3.26 show full, high-energy, and low-energy portions of the γ-ray spectrum collected in prompt coincidence with $p(^{44}\mathrm{S},^{44}\mathrm{S}+\gamma)\mathrm{p}'$. The $2_1^+ \rightarrow 0_1^+$ transition at 1328 keV is the strongest peak. Prominant full-energy peaks at both higher and lower energies open the possibility of significant γ-ray feeding of the 2_1^+ state. Solid-line, white-filled histograms represent the data and fit components are stacked, color-filled histograms superimposed on the data.

Fitting was done in two steps. First, the energy range 1500-5000 keV was fit, see figure 3.25, adding peak responses from high to low energy. Then, the energy range 800-1500 keV was fit, see figure 3.26, holding fixed the scaling and shifts of the high-energy peaks. Table 3.10 gives the γ-ray energies, γ-ray production cross sections, and corresponding uncertainties for all fitted transitions.

Low statistics precluded $\gamma - \gamma$ coincidences, but two energy-sum correspondences

were observed.

$$1154(9) + 1331.0(14) = 2485(9) \cong 2491(13)$$

$$1331.0(14) + 954.8(15) + 2719(9) = 5004(9)$$

$$1900(3) + 3100(4) = 5000(5)$$

$$5004(9) \cong 5000(5)$$

Level energies were then calculated as weighted averages of these sums. Ordering of the 955-2719 cascade was determined from γ-ray intensities. The 1900 keV transition is marginally more intense than the 3100 keV transition, but finding a state at such low excitation energy relative to the 2_1^+ state which decays primarily to the ground state is unlikely. Thus, a level is proposed at 3100 keV. Figure 3.27 shows the deduced level scheme and the low-lying, positive parity states calculated in the shell model.

Tentative J^π assignments for ^{44}S were assigned by comparing with the shell-model calculated decay scheme and the expected population of collective 2^+ and 3^- states. Feeding corrections were applied according to this decay scheme. An additional cor-

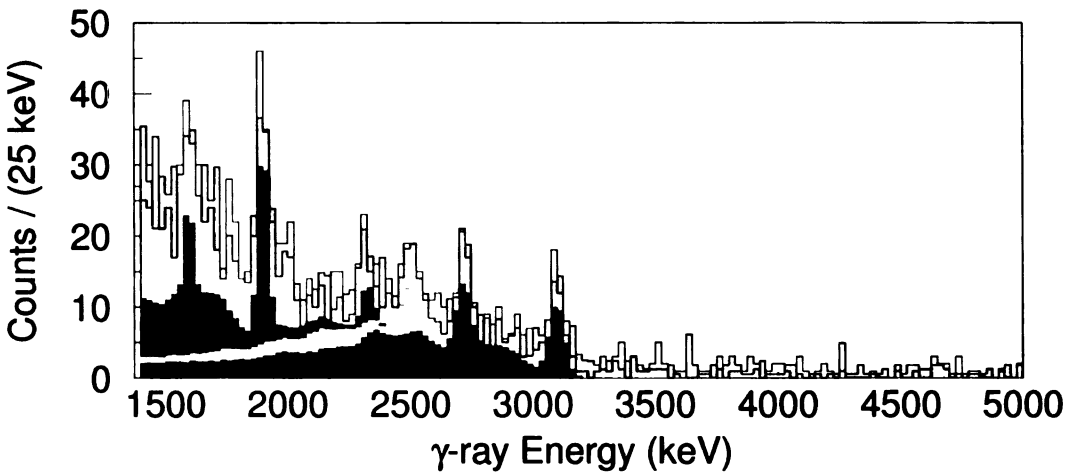

Figure 3.25: Spectrum of γ-rays in coincidence with ^{44}S(p,p') shown from 1500-5000 keV. Response functions for fitted γ-ray transitions (colors) are stacked with the scaled background (grey) at the top. Data is shown as an unfilled histogram (black line).

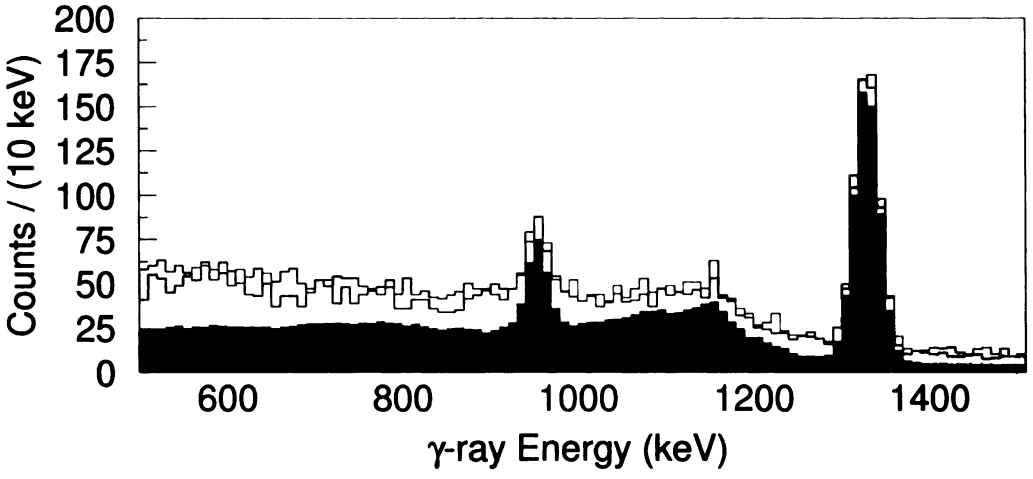

Figure 3.26: Spectrum of γ-rays in coincidence with $^{44}S(p,p')$ shown from 800-1500 keV. Response functions for fitted γ-ray transitions (colors) are stacked with the scaled background (grey) at the top. The sum of all responses due to higher energy γ rays is shown as a black filled histogram at the base of the stack. Data is shown as an unfilled histogram (black line).

Table 3.10: Energies and cross sections for γ rays produced in $p(^{44}S,^{44}S+\gamma)p'$.

γ-ray energy (keV)	unc.	Cross section (mb)	unc.
954.8	1.5	3.7	0.3
1154	9	0.6	0.3
1331.0	1.4	17.0	0.4
1599	7	0.9	0.2
1900	3	2.2	0.2
2328	14	0.5	0.2
2491	13	1.0	0.3
2719	9	1.2	0.3
3100	4	1.9	0.2

rection of 50(25)% of the summed intensity of all unplaced transitions was subtracted from the 2_1^+ cross section. Level energies and excitation cross sections for the reaction $p(^{44}S,^{44}S+\gamma)p'$ are presented in table 3.11.

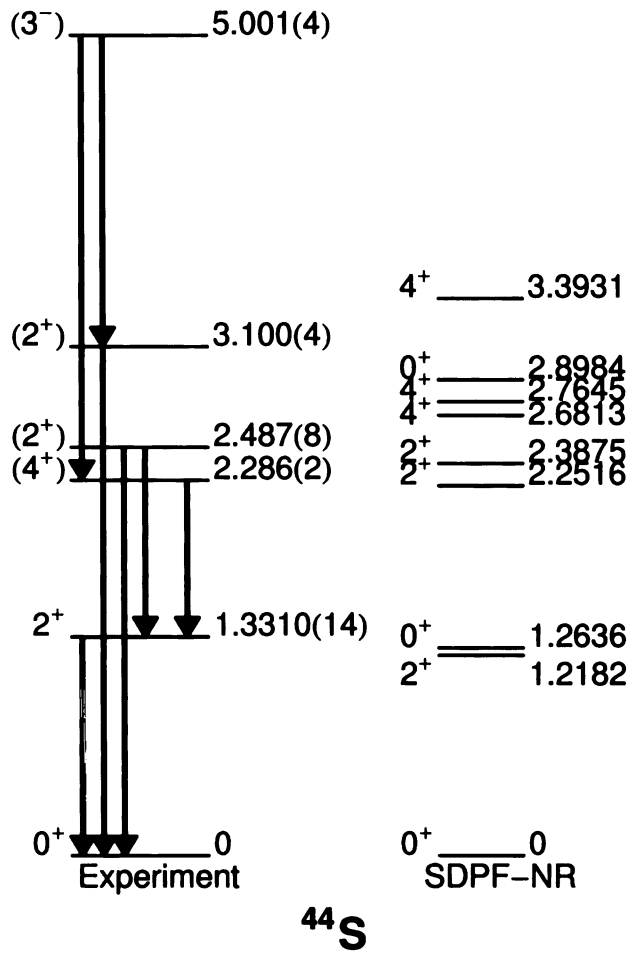

Figure 3.27: Level scheme of ^{44}S deduced in this experiment is compared with low-lying levels calculated in the shell model. Energies are given in MeV.

Table 3.11: Energies and cross sections for states populated in $p(^{44}\mathrm{S},^{44}\mathrm{S}+\gamma)\mathrm{p}'$.

Level energy (keV)	unc.	Cross section (mb)	unc.
1331.0	1.4	12.5	0.9
2286	2	2.7	0.4
2487	8	1.7	0.4
3100	4	-0.3	0.3
5001	4	3.6	0.4

Chapter 4

Results and Discussion

4.1 Spectroscopy of ^{40}Si

As discussed in section 1.3, the $N = 28$ shell gap has been predicted to weaken at or below $Z = 16$. Observation of enhanced collectivity in the neutron-rich sulfur isotopes was viewed as evidence of this weakening. However, an alternate explanation was proposed: the rise in collectivity near ^{44}S may be due to the narrowing of the $1s_{1/2} - 0d_{3/2}$ proton subshell gap. So, three components may play a role in increasing collectivity near ^{44}S:

- Neutrons promoted across the $N = 28$ shell gap
- Protons recoupled in the degenerate $1s_{1/2}0d_{3/2}$ space
- Enhanced proton-neutron coupling.

The strong $Z = 14$ subshell gap, however, remains large from $N = 20 - 28$. Thus, the neutron-rich silicon chain is expected to give a clearer picture of changes in the $N = 28$ shell. Specifically, changes in the 2_1^+ excitation energy of the $N = 20 - 28$ even-even silicon isotopes are tied directly to filling the $0f_{7/2}$ neutron orbital. Filling a single orbital bracketed by shell gaps, one expects a parabolic trend with the highest 2_1^+ energies at the shell gaps and the lowest energy at midshell.

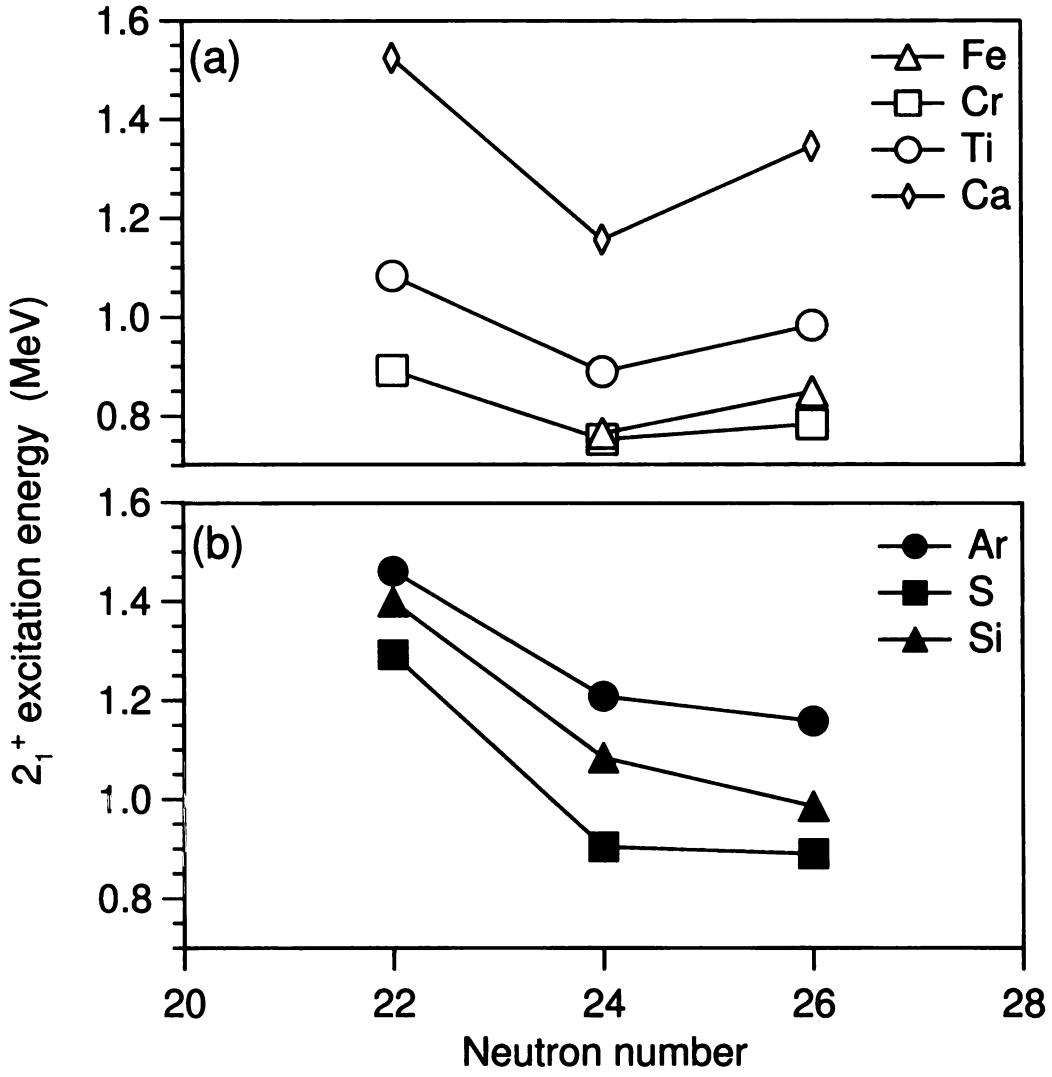

Figure 4.1: Evolution of 2_1^+ energy with neutron number (N) for even-even nuclei with $Z \geq 20$ (a) and $Z < 20$ (b). Data are not shown for $N = 20, 28$ nuclei because several values would be off scale. While a clear parabolic trend is observed in panel (a), $Z < 20$ nuclei show successively smaller increases between $N = 24$ and $N = 26$. The first significant decrease in excitation energy at $N = 26$ occurs in ^{40}Si.

Figure 4.1 shows the 2_1^+ energies versus neutron number for $N = 22, 24, 26$ nuclei for $Z \geq 20$ (panel a) and $Z < 20$ (panel b). Data in this figure were taken from the ENSDF database [92] and the current experiment. Isotopic chains for the higher-Z elements are well-described by a parabolic trend between the $N = 20$ and $N = 28$ shell gaps. Argon and sulfur deviate from the parabolic trend with lower excitation energies at $N = 26$ than at $N = 22$. This points to increased collectivity, but the previously noted reduction in the $\pi(0d_{3/2} - 1s_{1/2})$ gap may be to blame. The 2_1^+

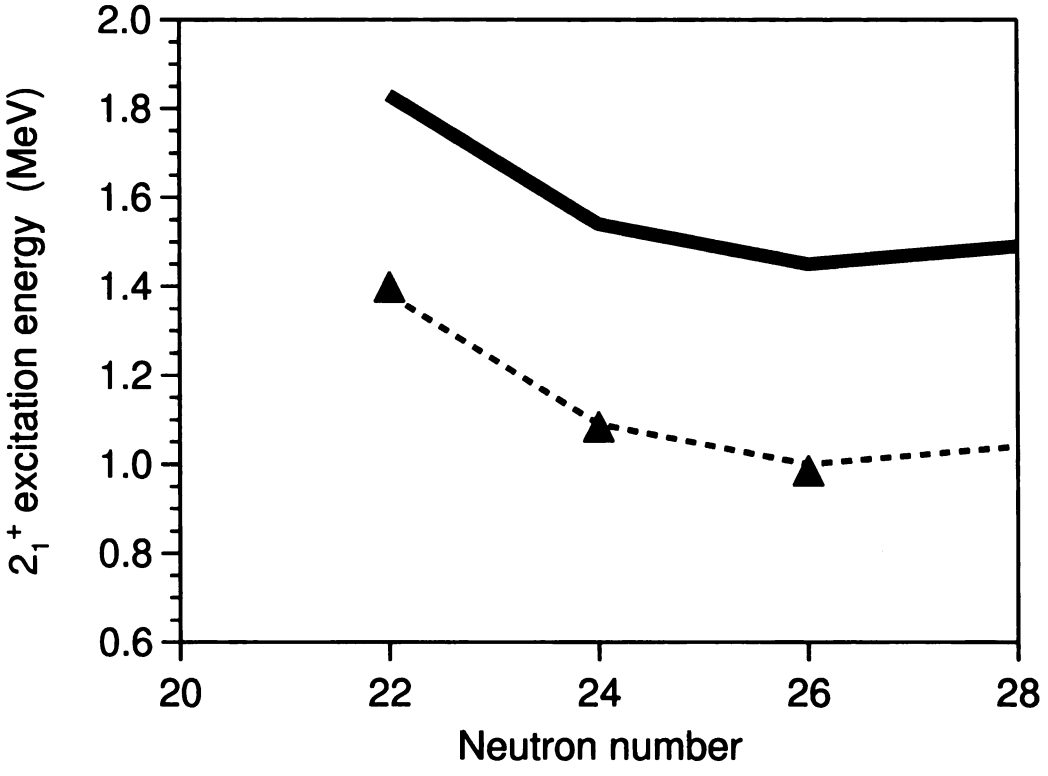

Figure 4.2: Measured and predicted silicon 2_1^+ energies are plotted as a function of neutron number. SDPF-NR shell-model calculations (solid line) give value that are systematically $\sim$ 450 keV greater than the measured energies. This suggests that refinement of the interaction may lead to the the dotted line values.

excitation energy of ^{40}Si deviates even more strongly from the parabolic prediction. This is the largest observed reduction in 2_1^+ excitation energy between $N = 24$ and $N = 26$ isotopes. The strong $Z = 14$ subshell closure directly ties the low 2_1^+ energy of ^{40}Si to a reduced $N = 28$ shell gap at $Z = 14$.

The evolution of silicon 2_1^+ excitation energies with neutron number was then compared with large-scale shell-model calculations. Shell-model calculations were performed in `OXBASH` [93] (for ^{36}Si) and `CMichSM` [94] (for ^{38,40,42}Si) in a $\pi(sd)^{Z-8}\,\nu(pf)^{N-20}$ model space using the SDPF-NR interaction [32]. Figure 4.2 shows the measured 2_1^+ energies as triangles and the shell-model results as a thick black line. Though a large offset is observed, the trend is reproduced nicely.

Comparisons between the calculated 2_1^+ energies and experimental data [92] in even-even sulfur and argon isotopes failed to show a large, systematic offset. Further-

more, the first excited states of $N = 22, 24, 26, 28$ phosphorus and chlorine isotopes were found to be in excellent agreement with calculations using this model space and interaction [95]. Finding the experimental values consistently 450 keV lower than the shell-model calculations could indicate some fault in the model inputs. (A dashed line showing the shell-model energies reduced by 450 keV is shown in figure 4.2.) Either some part of the interaction changes at $Z = 14$ or the even-N silicon isotopes are highlighting a particular part of the interaction, or both.

A possible explanation was suggested by Dr. B. A. Brown [96] who drew an analogy between the present situation and the neutron-rich carbon isotopes. Similar to silicon, the neutron-rich even-even carbon isotopes have a strong proton subshell closure. Shell model predictions using the interaction WBP successfully described the spectra of neutron-rich oxygen isotopes. Figure 4.3 shows the experimentally observed level scheme and the shell-model results for two interactions [97,98]. While the level spacing given by the WBP interaction is too large, the WBPM interaction reproduces the observed spacing quite well. The WBPM interaction is defined as the WBP interaction with a reduced neutron-neutron (n-n) interaction strength [97].

Changing the interaction strength affects not only the level spacing, but also the evolution of shell gaps. The neutron orbital $1s_{1/2}$ lies 0.87 MeV above the $0d_{5/2}$ orbital in ^{17}O, i.e. $Z = 8, N = 9$. The n-n interaction causes this gap to grow with increasing neutron number. This, in turn, results in a shell gap at $N = 14$ which makes ^{22}O doubly magic [99]. In carbon, the neutron orbitals are inverted at $N = 9$: $1s_{1/2}$ lies 0.74 MeV below $0d_{5/2}$. With no modification, WBP predicts $N = 14$ is not a shell closure in carbon. Including the weaker n-n interaction used in WBPM causes the $\nu(1s_{1/2} - 0d_{5/2})$ gap to grow more slowly, thus reinforcing that no shell gap develops at $N = 14$ in the carbon isotopes.

The evolution of level spacings and the $N = 14$ shell gap in the oxygen-carbon region may now be used to understand the similar features observed in the calcium-silicon region. Calculations of 2_1^+ energies in the $\pi(sd)\nu(fp)$ region performed with

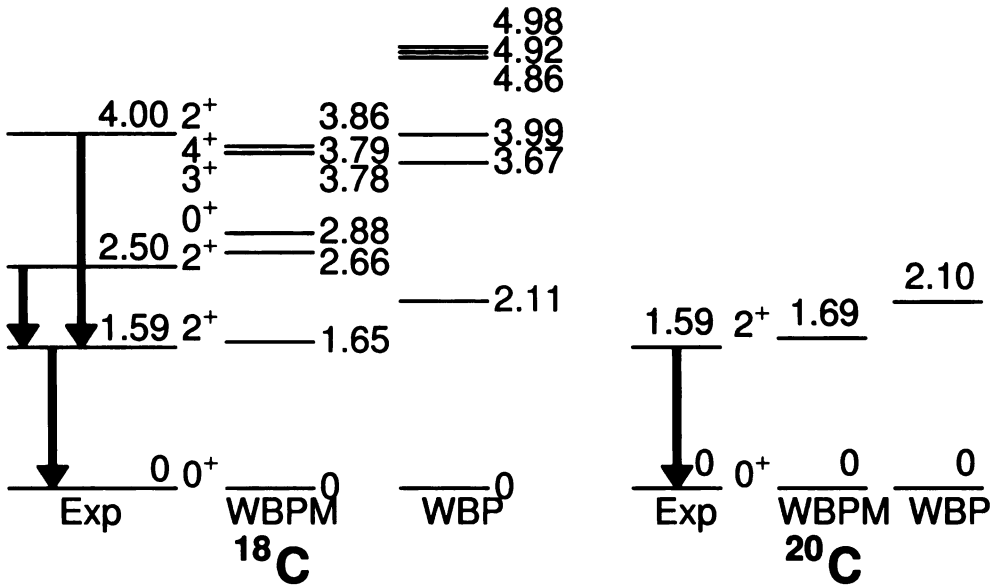

Figure 4.3: Experimental level schemes of ^{18,20}C along with shell-model predictions using the WBP and WBPM interactions. With the WBPM, reducing the valence n-n interaction strength leads to better agreement with experiment. A similar reduction in the valence n-n interaction may explain the discrepancy between measured silicon 2_1^+ energies and shell-model calculations using SDPF-NR.

the original SDPF-NR interaction [31] may serve as a baseline for comparison. That interaction used the $1p_{3/2} - 0f_{7/2}$ neutron gap from ^{41}Ca along with the n-n interaction found in stable nuclei—which is known to widen the $N = 28$ shell gap—to predict ^{42}Si as a doubly-magic nucleus with an E(2_1^+) of 2.5 MeV [31]. A subsequent β-decay experiment determined the $1p_{3/2} - 0f_{7/2}$ neutron gap in ^{35}Si. The observed $1p_{3/2}$ level was 1 MeV lower than expected, and the interaction was modified to account for the reduced shell gap. This had little impact on excitation energies other than ^{42}Si, which was then predicted to have E(2_1^+) of 1.5 MeV [35].

Figure 4.2 clearly shows the modified SDPF-NR interaction predicts a larger level spacing than is observed. Reducing the neutron-neutron (n-n) interaction strength for $Z = 14$ could correct the observed disagreement with experiment. A weaker n-n interaction would also cause the $N = 28$ shell gap to grow more slowly with neutron number, giving a smaller $N = 28$ gap at $Z = 14$ than is predicted by the current shell model interaction.

The deduced level scheme of ^{40}Si adds support to the proposition that the $N = 28$ shell gap is reduced at $Z = 14$. Though statistics were limited in the $p(^{42}\mathrm{P},^{40}\mathrm{Si} + \gamma)\mathrm{X}$ channel, a level either 1624(7) or 1831(8) keV was found, see section 3.2.3 for discussion. The existence of a level at such low energy above the 2_1^+ level at 986(5) keV would not be expected if the $N = 28$ shell gap were large. Figure 3.17 shows the observed level scheme and the shell-model calculation. In the shell-model calculations, states decaying by γ-rays of less than 1 MeV to the 2_1^+ level arise from particle-hole excitations across the $N = 28$ shell gap.

These observations:

- The decrease in 2_1^+ energy between $N = 24$ and $N = 26$ silicon isotopes
- The additional low-lying level observed in ^{40}Si
- The systematically smaller level spacing as compared to the current shell-model calculations

point to an $N = 28$ shell gap at $Z = 14$ which is even smaller than current predictions.

4.2 Quadrupole collectivity

Recalling section 1.2.2, collective nuclear states are often categorized as vibrational, rotational, or some combination thereof. Knowing the nature (vibrational/rotational) of a collective state may shed some light on their structure. Deformation parameters, $|\beta|$, correspond to the magnitude of the deformation, dynamic or static and may be used as quantitative measures of collectivity.

Extracting these deformation parameters from the measured inelastic proton scattering cross sections required the use of a specific collective model. Thus, the deformation parameters, $|\beta_{2,(p,p')}|$, presented here are model-dependent. Vibration, prolate rotation, and oblate rotation were used in the ECIS [39] calculations to deduce

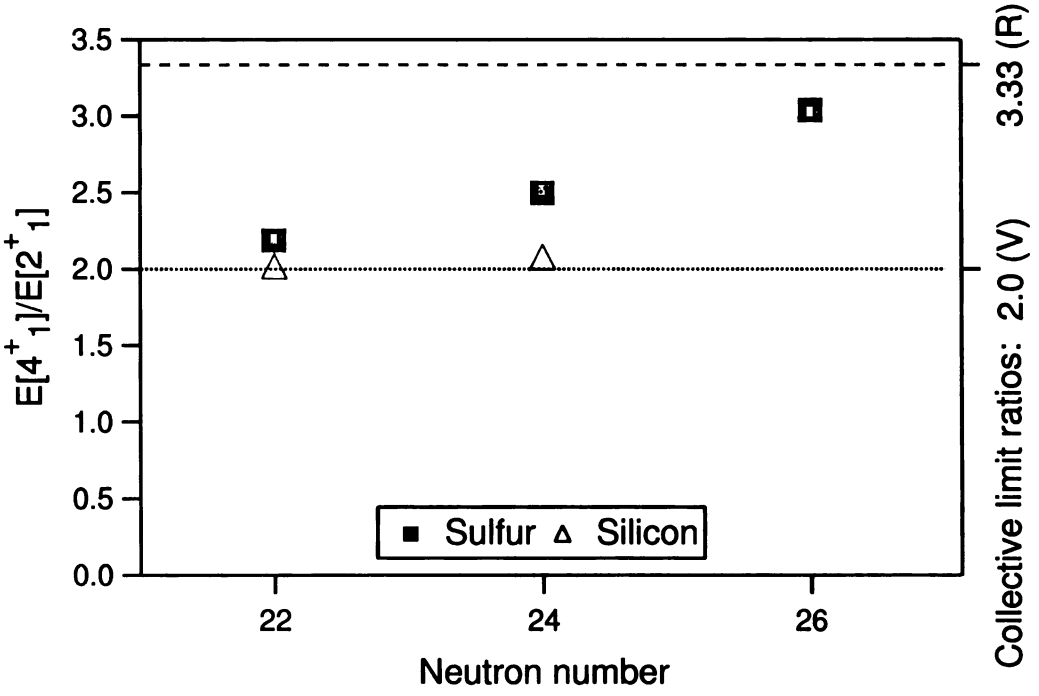

Figure 4.4: Ratios of excitation energies for the first 2^+ and 4^+ levels in neutron-rich, even-even sulfur and silicon nuclei filling the $\nu(0f_{7/2})$ orbital. Dotted and dashed lines show the values expected in the vibrational and rotational collective models.

$|\beta_{2,(p,p')}|$ from the measure inelastic cross-sections. For each nucleus, models consistent with the available data were used.

Figure 4.4 shows the ratios of excitation energies for the first 2^+ and 4^+ levels the even-A sulfur and silicon nuclei filling the $\nu(0f_{7/2})$ orbital. Data for ^{36}Si is from Ref. [85], and the ^{38}Si value is taken from the present analysis. These silicon isotopes show energy ratios consistent with the vibrational model. The strong proton sub-shell closure at $Z = 14$ likely prevents the coupling of proton and neutron excitations, which are associated with the development of static deformation [15,32]. Thus, the isotopes ^{36,38,40}Si were analyzed using the vibrational model.

Table 4.1 presents the measured inelastic proton-scattering cross sections and deduced deformation parameters, $|\beta_{2,(p,p')}|$, of the current experiment. For isotopes analyzed using more than one model, the average deformation parameter is used in subsequent tables and figures. Uncertainty limits will encompass the full uncertainty

for each model used. Example using ^{42}S:

$$|\beta_{2,(p,p'),average}| = (0.345 + 0.381)/2 = 0.363$$
$$|\beta_{2,(p,p'),lowerlimit}| = min(0.335, 0.369) = 0.335$$
$$|\beta_{2,(p,p'),upperlimit}| = max(0.355, 0.393) = 0.393$$
$$|\beta_{2,(p,p')}| = 0.36(3)$$

The sulfur isotopes show a steady increase in the ratio, $E[4_1^+]/E[2_1^+]$, with neutron number. This trend should be compared with figure 1.3, which shows the narrowing of the $Z = 16$ sub-shell gap with increasing neutron number. At $N = 22$, the proton sub-shell gap is still large, and ^{38}S has a ratio consistent with vibration. As the proton sub-shell gap narrows, the ratio, $E[4_1^+]/E[2_1^+]$, grows. ^{40}S has a transitional ratio, and calculations by Sohler *et al.* point to a γ-soft vibrational description. So, ^{40}S was analyzed using the vibrational model. ^{42}S has a ratio > 3, pointing to rotational character. The narrowed $Z = 16$ sub-shell gap allows for both enhanced proton collectivity and a coupling of proton and neutron collective excitations. This culminates in rotational behavior at $N = 26$. Although oblate deformation is predicted in ^{42}S, no experiment has probed the sign of the deformation. Both prolate and oblate models were used for ^{42}S. The low-lying structure of ^{44}S is quite complicated. Observation of

Table 4.1: Inelastic proton-scattering cross sections, deformation parameters of the current experiment ($|\beta_{2,(p,p')}|$) are given for ^{36,38,40}Si and ^{40,42,44}S.

N	$\sigma_{0_1^+ \to 2_1^+}$ (mb)	$\lvert\beta_{2,(p,p')}\rvert$		
		vibrational	prolate	oblate
^{36}Si	7.4(24)	0.24(4)		
^{38}Si	15.4(26)	0.35(3)		
^{40}Si	20^{+2}_{-4}	0.37^{+2}_{-4}		
^{40}S	19.8(12)	0.384(12)		
^{42}S	16.3(10)		0.34(1)	0.38(1)
^{44}S	12.5(9)	0.28(1)	0.27(1)	0.30(1)

Table 4.2: Deformation parameters of the current experiment ($|\beta_{2,(p,p')}|$) and a previous Coulomb excitation measurement ($|\beta_{2C}|$) [84], shell-model matrix elements A_p and A_n, and experimental and shell-model $(\frac{M_n}{M_p})/(\frac{N}{Z})$ ratios are given for ^{36,38,40}Si.

N	$\lvert\beta_{2,(p,p')}\rvert$	$\lvert\beta_{2C}\rvert$	A_p (fm)	A_n (fm)	$(\frac{M_n}{M_p})/(\frac{N}{Z})_{expt}$	$(\frac{M_n}{M_p})/(\frac{N}{Z})_{SM}$
22	0.24(4)	0.26(4)	5.44	13.1	0.89^{+23}_{-24}	0.95
24	0.35(3)	0.25(5)	5.04	19.7	1.58^{+32}_{-32}	0.84
26	0.37^{+2}_{-4}	-	5.28	23.5	-	0.82

an isomeric 0^+_2 state at an excitation energy of 1.365(1) MeV [91] is consistent with the prediction of shape coexistence in this nucleus [100]. All three models were used to analyze ^{44}S.

4.2.1 Collectivity in silicon isotopes

Figure 4.5 shows the deformation parameters, $|\beta_{2,(p,p')}|$, deduced in this experiment and the corresponding $|\beta_{2,C}|$ values from a Coulomb excitation experiment [84] plotted against N for ^{36,38,40}Si. If both the $N = 20$ and $N = 28$ shell gaps were large, filling of the $\nu(0f_{7/2})$ orbital would dominate changes in the excitation energy and collectivity of the 2^+_1 state in this isotopic chain. As discussed in section 4.1, a symmetric, parabolic trend was expected in the energies, but the ^{40}Si 2^+_1 energy was significantly lower than the simple prediction. The deformation parameters are, likewise, expected to vary symmetrically about mid-shell, $N = 24$. However, collectivity is expected to be maximum at mid-shell. This model fails to predict the large deformation parameter of ^{40}Si. Instead, ^{36}Si has the smallest collectivity, and ^{38,40}Si are similarly collective.

Unlike the collectivity changes in the sulfur isotopes, the increased collectivity at $N = 26$ does not appear to arise due to changes in the proton sub-shell gaps. With a large $Z = 14$ sub-shell gap from $N = 20 - 28$, the contribution of valence protons to collectivity is small and roughly constant in these isotopes. Only neutron

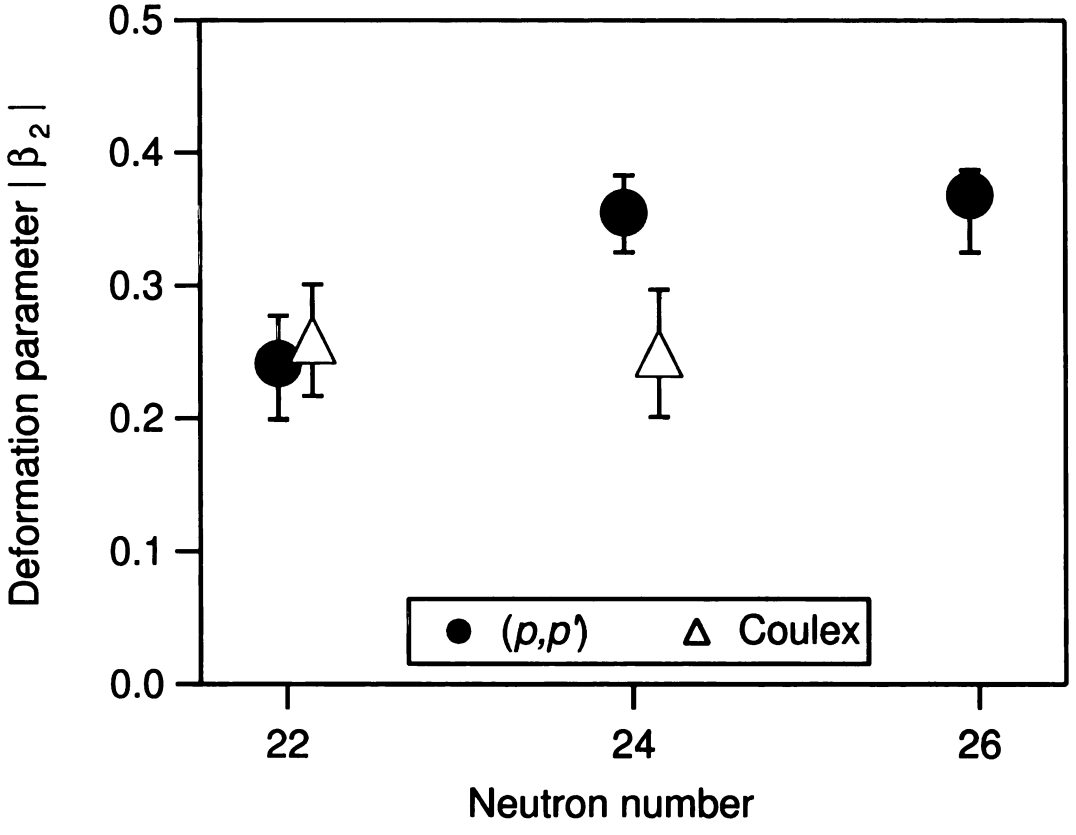

Figure 4.5: Deformation parameters $|\beta_{2,(p,p')}|$ and previously measured $|\beta_{2,C}|$ [84] are plotted against neutron number for the nuclei ^{36,38,40}Si.

excitations across the $N = 28$ shell gap can explain the increased collectivity in ^{40}Si. This increased collectivity is direct evidence that the $N = 28$ shell gap has narrowed at $Z = 14$.

Comparing the deformation parameters $|\beta_{2,(p,p')}|$ deduced here with those of Coulomb excitation, one may extract the relative proton and neutron contributions to the collective 2_1^+ excitation. As discussed in section 2.1.3, a simple collective model of the nucleus predicts equal deformations for protons and neutrons. This leads to proton and neutron transition matrix elements in direct proportion to the number of protons and neutrons (i.e. $\frac{M_n}{M_p} = \frac{N}{Z}$). To compare isotopes, the ratio of neutron to proton matrix elements will be divided by N/Z. Table 4.2 presents the deformation parameters, shell-model matrix elements, and experimental and predicted $\frac{M_n}{M_p} = \frac{N}{Z}$.

Before discussing these results, it is important to review the inputs used in these shell model predictions. Specifically, the polarization charges must be carefully considered. Recalling the discussion in section 1.2.1, matrix elements resulting from a shell-model calculation are not sufficient to describe the transitions among states. Coupling of valence nucleons to excitations of the core are handled through polarization charges, δ. Both like and unlike nucleon couplings occur, and the final matrix elements, M_n and M_p, are linear combinations of the valence space matrix elements, A_n and A_p.

In the present analysis, four sets of polarization charges were considered. Table 4.3 lists three polarization charge sets which use the simplifying assumption that $\delta_{pp} = \delta_{nn}$ and $\delta_{pn} = \delta_{np}$. These sets represent the standard isoscalar choice a set with a significant isovector component — which has been suggested in the pf shell [101],

Table 4.3: Three sets of polarization charges considered for analyzing $\frac{M_n}{M_p} = \frac{N}{Z}$.

Polarization set	δ_{pp}	δ_{pn}
isoscalar	0.5	0.5
sd-shell	0.2	0.5
duRietz (pf)	0.2	0.8

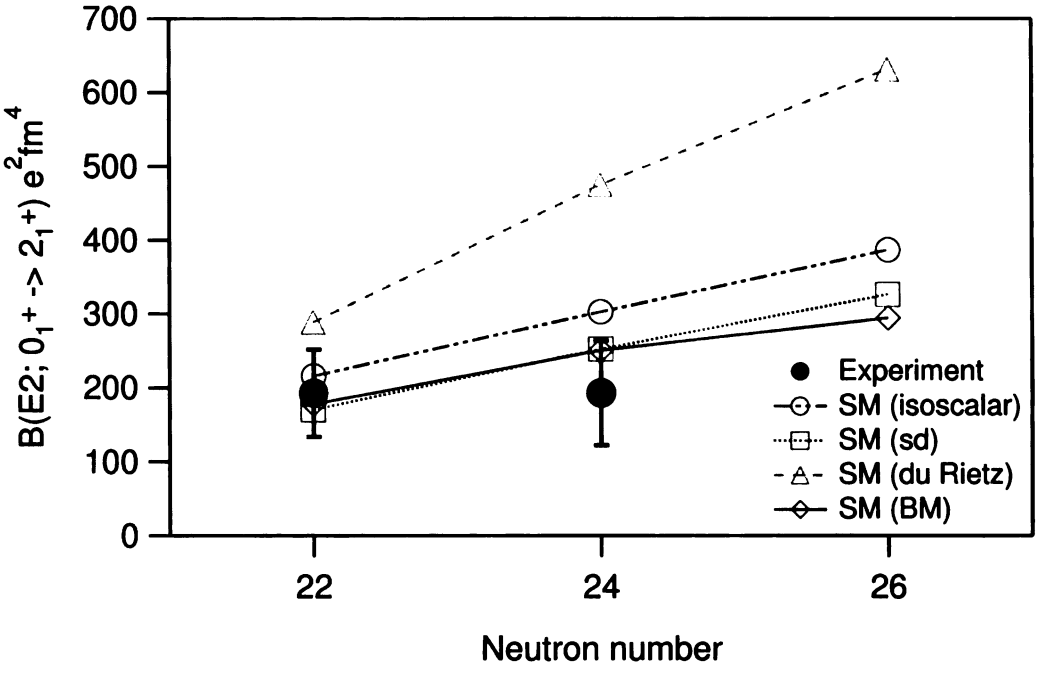

Figure 4.6: Measured B(E2↑) values are plotted versus neutron number N for $\nu(0f_{7/2})^{2n}$ silicon nuclei. Shell model predictions using various polarization charges are compared to data.

and the accepted polarization charges for the *sd* shell [102]. A fourth set — suggested by Dr. H. Sagawa — was an extension of the Bohr-Mottelson effective charge model, given in Eq. 6-386a of Ref [11]. The original model focused only on proton excitations of the core and was directed at correctly predicting B(E2) values. This model was explicitly constructed to handle changes in core polarization due to the N/Z of a given isotope. By applying the original reasoning to neutron excitations of the core, one may calculate all four polarization charges.

Each polarization charge set was used with the valence space matrix elements to calculate B(E2; $0_1^+ \rightarrow 2_1^+$) values for ^{36,38,40}Si. Figure 4.6 compares the results using each polarization charge set to the measured values for ^{36,38}Si [84]. The isovector *pf*-shell set clearly disagrees with the data. Both the *sd*-shell and extended Bohr-Mottelson sets give similar, good agreement with measured data. The *sd*-shell polarization charge set has been used to in table 4.2.

Figure 4.7 shows $(\frac{M_n}{M_p})/(\frac{N}{Z})$ plotted versus neutron number for experiment and

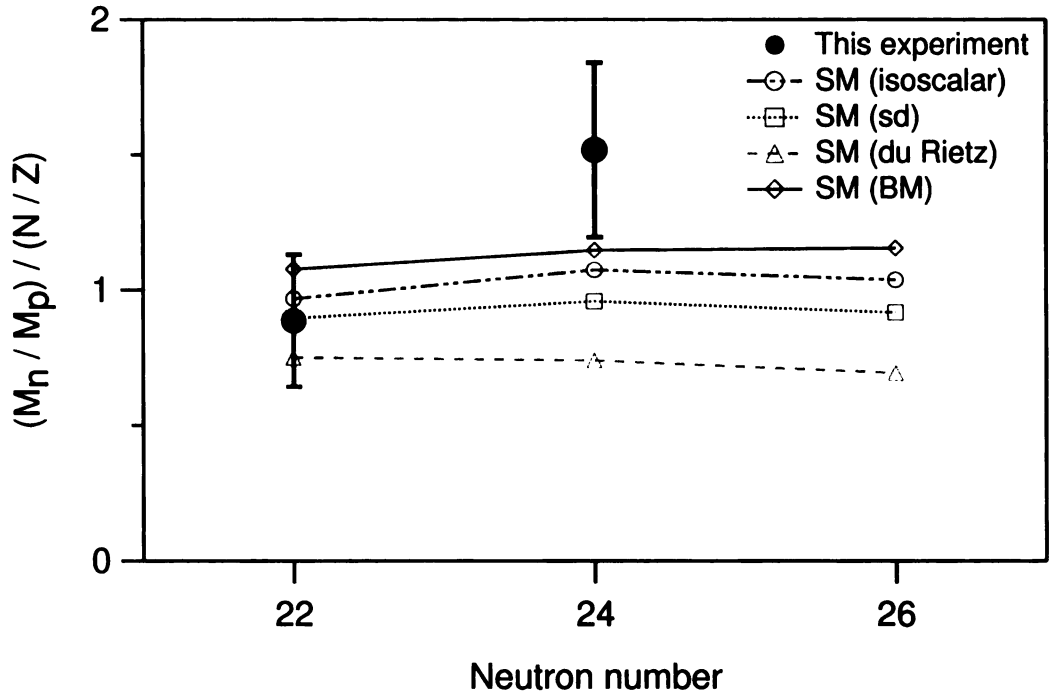

Figure 4.7: Normalized ratios of neutron-to-proton matrix elements, $(\frac{M_n}{M_p})/(\frac{N}{Z})$, are plotted versus neutron number N for silicon isotopes. Experimental results are compared to shell model predictions using various polarization charges.

each set of polarization charges. The large error bar for ^{36}Si is dominated by experimental uncertainties, with equal contributions from the present (p, p') experiment and the Coulomb excitation experiment. In the case of ^{38}Si, the Coulomb excitation uncertainty is dominant. The study of neutron and proton collectivity in the neutron-rich silicon isotopes would greatly benefit from a precision Coulomb excitation experiment on ^{36,38,40}Si.

Given the large error bars, ^{36}Si is consistent with both shell model and the simple collective model prediction. The neutron collectivity appears to increase significantly at $N = 24$ with no similar rise in proton collectivity. This large increase is not found in shell-model calculations. Three alternatives may be used to explain the possible discrepancy in ^{38}Si:

- a deficiency in the shell model such as a too-large $N = 28$ shell gap
- an enhanced core neutron – valence neutron coupling

- an overestimation of $|\beta_{2,(p,p')}|$ due to the formation of a neutron skin.

The latter two possibilities have also been suggested to explain enhanced neutron collectivity observed in ^{38,40}S [68, 103]. Differential cross sections with respect to scattering angle — as are measured in proton-detection (p, p') — are required to probe the different proton and neutron density distributions.

4.2.2 Collectivity in sulfur isotopes

The analysis of sulfur collectivity parallels the previous section on silicon collectivity. Figure 4.8 shows the deformation parameters, $|\beta_{2,(p,p')}|$, deduced in this experiment and previous experiments studying ^{36,38,40}S [45, 68] and the corresponding $|\beta_{2,C}|$ values from Coulomb excitation [104]. Here, the isotopes at $N = 20, 28$ have also been studied. Assuming large shell gaps at $N = 20, 28$, one would expect collectivity minima at the shell gaps with symmetric increases toward a maximum at $N = 24$. Instead, the Coulomb excitation data show a steady increase from $N = 20 - 26$, and the $|\beta_{2,(p,p')}|$ values show a sharp rise at $N = 22$. Both show declining collectivity at $N = 28$, but the (p, p') value has more statistical significance.

These observations can be explained by considering the evolution of the $\pi(1s_{1/2} - 0d_{3/2})$ gap with increasing neutron number and its impact on collectivity. As discussed in section 1.3, this $Z = 16$ proton sub-shell gap is known to narrow from $N = 20$ to $N = 28$. This not only increases the proton collectivity, but allows proton and neutron collective excitation to couple [32]. The result is a region of deformation near ^{42}S. Coupling of proton and neutron collectivity and the near degeneracy of the $\pi(1s_{1/2})$ and $\pi(0d_{3/2})$ orbitals at $N = 28$ has obscured changes in the $N = 28$ shell gap for sulfur and the neighboring $Z = 15, 17$ isotopic chains.

In fact, the Coulomb excitation data leave open the possibility that the collectivities of ^{42}S and ^{44}S are the same. Subtracting the observed $|\beta_{2,C}|$ value of ^{44}S from that of ^{42}S yields 0.046 ± 0.044. From this data alone, there appears to be a fair

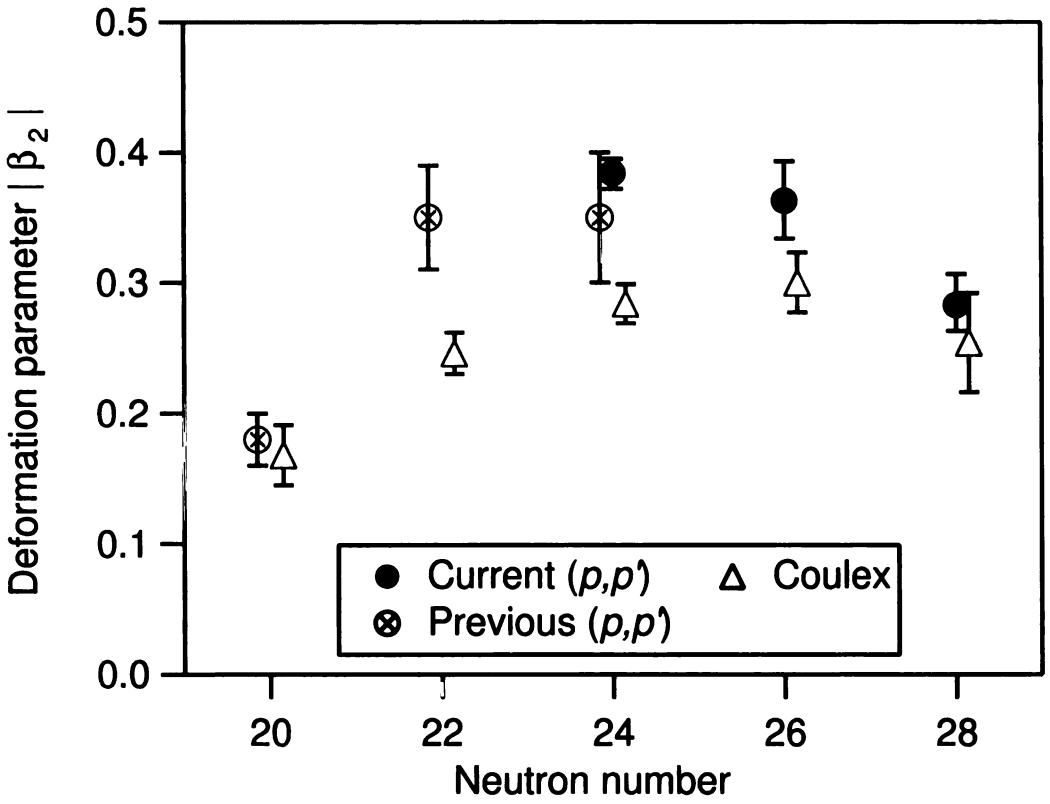

Figure 4.8: Deformation parameters $|\beta_{2,(p,p')}|$ deduced in this experiment and $|\beta_{2,(p,p')}|$ and $|\beta_{2,C}|$ from previous experiments are plotted against neutron number for the nuclei ^{38,40,42,44}S.

Table 4.4: Deformation parameters of the current experiment ($|\beta_{2,(p,p')}|$) and a previous Coulomb excitation measurement ($|\beta_{2C}|$) [84], shell-model matrix elements A_p and A_n, and experimental and shell-model $(\frac{M_n}{M_p})/(\frac{N}{Z})$ ratios are given for ^{40,42,44}S.

N	$\lvert\beta_{2,(p,p')}\rvert$	$\lvert\beta_{2C}\rvert$	A_p (fm)	A_n (fm)	$(\frac{M_n}{M_p})/(\frac{N}{Z})_{expt}$	$(\frac{M_n}{M_p})/(\frac{N}{Z})_{SM}$
24	0.386(12)	0.284(15)	7.28	18.2	1.41(10)	0.95
26	0.36(3)	0.300(23)	8.27	18.4	1.24(16)	0.84
28	0.283^{+24}_{-20}	0.254(38)	8.01	20.1	1.12(22)	0.82

chance that the $N = 28$ shell gap has significantly eroded at $Z = 16$.

Examining the present $|\beta_{2,(p,p')}|$ results is more difficult because the model dependence of the extracted deformation parameters forces one to consider a matrix of $|\beta_{2,(p,p')}|$ differences. In all cases, ^{42}S has a larger deformation parameter than ^{44}S. The least statistically significant difference was between prolate rotational ^{42}S and oblate rotational ^{44}S, which gave a $\Delta|\beta_{2,(p,p')}|$ of 0.048 ± 0.015. This case runs contrary to shell model and mean field calculations which suggest static oblate deformation in ^{42}S and shape coexistence in ^{44}S. All other differences are $> 5\sigma$. Thus, the present data gives evidence for a decline in collectivity between ^{42}S and ^{44}S.

Table 4.4 lists the deformation parameters determined in this experiment and previous Coulomb excitation experiments, the shell-model valence space matrix elements, and M_n/M_p values normalized by N/Z determined experimentally and calculated in the shell model. As in the silicons, the *sd*-shell polarization charges were used. The experimental ratio of neutron to proton collectivity falls from $N = 24$ to $N = 28$. This behavior arises from a small decrease in neutron collectivity and a large increase in proton collectivity as the neutron $0f_{7/2}$ orbital fills. Only ^{44}S is consistent with $M_n/M_p = N/Z$, and even this result contradicts expectations. Since the $Z = 16$ sub-shell gap vanishes at $N = 28$, ^{44}S is a single-closed-shell nucleus with neutrons forming the closed shell. Thus, one expects $M_n/M_p < N/Z$.

Large uncertainties do not, however, allow $M_n/M_p < N/Z$ to be ruled out for

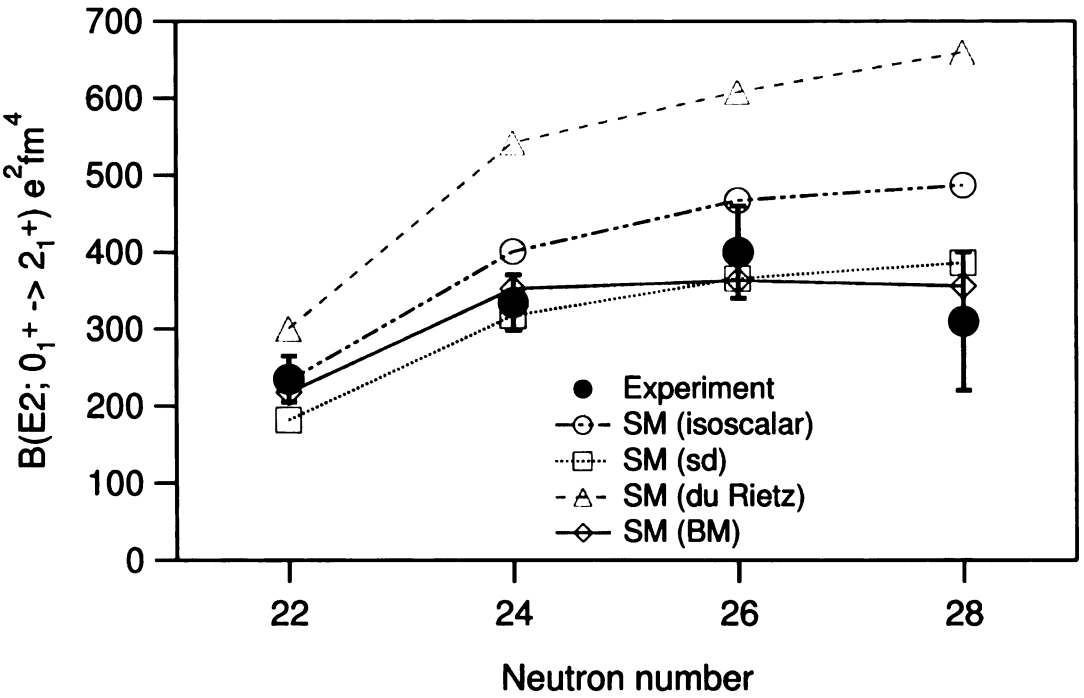

Figure 4.9: Measured B(E2↑) values are plotted versus neutron number N for $\nu(0f_{7/2})^{2n}$ sulfur nuclei. Shell model predictions using various polarization charges are compared with data.

^{44}S. Two main sources of uncertainty exist: the Coulomb excitation experimental uncertainties and the model dependence inherent in extracting $|\beta_{2,(p,p')}|$. As in the silicons, a precision measurement of the Coulomb excitation of ^{40,42,44}S at higher statistics would significantly improve the present analysis. A measurement of the static quadrupole moment, including the sign, of the ^{42,44}S ground states would allow selection of the appropriate collective model.

As before, shell-model results using the three sets of polarization charges from table 4.3 and the extended Bohr-Mottelson polarization charges are compared with data. Figure 4.9 shows experimental and calculated B(E2↑) values for ^{38,40,42,44}S plotted versus neutron number. Experimental B(E2↑) values were taken from the compilation of Raman *et al.* [104]. In line with the silicon results, the isoscalar and duReitz polarization charges given larger B(E2↑) values than are observed in experiment. B(E2↑) values calculated using polarization charge sets from the extended Bohr-Mottelson model and the *sd* shell give good agreement with data.

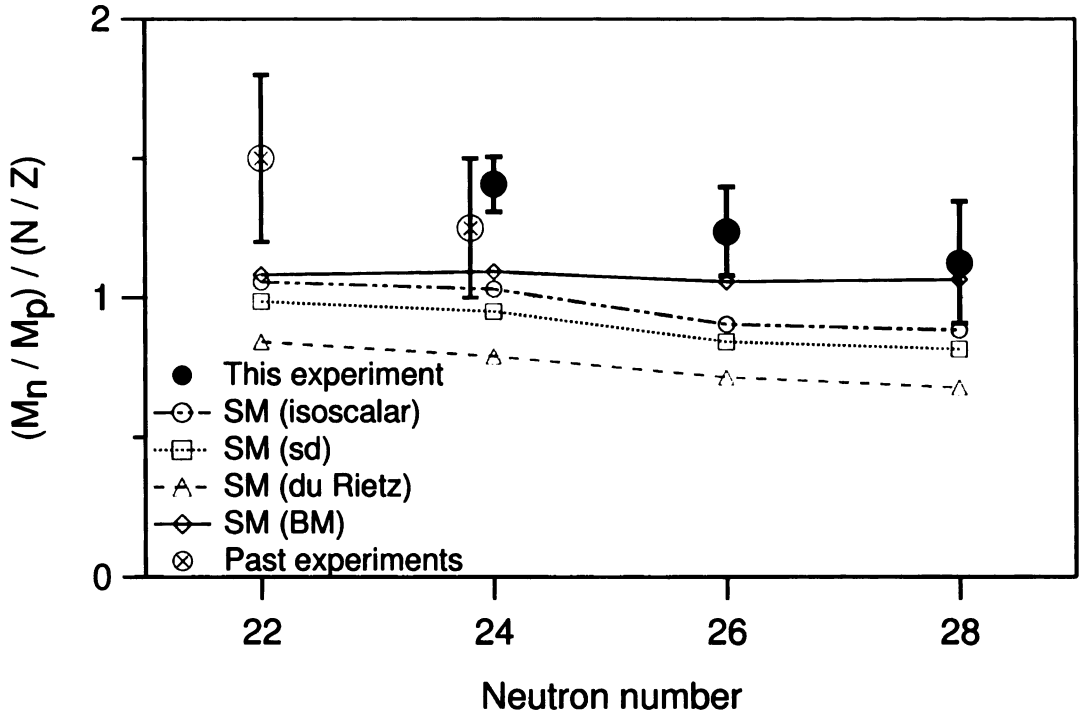

Figure 4.10: Normalized ratios of neutron-to-proton matrix elements, $(\frac{M_n}{M_p})/(\frac{N}{Z})$, are plotted versus neutron number N for sulfur isotopes. Experimental results are compared to shell model predictions using various polarization charges.

Figure 4.10 plots the $(\frac{M_n}{M_p})/(\frac{N}{Z})$ values versus neutron number. Values from the present analysis and from a previous set of experiments are shown along with shell-model calculations using each of the four polarization charges sets previously discussed. Although the experimental ratios of all nuclei overlap within their 1σ error bars, the central values show a steady decline with increasing N. Shell-model calculations show a similar trend but give lower neutron collectivity than is observed.

Chapter 5

Conclusion

Inelastic proton scattering cross sections, $\sigma_{(p,p')}[0_1^+ \rightarrow 2_1^+]$, have been measured for ^{36,38,40}Si and ^{40,42,44}S. Measurements were performed by the thick-target, γ-ray tagging method. Four state-of-the-art systems — A1900, S800, SeGA, and the RIKEN-Kyushu-Rikkyo liquid hydrogen target — were coupled to make efficient use of the rare isotopes being investigated.

The 2_1^+ excitation energy in ^{40}Si is lower than would be expected if $N = 28$ had a large shell gap at $Z = 14$. Proton single particle energies measured in stable nuclei indicate a large, stable $Z = 14$ subshell gap [29]. Therefore, the decline in 2_1^+ energies for $N = 24$ to $N = 26$ is directly tied to a narrowing of the $N = 28$ shell gap between $Z = 20$ and $Z = 14$. A systematic difference between measured 2_1^+ energies and shell-model values found only in the silicon isotopes is suggested as evidence of a Z-dependent weakening of the $n - n$ interaction. A low-lying second excited state observed in ^{40}Si results from neutron excitations across the $N = 28$ shell gap.

Measurements on ^{36,38}Si and ^{40,42,44}S have led to their level schemes. In ^{38}Si, the location of the 4_1^+ level appears to confirm the expectation of vibrational collectivity in this nucleus. Recently published mass measurements in this region show no evidence of deformation in the $N = 20 - 28$ silicon isotopes, but leave open the possibility of a rapid onset of deformation at $N = 28$ [105].

Quadrupole collectivity has been measured in each of these nuclei by the extraction of model-dependent deformation parameters, $|\beta_{2,(p,p')}|$. In the silicon isotopes, an asymmetry about mid-shell — $N = 24$– is observed with ^{40}Si being more collective than ^{36}Si, and perhaps equally collective as ^{38}Si. As with the energies, the increased collectivity is directly tied to a reduction in the $N = 28$ shell gap. In the sulfur chain, $|\beta_{2,(p,p')}|$ values provide a clear, quantitative measurement of the decrease in collectivity between ^{42}S and ^{44}S. This fits nicely into the shell-model description by Retamosa *et al.* of a localized region of deformation centered on ^{42}S [31].

BIBLIOGRAPHY

[1] M. G. Mayer. *Phys. Rev.*, 74:235–239, 1948.

[2] M. G. Mayer. *Phys. Rev.*, 75:1969–1970, 1949.

[3] O. Haxel, J. Hans D. Jensen, and Hans E. Suess. *Phys. Rev.*, 75:1766, 1949.

[4] J. Blomqvist and A. Molinari. *Nucl. Phys. A*, 106:545–569, 1968.

[5] B. A. Brown. Nuclear structure physics. Lecture notes, 2003.

[6] B. A. Brown and W. A. Richter. *Phys. Rev. C*, 74:034315, 2006.

[7] B. A. Brown and B. H. Wildenthal. *Annu. Rev. Nucl. Part. Sci.*, 38:29–66, 1988.

[8] B. A. Brown. *Prog. Part. Nucl. Phys.*, 47:517–599, 2001.

[9] E. Caurier, G. Martínez-Pinedo, F. Nowacki, A. Poves, and A. P. Zuker. *Rev. Mod. Phys.*, 77:427–488, 2005.

[10] V. R. Pandharipande, I. Sick, and P. K. A. deWitt Huberts. *Rev. Mod. Phys.*, 69:981–991, 1997.

[11] A. Bohr and B. R. Mottelson. *Nuclear Structure*, volume 2. World Scientific, New Jersey, 1998.

[12] B. A. Brown and B. H. Wildenthal. *Phys. Rev. C*, 21:2107–2110, 1980.

[13] W. Greiner and J. A. Maruhn. *Nuclear Models.* Springer-Verlag, New York, 1996.

[14] R. F. Casten. *Nuclear Structure from a Simple Perspective.* Oxford University Press, New York, 2000.

[15] J. Dobaczewski, W. Nazarewicz, J. Skalski, and T. Werner. *Phys. Rev. Lett.*, 60:2254–2257, 1988.

[16] A. Bohr and B. R. Mottelson. *Nuclear Structure*, volume 1. World Scientific, New Jersey, 1998.

[17] P. Federman, S. Pittel, and R. Campos. *Phys. Lett. B*, 82:9 -12, 1979.

[18] K. Heyde, P. Van Isacker, R. F. Casten, and J. L. Wood. *Phys. Lett. B*, 155:303–308, 1985.

[19] T. Otsuka, R. Fujimoto, Y. Utsuno, B. A. Brown, M. Honma, and T. Mizusaki. *Phys. Rev. Lett.*, 87:082502, 2001.

[20] C. Thibault, R. Klapisch, C. Rigaud, A. M. Poskanzer, R. Prieels, L. Lessard, and W. Reisdorf. *Phys. Rev. C*, 12:644–657, 1975.

[21] X. Campi, H. Flocard, A. K. Kerman, and S. Koonin. *Nucl. Phys. A*, 251:193–205, 1975.

[22] E. K. Warburton, J. A. Becker, and B. A. Brown. *Phys. Rev. C*, 41:1147–1166, 1990.

[23] T. Motobayashi, Y. Ikeda, K. Ieki, M. Inoue, N. Iwasa, T. Kikuchi, M. Kurokawa, S. Moriya, S. Ogawa, H. Murakami, S. Shimoura, Y. Yanagisawa, T. Nakamura, Y. Watanabe, M. Ishihara, T. Teranishi, H. Okuno, and R. F. Casten. *Phys. Lett. B*, 346:9–14, 1995.

[24] K. Yoneda, H. Sakurai, T. Gomi, T. Motobayashi, N. Aoi, N. Fukuda, U. Futakami, Z. Gacsi, Y. Higurashi, N. Imai, N. Iwasa, H. Iwasaki, T. Kubo, M. Kunibu, M. Kurokawa, Z. Liu, T. Minemura, A. Saito, M. Serata, S. Shimoura, S. Takeuchi, Y. X. Watanabe, K. Yamada, Y. Yanagisawa, K. Yogo, A. Yoshida, and M. Ishihara. *Phys. Lett. B*, 499:233–237, 2001.

[25] Y. Yanagisawa, M. Notani, H. Sakurai, M. Kunibu, H. Akiyoshi, N. Aoi, H. Baba, K. Demichi, N. Fukuda, H. Hasegawa, Y. Higurashi, M. Ishihara, N. Iwasa, H. Iwasaki, T. Gomi, S. Kanno, M. Kurokawa, Y. U. Matsuyama, S. Michimasa, T. Minemura, T. Mizoi, T. Nakamura, A. Saito, M. Serata, S. Shimoura, T. Sugimoto, E. Takeshita, S. Takeuchi, K. Ue, K. Yamada, K. Yoneda, and T. Motobayashi. *Phys. Lett. B*, 566:84–89, 2003.

[26] J. R. Terry, D. Bazin, B. A. Brown, C. M. Campbell, J. A. Church, J. M. Cook, A. D. Davies, D. C Dinca, J. Enders, A. Gade, T. Glasmacher, P. G. Hansen, J. L. Lecouey, T. Otsuka, B. Pritychenko, B. M. Sherrill, J. A. Tostevin, Y. Utsuno, K. Yoneda, and H. Zwahlen. *Phys. Lett. B*, 640:86–90, 2006.

[27] O. Sorlin, D. Guillemaud-Mueller, A. C. Mueller, V. Borrel, S. Dogny, F. Pougheon, K.-L. Kratz, H. Gabelmann, B. Pfeiffer, A. Wöhr, W. Ziegert, Yu. E. Penionzhkevich, S. M. Lukyanov, V. S. Salamatin, R. Anne, C. Borcea, L. K. Fifield, M. Lewitowicz, M. G. Saint-Laurent, D. Bazin, C. Détraz, F.-K. Thielemann, and W. Hillebrandt. *Phys. Rev. C*, 47:2941–2953, 1993.

[28] T. Glasmacher, B. A. Brown, M. J. Chromik, P. D. Cottle, M. Fauerbach, R. W. Ibbotson, K. W. Kemper, D. J. Morrissey, H. Scheit, D. W. Sklenicka, and M. Steiner. *Phys. Lett. B*, 395:163–168, 1997.

[29] P. D. Cottle and K. W. Kemper. *Phys. Rev. C*, 58:3761–3762, 1998.

[30] P. Doll, G. J. Wagner, K. T. Knpfle, and G. Mairle. *Nucl. Phys. A*, 263:210–236, 1976.

[31] J. Retamosa, E. Caurier, F. Nowacki, and A. Poves. *Phys. Rev. C*, 55:1266–1274, 1997.

[32] E. Caurier, F. Nowacki, and A. Poves. *Nucl. Phys. A*, 742:14–26, 2004.

[33] J. Fridmann, I. Wiedenhöver, A. Gade, L. T. Baby, D. Bazin, B. A. Brown, C. M. Campbell, J. M. Cook, P. D. Cottle, E. Diffenderfer, D.-C. Dinca, T. Glasmacher, P. G. Hansen, K. W. Kemper, J. L. Lecouey, W. F. Mueller, H. Olliver, E. Rodriguez-Vieitez, J. R. Terry, J. A. Tostevin, and K. Yoneda. *Nature*, 435:922–924, 2005.

[34] J. Fridmann, I. Wiedenhöver, A. Gade, L. T. Baby, D. Bazin, B. A. Brown, C. M. Campbell, J. M. Cook, P. D. Cottle, E. Diffenderfer, D.-C. Dinca, T. Glasmacher, P. G. Hansen, K. W. Kemper, J. L. Lecouey, W. F. Mueller, E. Rodriguez-Vieitez, J. R. Terry, J. A. Tostevin, K. Yoneda, and H. Zwahlen. *Phys. Rev. C*, 74:034313, 2006.

[35] S. Nummela, P. Baumann, E. Caurier, P. Dessagne, A. Jokinen, A. Knipper, G. Le Scornet, C. Miehé, F. Nowacki, M. Oinonen, Z. Radivojevic, M. Ramdhane, G. Walter, and J. Äystö. *Phys. Rev. C*, 63:044316, 2001.

[36] A. M. Bernstein, V. R. Brown, and V. A. Madsen. *Phys. Lett. B*, 103:255–258, 1981.

[37] A. M. Berstein, V. R. Brown, and V. A. Madsen. *Comments Nucl. Part. Phys.*, 11:203, 1983.

[38] P. D. Cottle. *Nucl. Phys. A*, 682:124c–130c, 2001.

[39] J. Raynal. *Notes on* `ECIS94`, 1994.

[40] N. Austern. *Direct Nuclear Reaction Theories.* John Wiley and Sons, Inc., New York, 1970.

[41] G. R. Satchler. *Direct Nuclear Reactions.* Oxford University Press, New York, 1983.

[42] E. Merzbacher. *Quantum Mechanics.* John Wiley and Sons, Inc., New York, 1998.

[43] C. A. Bertulani and P. Danielewicz. *Introduction to Nuclear Reactions.* Taylor and Francis, New York, 2004.

[44] A. J. Koning and J. P. Delaroche. *Nucl. Phys. A*, 713:231–310, 2003.

[45] J. H. Kelley, T. Suomijärvi, S. E. Hirzebruch, A. Azhari, D. Bazin, Y. Blumenfeld, J. A. Brown, P. D. Cottle, S. Danczyk, M. Fauerbach, T. Glasmacher, J. K. Jewell, K. W. Kemper, F. Maréchal, D. J. Morrissey, S. Ottini, J. A. Scarpaci, and P. Thirolf. *Phys. Rev. C*, 56:R1206–R1209, 1997.

[46] A. Bohr. *Physica*, 22:959–968, 1956.

[47] B. L. Cohen and A. G. Rubin. *Phys. Rev.*, 111:1568–1577, 1958.

[48] A. M. Bernstein, V. R. Brown, and V. A. Madsen. *Phys. Lett. B*, 106:259–263, 1981.

[49] V. R. Brown and V. A. Madsen. *Phys. Rev. C*, 11:1298–1311, 1975.

[50] J. A. Carr, F. Petrovich, and J. J. Kelly. In *Neutron-Nucleus Collisions - A Probe of Nuclear Structure*, volume 124, pages 230–255. American Institute of Physics, 1985.

[51] M. A. Franey and W. G. Love. *Phys. Rev. C*, 31:488–498, 1985.

[52] G. Bertsch, J. Borysowicz, H. McManus, and W. G. Love. *Nucl. Phys. A*, 284:399–419, 1977.

[53] P.G. Hansen and J.A. Tostevin. *Annu. Rev. Nucl. Part. Sci.*, 53:219–261, 2003.

[54] G Jacob and Th. A. J. Maris. *Rev. Mod. Phys.*, 38:121–142, 1966.

[55] G Jacob and Th. A. J. Maris. *Rev. Mod. Phys.*, 45:6, 1973.

[56] J. R. Grover and A. A. Caretto. *Annu. Rev. Nucl. Sci.*, 14:51–100, 1964.

[57] H. P. Yule and A. Turkevich. *Phys. Rev.*, 118:1591–1598, 1960.

[58] A. Van Der Woude. *Prog. Part. Nucl. Phys.*, 18:217–293, 1987.

[59] J. Speth. *Electric and Magnetic Giant Resonances in Nuclei.* World Scientific, New Jersey, 1991.

[60] K. Starosta, 2006. Private communication.

[61] A. Gade, 2006. Private communication.

[62] B. A. Brown, 2005. Private communication.

[63] H Geissel, G Munzenberg, and K Riisager. *Annu. Rev. Nucl. Part. Sci.*, 45:163–203, 1995.

[64] R. Serber. *Phys. Rev.*, **72**:1008, 1947.

[65] F. Marti, D. Poe, M. Steiner, J. Stetson, and X.Y. Wu. In *Proceedings of the 16th International Conference on Cyclotrons and Their Applications*, volume 600, pages 64–68. American Institute of Physics, 2001.

[66] D. J. Morrissey, B. M. Sherrill, M. Steiner, A. Stolz, and I. Wiedenhoever. *Nucl. Instr. and Meth. B*, 204:90–96, 2003.

[67] G. Kraus, P. Egelhof, C. Fischer, H. Geissel, A. Himmler, F. Nickel, G. Münzenberg, W. Schwab, A. Weiss, J. Friese, A. Gillitzer, H. J. Körner, M. Peter, W. F. Henning, J. P. Schiffer, J. V. Kratz, L. Chulkov, M. Golovkov, A. Ogloblin, and B. A. Brown. *Phys. Rev. Lett.*, 73:1773–1776, 1994.

[68] F. Maréchal, T. Suomijärvi, Y. Blumenfeld, A. Azhari, E. Bauge, D. Bazin, J. A. Brown, P. D. Cottle, J. P. Delaroche, M. Fauerbach, M. Girod, T. Glasmacher, S. E. Hirzebruch, J. K. Jewell, J. H. Kelley, K. W. Kemper, P. F. Mantica, D. J. Morrissey, L. A. Riley, J. A. Scarpaci, H. Scheit, and M. Steiner. *Phys. Rev. C*, 60:034615, 1999.

[69] H. Scheit, F. Maréchal, T. Glasmacher, E. Bauge, Y. Blumenfeld, J. P. Delaroche, M. Girod, R. W. Ibbotson, K. W. Kemper, J. Libert, B. Pritychenko, and T. Suomijärvi. *Phys. Rev. C*, 63:014604, 2000.

[70] H. Iwasaki, T. Motobayashi, H. Akiyoshi, Y. Ando, N. Fukuda, H. Fujiwara, Zs Flp, K. I. Hahn, Y. Higurashi, M. Hirai, I. Hisanaga, N. Iwasa, T. Kijima, T. Minemura, T. Nakamura, M. Notani, S. Ozawa, H. Sakurai, S. Shimoura, S. Takeuchi, T. Teranishi, Y. Yanagisawa, and M. Ishihara. *Phys. Lett. B*, 481:7–13, 2000.

[71] H. Ryuto, M. Kunibu, T. Minemura, T. Motobayashi, K. Sagara, S. Shimoura, M. Tamaki, Y. Yanagisawa, and Y. Yano. *Nucl. Instr. and Meth. A*, 555:1–5, 2005.

[72] S. Kan'no, 2004. Private communication.

[73] M. Sheplak and J. Dugundji. *Journal of Applied Mechanics*, **65**:107, 1998.

[74] D. Bazin, J. A. Caggiano, B. M. Sherrill, J. Yurkon, and A. Zeller. *Nucl. Instr. and Meth. B*, 204:629–633, 2003.

[75] J. Yurkon, D. Bazin, W. Benenson, D. J. Morrissey, B. M. Sherrill, D. Swan, and R. Swanson. *Nucl. Instr. and Meth. A*, 422:291–295, 1999.

[76] W. F. Mueller, J. A. Church, T. Glasmacher, D. Gutknecht, G. Hackman, P. G. Hansen, Z. Hu, K. L. Miller, and P. Quirin. *Nucl. Instr. and Meth. A*, 466:492–498, 2001.

[77] **GEANT**. CERN library long writeup. Technical Report W5013, CERN, 1994.

[78] M.J. Berger, J.H. Hubbell, S.M. Seltzer, J. Chang, J.S. Coursey, R. Sukumar, and D.S. Zucker. XCOM: Photon cross sections database, 2005.

[79] S. Shimoura. **ECIS97** Tips. Lecture notes, 2003.

[80] W. F. Mueller, 2004. Private communication.

[81] R. Fox, C. Bolen, K. Orji, and J. Venema. NSCLSpecTcl Meeting the Needs of Preliminary Nuclear Physics Data Analysis. In *Eleventh Annual Tcl/Tk Conference New Orleans*. Institute for Nuclear Theory, University of Washington, 2004.

[82] **PAW**. CERN library long writeup. Technical Report Q121, CERN, 1999.

[83] **Minuit**. CERN library long writeup. Technical Report D506, CERN, 1998.

[84] R. W. Ibbotson, T. Glasmacher, B. A. Brown, L. Chen, M. J. Chromik, P. D. Cottle, M. Fauerbach, K. W. Kemper, D. J. Morrissey, H. Scheit, and M. Thoennessen. *Phys. Rev. Lett.*, 80:2081–2084, 1998.

[85] X. Liang, F. Azaiez, R. Chapman, F. Haas, D. Bazzacco, S. Beghini, B. R. Behera, L. Berti, M. Burns, E. Caurier, L. Corradi, D. Curien, A. Deacon, G. de Angelis, Zs. Dombradi, E. Farnea, E. Fioretto, A. Hodsdon, A. Gadea, F. Ibrahim, A. Jungclaus, K. Keyes, A. Latina, S. Lunardi, N. Marginean, R. Menegazzo, G. Montagnoli, D. R. Napoli, F. Nowacki, J. Ollier, A. Papenberg, G. Pollarolo, V. F. E. Pucknell, M.-D. Salsac, F. Scarlassara, J. F. Smith, K. Spohr, M. Stanoiu, A. M. Stefanini, S. Szilner, N. Toniolo, M. Trotta, D. Verney, Z. Wang, and J. Wrzesinski. *Phys. Rev. C*, 74:014311, 2006.

[86] M. A. Caprio. *Comp. Phys. Comm.*, 171:107, 2005.

[87] F. Azaiez. *Journal of Physics: Conference Series*, 49:146–152, 2006.

[88] H. Scheit, T. Glasmacher, B. A. Brown, J. A. Brown, P. D. Cottle, P. G. Hansen, R. Harkewicz, M. Hellström, R. W. Ibbotson, J. K. Jewell, K. W. Kemper, D. J. Morrissey, M. Steiner, P. Thirolf, and M. Thoennessen. *Phys. Rev. Lett.*, 77:3967–3970, 1996.

[89] J. A. Winger, P. F. Mantica, R. M. Ronningen, and M. A. Caprio. *Phys. Rev. C*, 64:064318, 2001.

[90] D. Sohler, Zs. Dombrádi, J. Timár, O. Sorlin, F. Azaiez, F. Amorini, M. Belleguic, C. Bourgeois, C. Donzaud, J. Duprat, D. Guillemaud-Mueller, F. Ibrahim, J. A. Scarpaci, M. Stanoiu, M. J. Lopez, M. G. Saint-Laurent, F. Becker, F. Sarazin, C. Stodel, G. Voltolini, S. M. Lukyanov, V. Maslov, Yu.-E. Penionzhkevich, M. Girod, S. Péru, F. Nowacki, and G. Sletten. *Phys. Rev. C*, 66:054302, 2002.

[91] S. Grévy, F. Negoita, I. Stefan, N. L. Achouri, J. C. Angélique, B. Bastin, R. Borcea, A. Buta, J. M. Daugas, F. de Oliveira, O. Giarmana, C. Jollet, B. Laurent, M. Lazar, E. Liénard, F. Maréchal, J. Mrázek, D. Pantelica, Y. Penionzhkevich, S. Piétri, O. Sorlin, M. Stanoiu, C. Stodel, and M. G. St-Laurent. *Eur. Phys. J. A*, 25:111–113, 2005.

[92] Data extracted using the NNDC On-Line Data Service from the ENSDF database, revised as of March 30, 2006.

[93] B. A. Brown et al. **OXBASH** for Windows. Technical Report 1289, MSU-NSCL, 2004.

[94] M. Horoi. Central Michigan Shell Model Code (**CMichSM**): Present and Future Applications. In *Advanced Computational Methods for Solving the Nuclear Many-Body Problem*. Institute for Nuclear Theory, University of Washington, 2002.

[95] A. Gade, B. A. Brown, D. Bazin, C. M. Campbell, J. A. Church, D. C. Dinca, J. Enders, T. Glasmacher, M. Horoi, Z. Hu, K. W. Kemper, W. F. Mueller, T. Otsuka, L. A. Riley, B. T. Roeder, T. Suzuki, J. R. Terry, K. L. Yurkewicz, and H. Zwahlen. *Phys. Rev. C*, 74:034322, 2006.

[96] B. A. Brown, 2006. Private communication.

[97] M. Stanoiu, F. Azaiez, Zs Dombrdi, O. Sorlin, B. A. Brown, M. Belleguic, D. Sohler, M. G. Saint Laurent, Y. E. Penionzhkevich, G. Sletten, C. Borcea, C. Bourgeois, A. Bracco, J. M. Daugas, Z. Dlouh, C. Donzaud, Zs Flp, D. Guillemaud-Mueller, S. Grvy, F. Ibrahim, A. Kerek, A. Krasznahorkay, M. Lewitowicz, S. Lukyanov, P. Mayet, S. Mandal, W. Mittig, J. Mrzek, F. Negoita, F. De Oliveira-Santos, Zs Podolyk, F. Pougheon, P. Roussel-Chomaz, H. Savajols, Y. Sobolev, C. Stodel, J. Timr, and A. Yamamoto. *Nucl. Phys. A*, 746:135–139, 2004.

[98] E. K. Warburton and B. A. Brown. *Phys. Rev. C*, 46:923–944, 1992.

[99] B. A. Brown and W. A. Richter. *Phys. Rev. C*, 72:057301, 2005.

[100] T. R. Werner, J. A. Sheikh, W. Nazarewicz, M. R. Strayer, A. S. Umar, and M. Misu. *Phys. Lett. B*, 335:259–265, 1994.

[101] R. du Rietz, J. Ekman, D. Rudolph, C. Fahlander, A. Dewald, O. Moller, B. Saha, M. Axiotis, M. A. Bentley, C. Chandler, G. de Angelis, F. Della Vedova, A. Gadea, G. Hammond, S. M. Lenzi, N. Marginean, D. R. Napoli, M. Nespolo, C. Rusu, and D. Tonev. *Phys. Rev. Lett.*, 93:222501, 2004.

[102] H. Sagawa and B. A. Brown. *Nucl. Phys. A*, 430:84–98, 1984.

[103] N Alamanos, F Auger, B A Brown, and A Pakou. *J. Phys. G*, 24:1541–1546, 1998.

[104] S. Raman, C. W. Nestor, and P. Tikkanen. *At. Data and Nucl. Data Tables*, 78:1–128, 2001.

[105] B. Jurado, H. Savajols, W. Mittig, N. A. Orr, P. Roussel-Chomaz, D. Baiborodin, W. N. Catford, M. Chartier, C. E. Demonchy, Z. Dlouh, A. Gillibert, L. Giot, A. Khouaja, A. Lpine-Szily, S. Lukyanov, J. Mrazek, Y. E. Penionzhkevich, S. Pita, M. Rousseau, and A. C. Villari. *Phys. Lett. B*, 649:43–48, 2007.